Universitá degli studi di Padova

Dipartimento di Fisica e Astronomia "G. Galilei"
Corso di dottorato di ricerca in Fisica
Ciclo XXXI

# A fast ionization chamber for the detection of fusion-evaporation residues produced by the exotic beams of SPES: design, tests and first experiments

Coordinatore: Ch.ma Prof. Cinzia Sada
Supervisore: Ch.mo Prof. Alberto M. Stefanini
Co-supervisore: Ch.ma Prof. Giovanna Montagnoli

Dottoranda: Giulia Colucci

UNIVERSITÁ DEGLI STUDI DI PADOVA

# *Abstract*

Corso di dottorato di ricerca in fisica
Dipartimento di Fisica e Astronomia "G. Galilei"

Doctor of Philosophy

**A fast ionization chamber for the detection of fusion-evaporation residues produced by the exotic beams of SPES: design, tests and first experiments**

by Giulia COLUCCI

This thesis work is divided in two parts: (*i*) designing and constructing a new ionization chamber with fast response (FastIC) for the study of near- and sub-barrier fusion of exotic systems using the very neutron-rich beams of the SPES facility in construction at the Laboratori Nazionali di Legnaro (LNL) of INFN, and (*ii*) carrying out, analyzing and interpreting the results of the sub-barrier fusion experiment for the two systems $^{36}$S + $^{50}$Ti,$^{51}$V, performed using the FastIC.

A new set-up for fusion cross-section measurements, especially designed for the low-intensity beams delivered by the SPES facility, has been developed at the LNL. This new set-up includes a fast IC designed to withstand a high counting rate particle identification for fusion studies involving exotic beams up to $10^5$ pps. The readout of the FastIC was optimised and extensive tests using stable heavy-ion beams demonstrated its ability to operate up to rates of ∼140 kHz, compared to few kHz of the previous IC chamber. This feature and the much larger solid angle coverage will allow to detect fusion-evaporation residues with an efficiency close to 100%.

The new FastIC has been employed for the experimental study of sub-barrier fusion in the $^{36}$S + $^{50}$Ti, $^{51}$V systems. The possible effect of the non-zero spin of $^{51}$V ground state on the sub-barrier excitation function and on the shape of the barrier distribution has been investigated. The two excitation functions have been measured down to cross sections ∼20 $\mu$b, and it appears that they are very similar to each other. A coupled channels analysis has been performed in order to highlight differences between the two systems, and a modified coupled-channels code was used in order to treat the odd nucleus $^{51}$V. The experimental excitation functions and the extracted barrier distributions have been compared to the theoretical predictions. This comparison suggests a small difference between the two systems above the barrier, that might be experimentally observed by measuring the backward-angle quasi-elastic scattering in that energy region.

# Contents

# List of Figures

# List of Tables

# List of Abbreviations

| | |
|---|---|
| **ER** | **E**vaporation **R**esidues |
| **CN** | **C**ompound **N**ucleus |
| **LNL** | **L**aboratori **N**azionali di **L**egnaro |
| **SPES** | **S**elective **P**roduction of **E**xotic **S**pecies |
| **RIBs** | **R**adioactive **I**on **B**eams |
| **CC** | **C**oupled **C**hannel |
| **ORNL** | **O**ak **R**idge **N**ational **L**aboratory |
| **HRIBF** | **H**olifield **R**adioactive **I**on **B**eams **F**acility |
| **ISOL** | **I**sotope **S**eparation **O**n **L**ine |
| **LNS** | **L**aboratori **N**azionali del **S**ud |
| **INFN** | **I**stituto **N**azionale di **F**isica **N**ucleare |
| **PIAVE** | **P**ositive **I**on **A**ccelerator for **VE**ry low velocity ions |
| **ALPI** | **A**cceleratore **L**ineare **P**er **I**oni |
| **TIS** | **T**arget coupled to the **I**on **S**ource |
| **HRMS** | **H**igh **R**esolution **M**ass **S**pectrometer |
| **ECR** | **E**lectron **C**yclotron **R**esonance |
| **PISOLO** | **PI**ccolo **SOL**en**O**ide |
| **MCP** | **M**icro **C**hannel **P**lates |
| **IC** | **I**onization **C**hamber |

*To my Parents*

# Chapter 1

# Introduction

## 1.1 Fusion reactions in the near- and sub-barrier region

The increasing interest in heavy-ion fusion begins with the possibility to extend the periodic table beyond the elements synthesized using neutrons and light charged particles.

The ion-ion potential consists of a repulsive Coulomb term and a short-ranged attractive nuclear component. The Coulomb barrier arises from the balance of these two opposite forces, so that at energies lower than the barrier, quantum tunneling is the process leading to compound nucleus formation. In the simplest approach, the distance between the centers of mass of two interacting nuclei represents the only degree of freedom.

Thanks to the firsts Tandem electrostatic accelerators, medium-mass heavy-ion beams have been produced with sufficient energy to overcome the Coulomb barrier in collisions with targets of nearly all elements. Consequently, much interest has been devoted since then to the study of reaction dynamics with such heavy beams.

At energies above the barrier, fusion accounts for a large part of the reaction cross section, so that a comprehensive study of this type of reactions became essential in nuclear physics. Early theoretical descriptions of fusion were quite simple, nevertheless they clarified the overall dependence of the cross sections on beam energy, system size, and the range of angular momenta involved.

Fusion excitations of light heavy-ion systems essentially follow the predictions of the Wong formula [1] based on the quantum penetration of the barrier. On the contrary , experimental and theoretical studies on near- and sub-barrier heavy-ion fusion pointed out inconsistencies. Experiments showed up a large enhancement of cross sections with respect to the simple predictions of the Wong formula and highlighted strong isotopic dependences [2].

It was soon realized [3, 4, 5] that the enhancement is related to the low-lying collective structure of the two colliding nuclei. The coupled channels (CC) model was subsequently developed [3] in order to address the effects of the couplings between the relative motion and nuclear intrinsic degrees of freedom and to reproduce the experimental evidences.

An important consequence of channel coupling was to introduce a distribution of fusion barriers, where the fusion cross section is given by a weighted sum of the fusion cross sections for each barrier. On the basis of this idea, Rowley et al. [6] proposed a simple and elegant mathematical transformation to extract the distribution of barriers directly from precise fusion cross section measurements. The extracted fusion barrier distributions provided a much clearer way of understanding the effects of channel couplings on the fusion process than the fusion excitation functions themselves.

The development of new instrumentation and methods allowed the extension of measurements to deep sub-barrier energies, revealing an unanticipated drop in the cross sections that could not be explained by the coupled-channels theory with standard ion-ion potentials. This phenomenon, named “hindrance” [7], opened a new area of research and is still a matter of debate.

## 1.2 The experimental approach

Experimentally, fusion can be recognised in terms of the nuclei formed in the reaction or of the products of their following decay, since these are the measurable quantities. For light nuclei, the compound nucleus (CN) decays by light particles evaporation, leaving an evaporation residue (ER). The direct or indirect detection of ER is therefore a clear-cut experimental evidence that fusion has occurred. In heavy systems where fission can compete with particle evaporation, the fission decay branch must also be measured in order to obtain the total fusion cross section.

When the CN decays only by particles evaporation, the fusion cross sections can be determined by direct detection of the ER or by detecting the radiation emitted in their deexcitation.

The measurement of the ER implies the separation in space, and often in time, from the beam particles. Detection of alpha-particle decay has been successfully used in the determination of fusion cross section for reactions where alpha decay is the dominant or exclusive ER decay mode. Measurements of gamma rays, delayed X rays and evaporated neutrons have also been used to obtain fusion cross sections, despite high precision measurements result more difficult because of the uncertainties in feeding of the decaying states, in branching ratios, and in absolute detection efficiency.

In the direct detection methods, the ER, which are forward peaked, must be physically separated from the direct beam and the intense flux of elastically scattered beam particles. By using the different electrical rigidity of ER with respect to beam particles, their separation can be achieved by applying an electrostatic field perpendicular to the direction of the particles and placed between the target and the detection system. Such an electrostatic beam deflector has been used at the National Laboratories of Legnaro (LNL) in experiments on heavy-ion fusion, where an energy, loss of energy and time-of-flight telescope, based on micro-channel plates, ionization chamber and Silicon surface barrier detectors, detects and identifies the ER.

## 1.3 New perspectives with radioactive beams

The availability of accelerated beams of unstable nuclei introduced the possibility to extend studies of sub-barrier fusion to systems with large excess of neutrons or protons. Such studies will lead to a better understanding of the role that neutron excess plays in enhancing sub-barrier fusion and may constitute the way to synthesize heavier nuclei by using neutron-rich radioactive nuclei. However this aim is very challenging. The intensities of radioactive beams decrease farther from stability, and often the beams are contaminated by mixtures of nuclides, according to the facility and production technologies. Therefore, experiments have to employ methods to mitigate the effects of beam impurity and low beam intensity.

In the case of the detection of ER and beam-like heavy recoils at far forward angles, the measurements with radioactive beams are critical, in particular in the inverse kinematics reactions. The high contamination of the radioactive heavy ion beams by other elements having similar energies and masses requires detection systems able to distinguish the beam particles from unwanted constituents. Furthermore, in some studies it is very important to design detectors that avoid unnecessary energy straggling and angular dispersion. Under these conditions, the detection system should exhibit an efficiency close to 100% and assure a fast response time to avoid limitations of the intensity of the beam in the experiments. Gas-filled ionization chambers are well suited for these applications, since they have moderately good energy resolution and can withstand prolonged exposure to high beam intensities without damage, in contrast to fragile semiconductor detectors.

A new set-up for fusion cross section measurements, especially designed for the low intensity beams which will be delivered by the SPES facility, has been developed and is being installed at LNL. The set-up is characterized by a significant improvement with respect to the electrostatic deflector previously in use thanks to a very fast ionization chamber (IC), which ensures a high counting rate particle identification for fusion studies involving exotic beams (up to $\sim 10^5$ pps).

The project of this PhD thesis has been to develop and test this Fast Ionization Chamber and to perform the sub-barrier fusion measurement of the two systems $^{36}\mathrm{S} + {}^{50}\mathrm{Ti}$, $^{51}\mathrm{V}$, where the Fast IC was used for the first time.

This thesis is organized as follows. Chapter 2 provides a complete description of the coupled-channels model. The concept of fusion barrier distributions and how it can be extracted from the data is illustrated, with a brief introduction to the hindrance phenomena. Chapter 3 briefly outlines the extra-features of heavy-ion fusion evidenced by means of exotic beams, with a special emphasis on the new facility SPES in construction at LNL and on the low intensity radioactive beams which will be used in the future. In Chapter 4 the electrostatic deflector of LNL for near and sub-barrier fusion reactions is presented, as well as its planned upgrade for the SPES beams. The Fast Ionization Chamber is introduced with its fundamental features and the way how to build a IC with fast response. Chapter 5 reports on the several tests with stable beams performed to optimize the performance of the new detector. The fast ionization chamber was employed in one full experiment with stable beams, whose results are reported in Chapter 6. In this experiment the sub-barrier fusion of the two systems $^{36}\mathrm{S} + {}^{50}\mathrm{Ti}$, $^{51}\mathrm{V}$ was measured in order to investigate the possible effect of the non-zero spin of the ground state of $^{51}\mathrm{V}$ on sub-barrier excitation function, and in particular on the shape of the barrier distribution. Concluding remarks are given in Chapter 7, which summarizes the subjects covered by this thesis.

## Chapter 2

# Fusion reactions near and below the Coulomb barrier

One of the fundamental processes in quantum mechanics is quantum tunnelling, which occurs when a particle penetrates a classically forbidden region. It is a wave phenomenon and is frequently encountered in various processes in chemistry and physics. In many applications of quantum tunnelling, the penetration of a one-dimensional potential barrier, or a single variable dependent barrier, is required. In general a barrier of this type neglects the interactions of the particle with its surroundings or environment, which results in the modification of its behaviour. In addition, in the case of composite particles, the quantum tunnelling has to be treated through a many-particle approach. Under these conditions, the quantum tunnelling process takes place in a multidimensional space. In a complex system, the tunnelling variable couples to a large number of degrees of freedom and in most cases these degrees of freedom reveal a dissipative character.

In nuclear physics, a typical process where the tunnelling phenomena occurs is the heavy-ion fusion reaction at energies near and below the Coulomb barrier. The fusion is a process where two separate nuclei combine together and generate a compound nucleus. Classically, this process takes place when the energy of the relative motion between the two interacting nuclei overcomes the Coulomb barrier, which is produced by the long range repulsive Coulomb force and the short range attractive strong nuclear force. In these conditions, the coupling to external environments can be neglected since the atomic nuclei can be assumed as isolated systems. On the contrary, the coupling to the intrinsic degrees of freedom are not negligible. During fusion reactions, the excited states of both projectile and target are populated in a complex way and their relative motion couples to them. This coupling to the intrinsic degree of freedom of the colliding nuclei results in an enhancement of the fusion cross section at energies below the Coulomb barrier.

The standard method used to calculate the effects of such couplings on fusion reactions is to numerically solve the coupled-channels equations, which include all the relevant channels.

In this chapter, the theoretical aspects of heavy-ion sub-barrier reactions from the viewpoint of quantum tunnelling of composite particles are discussed. With this aim the coupled-channels formalism is introduced and is followed by a discussion on the fusion barrier distribution representation and on the present status of our understanding of deep sub-barrier fusion reactions.

## 2.1 One-dimensional potential model

### 2.1.1 The ion-ion potential

The simplest approach to the heavy-ion fusion reactions is within a one-dimensional potential model in which the projectile and target nuclei are treated as being structureless. Under this condition, the potential is a function of only the relative distance $r$ between the colliding nuclei and it consists of two parts: the nuclear potential $V_N(r)$ and the Coulomb potential $V_C(r)$ :

$$V(r) = V_N(r) + V_C(r) \tag{2.1}$$

The Coulomb potential is expressed as the electrostatic potential between two point-like charged particles placed at a distance $r$:

$$V_C(r) = \frac{e^2}{4\pi\epsilon_0}\frac{Z_p Z_t}{r} \tag{2.2}$$

where $Z_p$ and $Z_t$ are the projectile and target atomic number, respectively. This expression neglects the structure of the nuclei and is valid in the region where the projectile and target do not significantly overlap with each other ($r \geq r_t + r_p$ , where $r_p$ and $r_t$ are the projectile and target nuclear radii, respectively). As an alternative option, the projectile nucleus can be assumed point-like charge whereas the target nucleus is treated as a sphere with a uniform charge $Z_t$ and a radius $R_C$. In this case the Coulomb potential is given as:

$$V(r) = \frac{e^2}{4\pi\epsilon_0} Z_p Z_t \begin{cases} \frac{1}{r} & r > R_C \\ \frac{1}{2R_C}(3 - \frac{r^2}{R_C^2}) & r < R_C \end{cases} \tag{2.3}$$

Because of the dependence on the atomic numbers, the importance of the Coulomb potential increases in reactions involving heavy nuclei.

A typical potential V(r) for the $s$-wave scattering of $^{16}O + ^{144}Sm$ reaction [8] is shown in Fig. 2.1. Classically, the Coulomb barrier has to be overcome for the fusion reaction to occur. In Fig. 2.1 the distance at which the colliding nuclei begin to overlap significantly is defined as the *touching radius* $R_{touch}$ and the Coulomb barrier is placed outside this radius.

The nuclear potential is a crucial component of the total potential, in particular in the coupled-channels approach. As a matter of fact, it establishes not only the height of the Coulomb barrier but also the nuclear couplings to the excited states of the interacting nuclei. There are several ways to estimate this potential. The ion-ion potential that has been widely used is the phenomenological Woods-Saxon potential:

$$V_N(r) = -\frac{V_0}{1 + exp[(r - R_0)/a_0]} \tag{2.4}$$

where $R_0$ is the radius, $V_0$ is the depth and $a_0$ is the diffuseness of the potential. A standard set of parameters that are consistent with the analysis of elastic scattering

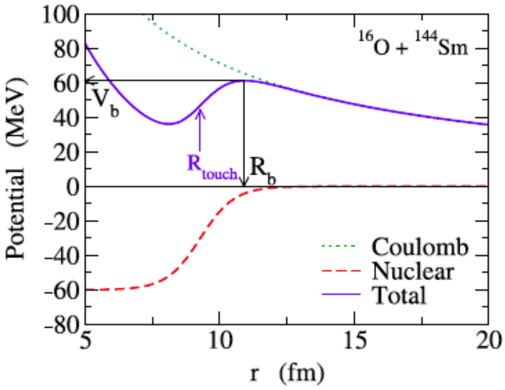

FIGURE 2.1: Internucleus potential for the $^{16}\mathrm{O} + {}^{144}\mathrm{Sm}$ reaction [8]. The dotted and dashed lines represent the Coulomb and nuclear potentials, respectively. The solid line denotes the total potential. The height $V_b$ and position $R_b$ of the Coulomb barrier are shown. The projectile and target nuclei start overlapping significantly with each other at the touching radius $R_{touch}$.

data [9, 10] is the following:

$$
\begin{gathered}
V_0 = 16\pi\gamma a_o \tfrac{R_p R_t}{R_p + R_t} \\
R_0 = R_p + R_t \\
a_0 = \tfrac{1}{1.17[1+0.53(A_p^{-1/3}+A_t^{-1/3})]} \qquad (2.5) \\
R_i = (1.2A_i^{1/3} - 0.09) fm \qquad i = t, p \\
\gamma = 0.95(1 - 1.8(A_p - 2Z_p)(A_t - 2Z_t)/(A_p/A_t))
\end{gathered}
$$

This empirical potential is sometimes referred to as Akyuz-Winther potential and is a smooth function of the mass numbers of the reacting nuclei. The nuclear potential constructed in this way has been successful in reproducing experimental angular distributions of elastic and inelastic scattering for many systems [9]. The empirical value of the surface diffuseness parameter, a ∼0.63 fm, is consistent also with the double-folding potential, which will be shortly introduced. Recently it has been realised that the Akyuz-Winther parametrization of the ion-ion potential is unrealistic for overlapping nuclei and provides a poor description of the fusion data at extreme sub-barrier energies. For some systems, the potential fitting elastic and inelastic scattering data overestimates fusion cross sections at energies both above and below the Coulomb barrier. The reason is that heavy-ion scattering is a process which involves the surface of the nucleus, while fusion implies a stronger overlap of the interacting nuclei [8].

A way to overcome this problem is to use a double-folding potential and adjust it for overlapping nuclei so that it provides a better description at very low energies. Such a potential is given by

$$V(\mathbf{r}) = \int dr_1 \int dr_2 \rho_P(r_1)\rho_T(r_2) v_{NN}(r_2 - r_1 - r) \tag{2.6}$$

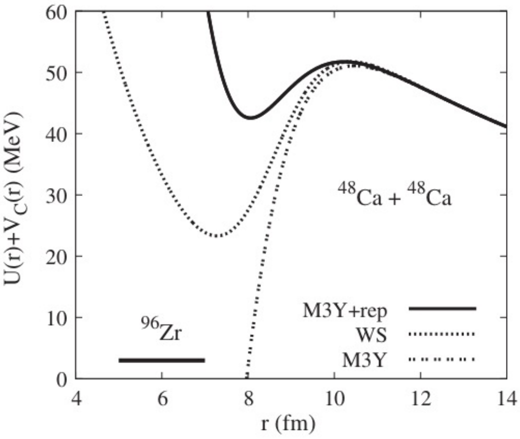

FIGURE 2.2: Comparison of the Woods-Saxon potential (dotted line) with the M3Y potential without (dashed curve) and with (solid line) repulsive term, for the $^{48}$Ca + $^{48}$Ca system [13]. The horizontal bar indicates the ground state of the compound nucleus $^{96}$Zn.

where $v_{NN}$ is the effective nucleon-nucleon interaction, and $\rho_P$ and $\rho_T$ are the density of the projectile and target, respectively.
An interaction that is often used is the Michigan-3-Yukawa-Reid (M3Y) interaction [11, 12], which turns to be quite reliable in reproducing the height of the Coulomb barrier. The double-folding potential produced by the M3Y interaction is in good agreement with the phenomenological Akyuz-Winther potential in reproducing the situation in the region outside the barrier where the elastic scattering is the prevalent channel. On the contrary, the potential constructed in this way is unrealistic for the sub-barrier energy region where the overlapping of the nuclei occurs. This is due to the fact that in this energy region the M3Y interaction provides a potential which results much deeper than the ground-state energy of the compound nucleus, as shown in Fig. 2.2. To correct for this deficiency, the ion-ion potential should also contain a repulsive core, that was suggested to originate from the incompressibility of nuclear matter, and which is introduced by supplementing the M3Y with a repulsive term:

$$v_{NN}^{rep}(r) = v_0 \delta(r) \tag{2.7}$$

The repulsive potential is thus obtained by replacing this constant term as an interaction in the double-folding potential Eq. 2.6. The amplitude $v_0$ is calibrated to reproduce a reasonable incompressibility of the overlapping nuclei, while the diffusivity is modified in order to obtain the best agreement between the fusion data and the results of coupled channels calculations. An example of the entrance channel potential for the fusion reaction of the symmetric system $^{48}$Ca + $^{48}$Ca [13] is shown in the Fig. 2.2. The excessive depth of the M3Y interaction is reduced following the introduction of the repulsive core. The behaviour of the ion-ion potential in the nuclear overlapping region is of crucial importance in the understanding the fusion hindrance phenomenon, which discussion is carried on in section 2.4.

The fusion of two spherical colliding nuclei can be described by using a three-dimensional Schrödinger equation, as follows:

$$\left[ -\frac{\hbar^2}{2\mu}\Delta + V(r) - E \right] \Phi(r) = 0 \tag{2.8}$$

where $\mu$ is the reduced mass of the system and $V(r)$ the total potential. When both the projectile and target are assumed structureless, the total potential coincides with the one given by the Eq. 2.1. The solution of the equation can be expanded in terms of spherical harmonics, where the radial part obeys the following equation:

$$\left(-\frac{\hbar^2}{2\mu}\frac{d^2}{dr^2}+\frac{l(l+1)\hbar^2}{2\mu r^2}+V(r)-E\right)u_l(r)=0 \tag{2.9}$$

In the last equation the centrifugal repulsive potential appears.

### 2.1.2 The Coulomb barrier and the compound nucleus

The presence of a pocket in the nucleus-nucleus potential allows the use of a conceptually simple fusion criterion where the capture and subsequent fusion of the system takes place if it "enters" in the pocket. This hypothesis is valid for kinetic energies that are not significantly higher than the fusion barrier, since for high energies higher angular momenta may contribute to the fusion process and the depth of the potential pocket decreases until it disappears above a critical value $l_{crit}$ [14].

$$l_{crit}=R_0\sqrt{\frac{2\mu}{\hbar^2}(E-B)} \tag{2.10}$$

This value is derived from the conservation of angular momentum and depends on the energy $E$, the height of the barrier $B$ and its position $R_0$.

For values lower than $l_{crit}$, dissipative forces reduce the initial orbital angular momentum and consequently the centrifugal potential of the system. Under these conditions the system is captured inside the pocket and can then evolve towards the formation of a compound nucleus. On the contrary, if the orbital angular momentum is higher than the critical value $l_{crit}$, the capture does not take place and the two colliding ions separate after a period of contact in which energy dissipation and exchange of nucleons occur.

Following the fusion of the two colliding nuclei, the compound nucleus is produced usually at high excitation energy and tends to decay according to two main schemes: evaporation of light particles and/or fission.

During the evaporation light particles (such as neutrons, protons and alpha particles) are emitted. The remaining nucleus is referred as *evaporation residue* and exhibits slightly lower mass than the compound nucleus.

On the other hand, when fission occurs, the compound nucleus brakes into two fragments of comparable mass. The excitation energy is transferred not only to the relative motion of the fission products but also to the internal degrees of freedom of each of them. The fission process is typical of heavy nuclei. It is due to the competition between the repulsive force of protons which induce strong deformations and the surface effects that tend to re-establish a spherical shape [15]. These forces, working the opposite ways, are related through the fissility parameter

$$x=\frac{E_C}{2E_S}\sim\frac{Z^2}{50A} \tag{2.11}$$

where $E_C$ and $E_S$ are the Coulomb and surface energy, respectively [15]. The fissility parameter is higher for havier systems (for example, the fissility for the $^{36}$S + $^{50}$Ti system, which will be shown in Chapter 6, is of about ~0.008 while for $^{58}$Ni + $^{208}$Pb is of the order of ~0.012). Nuclei with very high Z drift to fission.

### 2.1.3 Fusion cross section

The one-dimensional potential model is the simplest barrier penetration model since the only variable is the relative motion of the two colliding nuclei. The barrier has a height proportional to the product of the charges of the two nuclei. Under these conditions, a greater overlap of the densities of the interacting nuclei is needed when systems with a high $Z$ are involved in the reaction. Once the overlap is significant, the nucleon-nucleon interaction becomes dominant and leads to a substantial loss of kinetic energy and angular momentum of the relative motion, so that the nuclei can not escape from the potential pocket and fusion occurs.

In this model, the interaction is therefore closely linked to the probability that the system with angular momentum $l$ will cross the barrier overcoming the total potential. Neglecting the spin, this probability is expressed by the transmission coefficient $T_l(E)$ relative to the energy $E$ and the partial wave $l$. The cross section is proportional to the transmission coefficient through the multipolar components of the interaction

$$\sigma_l(E) = \pi\lambdabar^2(2l+1)T_l(E) \tag{2.12}$$

where $\lambdabar$ is is the reduced de Broglie wavelength of the relative motion. The total cross section is obtained by the sum on the partial waves:

$$\sigma(E) = \sum_{l=0}^{\infty} \pi\lambdabar^2(2l+1)T_l(E) \tag{2.13}$$

Not all partial waves take part in the fusion process, since above the critical value $l_{crit}$ (Eq. 2.10) fusion does not occur. The fusion cross section is therefore smaller than the total one and can be expressed as:

$$\sigma^{fus}(E) = \sum_{l=0}^{\infty} \pi\lambdabar^2(2l+1)T_l(E)P_l^{fus}(E) \tag{2.14}$$

$P_l^{fus}(E)$ represents the probability that the $lth$-partial wave overcomes the Coulomb barrier and leads to fusion. According to this definition, it can be expressed as:

$$P_l^{fus}(E) = \begin{cases} 0 & l > l_{crit} \\ 1 & l < l_{crit} \end{cases} \tag{2.15}$$

Under this condition, the fusion cross section becomes:

$$\sigma^{fus}(E) = \sum_{l=0}^{l_{crit}} \pi\lambdabar^2(2l+1)T_l(E) \tag{2.16}$$

The transmission coefficient is derived from the solution of the Schrödinger equation, Eq. 2.35. Another way to obtain the transmission coefficient and the following fusion cross section is using the Hill-Wheeler [16] approximation, where the Coulomb barrier is approximated by a parabola:

$$V_l(r) \sim V_{bl} - \frac{1}{2}\mu\Omega_l^2(r-R_{bl})^2 \tag{2.17}$$

where $V_{bl}$ is the barrier height, $\Omega_l$ is the curvature relative the $l$th wave and $R_{bl}$ indicates the position of the barrier. Within this approximation, the corresponding transmission coefficient is evaluated analytically [16] as:

$$T_l(E) = \frac{1}{1 + exp[\frac{2\pi}{\hbar\Omega_l}(V_{bl} - E)]} \tag{2.18}$$

where the curvature is defined as:

$$\hbar\Omega_l = \sqrt{-\frac{\hbar^2}{\mu}\frac{\delta^2 V_l(r)}{\delta r^2}\bigg|_{r=R_{bl}}} \tag{2.19}$$

By replacing the transmission coefficient in Eq. 2.16, the fusion cross section is expressed as follow:

$$\sigma^{fus}(E) = \sum_{l=0}^{l_{crit}} \pi ƛ^2 \frac{2l+1}{1 + exp[-\frac{2\pi}{\hbar\Omega_l}(E - V_{bl})]} \tag{2.20}$$

A simpler expression is obtainable by assuming that both the curvature and the position of the Coulomb barrier are independent of the angular momentum $l$. This condition allows to approximate these values to the ones for the $s$-wave ($l$=0).

$$\begin{cases} R_{bl} \simeq R_{b0} \\ \hbar\Omega_l \simeq \hbar\Omega_0 \end{cases} \tag{2.21}$$

The height of the barrier relative to the $l$th wave is therefore:

$$V_{bl} = V_{b0} + \frac{\hbar^2}{2\mu}\frac{l(l+1)}{R_{b0}^2} \tag{2.22}$$

Under these conditions, the dependence of the transmission coefficient on the angular momentum can be well approximated by shifting the incident energy by a rotational term:

$$T_l(E) = T_0\left(E - \frac{\hbar^2}{2\mu}\frac{l(l+1)}{R_{b0}^2}\right) \tag{2.23}$$

If many partial waves contribute to the fusion cross section, the sum in Eq. 2.13 may be replaced by the integral form:

$$\sigma_{fus}(E) = \pi ƛ^2 \int_0^\infty dl(2l+1)T_l(E) \tag{2.24}$$

Changing the variable from $l$ to $l(l+1)$, the integral can be explicitly evaluated, leading to the Wong formula [1]:

$$\sigma^{fus}(E) = \frac{\hbar\Omega_0 R_{b0}}{2E} ln\left\{1 + exp\left[\frac{2\pi}{\hbar\Omega_0}(E - V_{b0})\right]\right\} \tag{2.25}$$

In the high and low energy limits the cross section can be approximated by the expressions:

$$\sigma^{fus}(E) = \begin{cases} \pi R_{b0}^2(1 - \frac{V_{b0}}{E}) & E \gg V_{b0} \\ \\ \frac{\hbar\Omega_0 R_{b0}}{2E} exp\left[\frac{2\pi}{\hbar\Omega_0}(E - V_{b0})\right] & E \ll V_{b0} \end{cases} \tag{2.26}$$

At energies below the Coulomb barrier the cross section depends exponentially on the difference $(E - V_{b0})$. Another observation is that, in the high energies range, the expression coincides with the cross section predicted by the classical theory 2.12, assuming $T_l = 0$ for $l > l_{max}$, and $T_l = 1$ for $l < l_{max}$. Under this approximation the fusion cross section is

$$\sigma(E) = \sum_{l=0}^{l_{max}} \pi \lambda\!\!\bar{}^{2}(2l+1) \simeq \pi \lambda\!\!\bar{}^{2} l_{crit}^2 \tag{2.27}$$

By replacing the $l_{crit}$ value given by Eq. 2.10, the cross section in the high energy limit of Eq. 2.26 is obtained.

### 2.1.4 Comparison with experimental data

The single barrier penetration model has achieved great success in the description of fusion cross section in light systems. On the contrary, it underestimates the sub-barrier fusion for heavier systems, although it reproduces the experimental data above the Coulomb barrier. This suggested that other degrees of freedom take part in the fusion process besides the relative motion of the two nuclei.

The study of the $^{16}$O + $^{144,148,154}$Sm [17] reactions provided an evidence of the influence of the nuclear structure on sub-barrier fusion. As shown in Fig. 2.3 (left panel), the fusion cross sections for the different systems match each other at energies above the Coulomb barrier. On the contrary, at lower energies all excitation functions are strongly enhanced with respect to the one-dimensional barrier penetration ("no coupling") calculation, and the more deformed Sm isotopes have larger cross sections below the barrier.

On the other hand, the comparison of the three $^{58}$Ni + $^{58}$Ni, $^{58}$Ni + $^{64}$Ni and $^{64}$Ni + $^{64}$Ni systems [18] showed, in addition to the excitation function enhancement, a more gradual decrease of the excitation function for $^{58}$Ni + $^{64}$Ni with respect to the other two systems (see Fig. 2.3 right panel). This trend was associated with the availability of positive Q-value neutron transfer channels for $^{58}$Ni + $^{64}$Ni, unlike for the other two systems. This evidence led to the hypothesis that specific reaction channels may influence the fusion process.

The inadequacy of the one-dimensional model has been demonstrated in a more transparent way by Balantekin et al [19]. They extracted an effective potential from the experimental data. The resulting potential was largely unphysical for heavy systems. This allowed to associate the fusion enhancement not to an incorrect shape of the potential, but rather to the inadequacy of considering spherical and inert nuclei, only interacting through a one-dimensional effective potential.

From these results and from those obtained in subsequent studies the enhancement was therefore attributed *i*) to the existence of collective excitation modes (surface modes) in the interacting nuclei of vibrational and/or rotational nature, and *ii*) to transfer processes that may take place during the collision.

There are many other modes of excitation in addition to the low-lying collective excitations. Non-collective excitations couple only weakly to the ground state and usually they do not significantly affect heavy-ion fusion reactions, even if the number of non-collective states is large [20, 21]. On the other hand, couplings to giant resonances are relatively strong because of their collective character. However, since their excitation energies are high [22], their effects are included in the choice of ion-ion potential which is renormalized by those high energy excitations [23, 24].

The effects of the nuclear structure can be taken into account in a more quantitative way using the coupled-channels model.

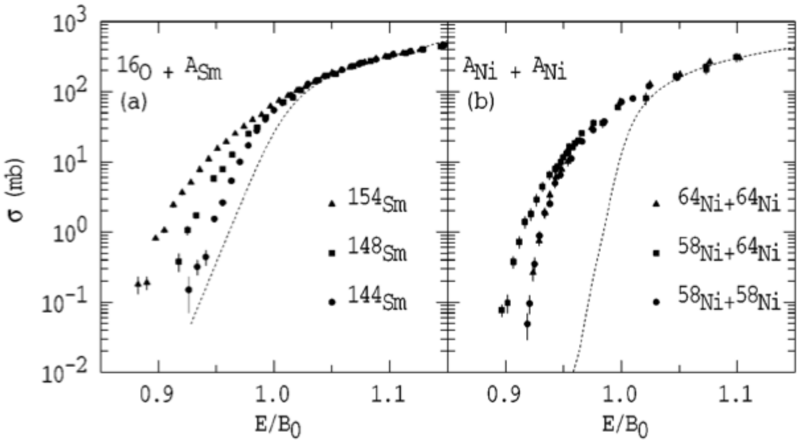

FIGURE 2.3: On the left, the excitation function of $^{16}$O on Sm isotopes [17], where a marked increase of the cross section with increasing mass and isotope deformation is observed. On the right, the excitation functions of $^{58}$Ni + $^{58}$Ni, $^{58}$Ni + $^{64}$Ni and $^{64}$Ni + $^{64}$Ni [18], where the influence of the transfer channels on the fusion process is highlighted. The dashed curves correspond to the excitation function in the one-dimensional barrier model [25].

## 2.2 Coupled-channels formalism for heavy-ion fusion reactions

### 2.2.1 Coupling matrix

In order to formulate the coupled-channels model, it is necessary to consider a collision between two nuclei in the presence of coupling of the relative motion to a nuclear intrinsic motion $\xi$. The Hamiltonian is written as

$$H(r,\xi) = H_0(\xi) + T(r) + V(r) + V_{cpl}(r,\xi) \tag{2.28}$$

where $H_0(\xi)$ is the Hamiltonian describing the internal degrees of freedom, $V_{cpl}(r,\xi)$ is the coupling term, and $T(r) + V(r)$ is the one-dimensional Hamiltonian.
The stationary Schrödinger equation obtained is therefore

$$\left[-\frac{\hbar^2}{2\mu}\frac{d^2}{dr^2} + \frac{l(l+1)\hbar^2}{2\mu r^2} + V(r) - E\right]\Psi(r,\xi) = -\left[H_o(\xi) + V_{cpl}(r,\xi)\right]\Psi(r,\xi) \tag{2.29}$$

Denoting the functions $\chi_j(\xi)$ as the eigenstates of the intrinsic Hamiltonian $H_0(\xi)$, the corresponding eigenvalues $\epsilon_j$ indicate the energies of the intrinsic excitation states. The ensemble of eigenstates constitutes a complete orthonormal system for the Hilbert space, in which the solutions of Eq. 2.29 are defined. The function $\Psi(r,\xi)$ can be therefore expanded in the $\chi_j(\xi)$ eigenstates.

$$\Psi(r,\xi) = \sum_j \phi_j(r)\chi_j(\xi) \tag{2.30}$$

where $\phi_j(r)$ is the distorted wave of the relative motion of the j-th channel.
Using the Dirac formalism to express the eigenstate of the complete orthonormal

base of the intrinsic Hamiltonian (so that $H_0|j >= \epsilon_j|j >$), the wave function becomes:

$$\Psi(r) = \sum_j \phi_j(r)|j > \tag{2.31}$$

The equation 2.29 is therefore a set of coupled differential equations

$$\sum_j \left[ -\frac{\hbar^2}{2\mu}\frac{d^2}{dr^2} + \frac{l_j(l_j+1)\hbar^2}{2\mu r^2} + V(r) - E \right] \phi_j(r)|j >= -\sum_j \left[ H_o(\xi) + V_{cpl}(r,\xi) \right] \phi_j(r)|j > \tag{2.32}$$

Taking advantage of the orthonormality of the base of the eigenstates $|j >$, it is possible to apply the bra $< i|$ to the previous equation and obtain a new set of coupled equations which solutions are the wave functions $\phi(r)$ of the relative motion of the two nuclei.

$$\left[ -\frac{\hbar^2}{2\mu}\frac{d^2}{dr^2} + \frac{l_i(l_i+1)\hbar^2}{2\mu r^2} + V(r) - E \right] \phi_i(r) = -\sum_j M_{ij}\phi_j(r) \tag{2.33}$$

In the equation above, $M_{ij}$ are the coupling matrix elements among the eigenstates related to internal energy

$$M_{ij} = \epsilon_i \delta_{ij} + < i|V_{cpl}(r,\xi)|j > \tag{2.34}$$

The matrix $M_{ij}$ is symmetric and in case it is diagonal it can be factored allowing the decoupling of the solutions. In this perspective, some approximations have to be adopted.

### 2.2.2 Approximations

The coupled channel model provides a system of differential equations where each $i$-th channel denotes an intrinsic state. In particular, each equation associated with the partial wave $l_i$ has to be solved by considering all the coupling orders between channels leading to the same total angular momentum of the system J.

The equations can be solved by numerical means, by using dedicated programs such as CCFULL [26], or by decoupling them. One of the main problems is the number of channels that must be included to describe the reaction, which can be very large, making the decoupling difficult and the numerical calculations long. Therefore, approximations are used which reduce the number of channels and simplify the calculations.

#### Incoming Wave Boundary Conditions

The internuclear potential $V(r)$ is supplemented by an imaginary part $iW(r)$, which simulates the absorption in the fusion reaction channel. The Schrödinger equation to be solved is therefore

$$\left( -\frac{\hbar^2}{2\mu}\frac{d^2}{dr^2} + \frac{l(l+1)\hbar^2}{2\mu r^2} + V(r) - iW(r) - E \right) u_l(r) = 0 \tag{2.35}$$

In order to solve the equation for each partial wave $l$, typical scattering process boundary conditions are applied:

$$u_l(r) \sim r^{l+1} \qquad r \to 0 \tag{2.36}$$

$$u_l(r) \cong \frac{i}{2}\left[H_l^{(+)}(kr) - S_l H_l^{(-)}(kr)\right] \qquad r \to \infty \tag{2.37}$$

where $H_l^{(+)}$ and $H_l^{(-)}$ are the outgoing and incoming Coulomb wave functions and $S_l$ is the nuclear S-matrix. The wave number associated with the energy E is $k = \sqrt{2\mu E/\hbar^2}$.

If the imaginary part of the potential, $iW(r)$, is confined well inside the Coulomb barrier, the total absorption cross section can be regarded as the fusion cross section [8]

$$\sigma_{fus}(E) \sim \sigma_{abs}(E) = \frac{\pi}{k^2}\sum_l 2(l+1)(1-|S_l|^2) \tag{2.38}$$

In heavy-ion fusion reactions, instead of imposing the regular boundary condition, Eq. 2.36, the so called incoming wave boundary condition (IWBC) is often applied without introducing the imaginary part of the potential, $iW(r)$ [3]. IWBC corresponds to the case where there is strong absorption within the inner region of the potential, so that the incoming flux never returns back. Under this condition, the wave function has the following form:

$$u_l(r) = \sqrt{\frac{k}{k_l(r)}} T_l exp\left[-i\int_r^{r_{abs}} k_l(r')dr'\right] \qquad r \le r_{abs} \tag{2.39}$$

where $T_l$ is the transmission coefficient and $r_{abs}$ refers to the the absorption radius, which is assumed to be inside the Coulomb barrier. Conventionally, $r_{abs}$ corresponds to the position of the interaction potential minimum [26].The local wave number for the energy of the $l$-th partial wave is:

$$k_l(r) = \sqrt{\frac{2\mu}{\hbar^2}\left(E - V(r) - \frac{l(l+1)\hbar^2}{2\mu r^2}\right)} \tag{2.40}$$

The IWBC corresponds to the case where there is strong absorption in the inner region so that the incoming flux never returns. For heavy-ion fusion reactions, the final result is not sensitive to the choice of the absorption radius $r_{abs}$. Equation 2.38 is then transformed to

$$\sigma_{fus}(E) = \frac{\pi}{k^2}\sum_l 2(l+1)P_l(E) \tag{2.41}$$

where $P_l$(E) is the penetrability for the $l$-wave scattering, defined as

$$P_l(E) = 1 - |S_l|^2 = |T_l|^2 \tag{2.42}$$

The IWBC is valid for reactions between heavy ions, where there is a strong absorption inside the Coulomb barrier.

#### Iso-centrifugal approximation

The iso-centrifugal approximation [26, 27] allows to reduce the number of incoming channels and consequently the dimension of the coupling matrix to be solved.

In the coupled channel method, an excited state of internal spin $I$ generates $I+1$ channels when it is coupled to the angular momentum $l_i$ of the relative motion, since each orbital angular momentum of the type $l_i' = |l_i - I|, .., |l_i + I|$ satisfies the condition $J = I + l_i$.

The approximation reduces the number of channels by assuming that the orbital angular momentum, or equivalently the centrifugal potential, is the same in all reaction channels

$$\frac{\hbar^2}{2\mu}\frac{l_i(l_i+1)}{r^2} \approx \frac{\hbar^2}{2\mu}\frac{J(J+1)}{r^2} \tag{2.43}$$

Under this condition, the coupling of the spin $I$ to the orbital angular momentum $l$ can be neglected and consequently only one effective channel for each excited state (instead of I + 1) is taken into account.

The approximation is successfully applied in collisions between heavy ions, because of their large reduced mass and barrier radius, and in general in inelastic couplings of various complexity, both rotational and vibrational.

### Adiabatic approximation and constant coupling

Two other approximations allow to analytically reveal the univocal correspondence between channels and barriers and, as the previous ones, simplify the decoupling of the equations and their resolution.

The adiabatic approximation (or "sudden limit approximation") [27] is based on the assumption that the tunneling occurs much faster than the intrinsic motion, so that the nuclear structure is not perturbed during the crossing of the Coulomb barrier. The internal excitation energies can then be neglected with respect to the coupling interaction. This condition is obtained by placing $\epsilon_i \simeq 0$ in the $M_{ij}$ matrix.

$$M_{ij} = \epsilon_i\delta_{ij} + < i|V_{cpl}(r,\xi)|j > \simeq < i|V_{cpl}(r,\xi)|j > \tag{2.44}$$

However, its validity is verified only for strongly deformed nuclei [25].
Assuming that the reduced mass and the potential energy are the same for all the channels, it is possible to factorize the coupling potential in two terms which depend separately on the intrinsic and relative motions.

$$< i|V_{cpl}(r,\xi)|j > = < i|F(r)\Gamma(\xi)|j > = F(r)\Gamma_{ij} \tag{2.45}$$

The approximation of the constant coupling is based on the assumption that the form factors of all channels have the same radial dependence as $F(r)$. Under this condition, by indicating with $F(r_b)$ the value at the barrier where the coupling is stronger so that $F(r) = F(r_b)$, the following simplification is obtained

$$\left[-\frac{\hbar^2}{2\mu}\frac{d^2}{dr^2} + V(r) - E\right]\phi_i(r) = -\sum_j M_{ij}\phi_j(r) = -F(r_b)\sum_i \Gamma_{ij}\phi_j(r) \tag{2.46}$$

This further approximation, together with the previous ones, allows to diagonalize the matrix through the use of a unitary transformation. By employing a unitary matrix $U$ independent of the relative distance $r$, the coupling matrix is diagonalized with respect to a base of eigenfunctions $\chi_j(r)$, where $\lambda_j$ are the associated eigenvalues.

$$\chi_j(r) = \sum_i U_{ji}\phi_i(r) \qquad\qquad \sum_{mn} U_{im}M_{mn}U^{\dagger}_{nj} = \delta_{ij}\lambda_j \tag{2.47}$$

A system of decoupled second-order differential equations which satisfy the IWBC boundary conditions is obtained:

$$\left[-\frac{\hbar^2}{2\mu}\frac{d^2}{dr^2} + V(r) + \lambda_i F(r) - E\right]\chi_i(r) = 0 \tag{2.48}$$

The problem has been therefore reduced to solving a set of decoupled equations, each corresponding to a different inelastic channel $i$ and to which a certain potential $V(r) + \lambda_i F(r)$ is associated. By using these approximations, the coupled-channel method replaces the single Coulomb barrier of the one-dimensional model with a spectrum of barriers $V(r) + \lambda_i F(r)$, to each of which a transmission coefficient is assigned $T_l(E, V(r) + \lambda_i F(r))$.
The total transmission coefficient is obtained as the weighted sum of the transmission coefficients of each barrier associated with the single reaction channels

$$T_l(E) = \sum_i |U_{i1}|^2 T_l(E, V(r) + \lambda_i F(r)) \tag{2.49}$$

The factor $W_i = |U_{i1}|^2$ represents the contribution of the $i$-th barrier to the fusion cross section and is obtained by the superposition of the incoming wave function and the ones of the considered outgoing channels $| < i|1 > |^2$. The fusion cross section is therefore expressed as the weighted sum of the cross sections of each channel

$$\sigma^{fus}(E) = \sum_i W_i \sigma_i^{fus} \tag{2.50}$$

where $\sigma_i^{fus}$ corresponds to the expression of 2.16, employing the potential of the $i$-th barrier $V(r) + \lambda_i F(r)$.

$$\sigma_i^{fus}(E) = \sum_l \pi \lambda\!\!\!^{-2}(2l+1) T_l(E, V(r) + \lambda_i F(r)) \tag{2.51}$$

### 2.2.3 Example of two-channel coupling

As an example of the application of the model described above, a coupled system with only two channels is considered. In particular, the coupling is between an elastic channel and a negative $Q$-value channel, assuming a constant form factor $F$. The decoupled equations for the present system are:

$$\begin{cases} \left[-\frac{\hbar^2}{2\mu}\frac{d^2}{dr^2} + V(r) + \lambda_+ F - E\right]\chi_+(r) = 0 \\ \left[-\frac{\hbar^2}{2\mu}\frac{d^2}{dr^2} + V(r) + \lambda_- F - E\right]\chi_-(r) = 0 \end{cases} \tag{2.52}$$

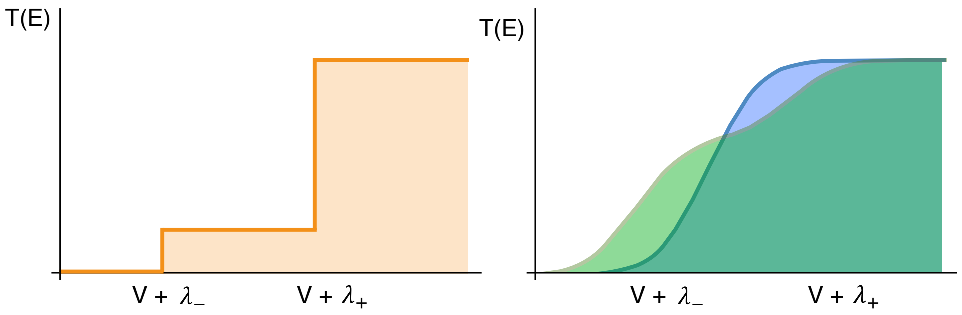

FIGURE 2.4: Transmission coefficient as a function of the energy in the classical (left panel) and quantum (right panel) approach to the two-channels coupling. The no-coupling transmission coefficient in the quantum treatment (blue line) is shown on the right.

where $\lambda_\pm$ and $\chi_\pm(r)$ are the eigenvalues and the eigenfunctions of the diagonalized coupling matrix, respectively.
The coupling matrix for this system is

$$M = \begin{pmatrix} 0 & F \\ F & -Q \end{pmatrix} \tag{2.53}$$

where $-Q = \epsilon$ is the intrinsic excitation energy of the state coupled to the elastic channel. The eigenvalues and their weight factors are:

$$\lambda_\pm = \frac{-Q \pm \sqrt{Q^2 + F^2}}{2} \qquad\qquad W_\pm = \frac{F^2}{F^2 + \lambda_\pm^2} \tag{2.54}$$

The results show that the single barrier is split into two barriers. One barrier is higher than the single barrier $V(r)$ by an amount $\lambda_+$, the second one is lower by the quantity $\lambda_-$. Each barrier has a weight factor $W_+$ and $W_-$.
The transmission coefficient is therefore (classically):

$$T = \begin{cases} 0 & E < V_b + \lambda_- \\ W_- & V_b + \lambda_- < E < V_b + \lambda_+ \\ 1 & E > V_b + \lambda_+ \end{cases} \tag{2.55}$$

and is shown in Fig. 2.4 (left). The range of energies for which the penetration of barrier is allowed is extended with respect to the one-dimensional model.
The increase of the transition probability occurs both for positive and negative $Q$-values with different weight factors. Indeed, for $Q > 0$, as shown by Eq. 2.54, the greater weight is associated with the barrier $V_b + \lambda_+$. On the contrary, in the case of $Q < 0$ the lower barrier ($V_b + \lambda_-$) takes the greater weight.

### 2.2.4 CCFULL code

The CCFULL code [26] calculates the fusion cross section and the angular momentum of the compound nucleus, taking into account the effect of couplings between the relative motion of the two interacting nuclei and intrinsic degrees of freedom on fusion. The standard way to address the effects of these couplings is to numerically solve the coupled-channel equations, including all the relevant channels.

The program CCFULL includes the couplings to full order, without introducing the expansion of the coupling potential (no linear coupling approximation [26]). In order to reduce the dimension of the coupled-channel equations, the program employs the isocentrifugal approximation. The code fully takes into account the finite excitation energies of intrinsic motions, includes Coulomb excitations and uses the IWBC inside the Coulomb barrier, adopting the minimum position of the Coulomb pocket inside the barrier for $r_{min}$.

CCFULL directly integrates coupled second-order differential equations using the modified Numerov method [26] and a barrier penetrability is calculated for each partial wave.
The cross section and angular momentum of the compound nucleus are then obtained for all partial waves

$$\begin{aligned} &\sigma^{fus}(E) = \textstyle\sum_J \sigma_J(E) = \pi\lambda^2 \sum_J (2J+1) T_J(E) \\ &< l >= \textstyle\sum_J J\sigma_J / \sum_J \sigma_J \end{aligned} \tag{2.56}$$

The employed nuclear potential follows a Woods-Saxon parameterization, while no imaginary potential is used.

The input file contains the parameters specifying the system, which are the atomic number and mass of the nuclei, and the nuclear potential parameters of the entrance channel, that is, the potential depth $V_0$, the radius $R_0$ and the diffuseness $a_o$. To take into account the vibrational motions, for each level the excitation energy $E_x$, the deformation parameter $\beta_\lambda$, the multiplicity of the vibration coupling $\lambda$ and the number of considered phonons $n$ are specified. The deformation parameter is related to the reduced transition probability $B(E\lambda)$ of the electromagnetic decay from the excited state $\lambda^\pi$ to the ground state by:

$$\beta_\lambda^2 = \left(\frac{4\pi}{3Ze^2R^\lambda}\right)^2 4\pi B(E\lambda) \tag{2.57}$$

with Z and R being the nuclear charge and radius, respectively.
In the case of rotational coupling, the excitation energy of the first $2^+$ state of the rotational band, the quadrupole deformation $\beta_2$ and the hexadecapole $\beta_4$ deformation parameters and the number of levels in the band have to be specified.
For the transfer of nucleons it is necessary to provide the $Q$-value of the transfer channel, the strength of the coupling and the number of transferred nucleons. The code allows also to include in the calculations all the possible mutual excitations.

### Excitation of surface modes

The coupling of the surface excitation states of a nucleus are generated by the interaction $V(r-\delta R)$, where $V(r)$ is the ion-ion potential and $\delta R$ is the surface distortion, expressed as

$$\delta R = \sum_{n\lambda\mu} R\alpha_{n\lambda\mu} Y_{\lambda\mu}(r) \tag{2.58}$$

where $\alpha_{n\lambda\mu}$ is the static or dynamic deformation amplitude. The expression above can be simplified, in the rotating frame, if the direction $\hat{r}$ between the colliding nuclei defines the z axis, which implies that $\mu = 0$

$$\delta R = \sum_{n\lambda} R\alpha_{n\lambda 0}\sqrt{\frac{2\lambda+1}{4\pi}} \tag{2.59}$$

Under this condition, it is possible to define the matrix element of the surface distortion amplitude between the ground state and the first excited state. This expression holds for both static and dynamic deformations, i.e. rotational and vibrational excitations

$$< n\lambda|\delta R|00 >= \frac{\beta_{n\lambda}R}{\sqrt{4\pi}} \tag{2.60}$$

Both Coulomb and nuclear potentials can be developed with respect to the deformation parameter $\delta R$. In particular for the Coulomb interaction a first-order truncation is sufficient and the non-diagonal elements of the coupling matrix are

$$\delta V_C = \sum_n \frac{3Z_1Z_2e^2}{2\lambda+1}\frac{R^\lambda}{r^{\lambda+1}}\alpha_{n\lambda 0}\sqrt{\frac{2\lambda+1}{4\pi}} \tag{2.61}$$

First-order truncation has been also performed for nuclear potential, however it has been demonstrated that nonlinear couplings significantly affect the shape of fusion barrier distributions [28]. The CCFULL program allows to calculate the coupling of the surface excitations to all orders [29]

$$\begin{aligned} &U(r-\delta R) \sim U(r)+\delta V_N \\ &\delta V_N = -\tfrac{dU}{dr}\delta R + \tfrac{1}{2}\tfrac{d^2U}{dr^2}[(\delta R)^2 - <0|(\delta R)^2|0>] \end{aligned} \tag{2.62}$$

where the second-order term is null at the ground state.
The program is suitable for the treatment of both light and heavy ion fusion, where multiphonon excitations are crucial. The main excitations that influence the fusion reaction between heavy ions are the low energy states $2^+$ and $3^-$, and occasionally also the $4^+$ and $5^-$ states.

### Vibrational coupling

CCFULL considers the coupling of vibrational states by parameterizing the vibrational potential through an harmonic oscillator. This approximation is performed by introducing a dynamic operator which depends on the operator of creation (annihilation) $a^\dagger_{\lambda 0}$ ($a_{\lambda 0}$) of phonons and which is added to the radius parameter of the Woods-Saxon potential.

$$R_{00}+\hat{O} = R_0 + \frac{\beta_\lambda}{\sqrt{4\pi}} R_t (a^\dagger_{\lambda 0} + a_{\lambda 0}) \tag{2.63}$$

where $\lambda$ indicates multipolarity, $\beta_\lambda$ the deformation parameter and the radius of the target $R_t = r_{cp} A_t^{1/3}$ is expressed as a function of the coupling radius.
The matrix element between the $n$-phonons $|n>$ state and $m$-phonons $|m>$ is

$$\hat{O}_{nm} =< n|\hat{O}|m >= \frac{\beta_\lambda}{\sqrt{4\pi}} R_t (\sqrt{m}\delta_{n,m-1} + \sqrt{n}\delta_{n,m+1}) \tag{2.64}$$

Diagonalizing the dynamic operator $\hat{O}$ it is possible to derive the elements of the nuclear potential matrix

$$V^N_{nm} =< n|V^N(r,\hat{O})|m > -V^N_0 \delta_{n,m} \tag{2.65}$$

where the term $V^N_0 \delta_{n,m}$ avoids a double counting of the same term in the diagonal components.
As mentioned before, the code employs the linear coupling approximation for the coupling of the Coulomb potential with the vibrational degrees of freedom, obtaining the matrix element $V^C_{nm}$ which is added to the nuclear element $V^N_{nm}$.

$$V^C_{nm} = \frac{\beta_\lambda}{\sqrt{4\pi}} \frac{3}{2\lambda+1} Z_P Z_T e^2 \frac{R_T^\lambda}{r^{\lambda+1}} (\sqrt{m}\delta_{n,m-1} + \sqrt{n}\delta_{n,m+1}) \tag{2.66}$$

In realistic cases the phonon spectrum is truncated to a certain level and therefore the intrinsic motion deviates from the harmonic limit, even when the levels are equally spaced and the electromagnetic transitions do not alter the linear approximation. However, the discussed matrix formalism still provides a convenient and powerful technique to evaluate the coupling matrix elements.

### Rotational coupling

In the case of deformed nuclei, the program allows to include the coupling with the rotational excitation states. The used method is very similar to the one described previously for the vibrational case. The target radius in the nuclear potential is changed to a dynamical operator $\hat{O}$

$$R_{00} + \hat{O} = R_0 + \beta_2 R_t Y_{20} + \beta_4 R_t Y_{40} \tag{2.67}$$

where R$_t$ is parametrised as r$_{cpl}$A$_T^{1/3}$ , and $\beta_2$ and $\beta_4$ are the quadrupole and hexadecapole deformation parameters of the deformed target nucleus, respectively. Following this replacement, the matrix element of the coupling Hamiltonian between the $|n >= |I0 >$ and $|m >= |I'0 >$ states of the ground state rotational band of the target can be calculated. For this purpose the dynamical operator is diagonalized and the matrix elements result

$$\begin{aligned} \hat{O}_{II'} = \sqrt{\tfrac{5(2I+1)(2I'+1)}{4\pi}}\beta_2 R_t \begin{pmatrix} I & 2 & I \\ 0 & 0 & 0 \end{pmatrix}^2 + \\ + \sqrt{\tfrac{9(2I+1)(2I'+1)}{4\pi}}\beta_4 R_t \begin{pmatrix} I & 4 & I \\ 0 & 0 & 0 \end{pmatrix}^2 \end{aligned} \tag{2.68}$$

By introducing these elements into the potential representation, the coupling matrix elements of nuclear potential are expressed as

$$V_{nm}^N =< n|V^N(r,\hat{O})|m > -V_0^N \delta_{n,m} = \sum_{\alpha} < I0|\alpha >< \alpha|I'0 > V_N(r,\lambda_\alpha) - V_0^N \delta_{n,m} \tag{2.69}$$

For the Coulomb interaction of the deformed target, the program includes up to the second order with respect to $\beta_2$ and to the first order of $\beta_4$. At variance with the nuclear couplings, the higher order couplings of the Coulomb interaction play a minor role.

$$\begin{aligned} V_{mn}^C = \tfrac{3Z_P Z_T}{5}\tfrac{R_T^2}{r^3}\sqrt{\tfrac{5(2I+1)(2I'+1)}{4\pi}}(\beta_2 + \tfrac{2}{7}\sqrt{\tfrac{5}{\pi}}\beta_2^2) \begin{pmatrix} I & 2 & I \\ 0 & 0 & 0 \end{pmatrix}^2 + \\ + \tfrac{3Z_P Z_T}{9}\tfrac{R_T^4}{r^5}\sqrt{\tfrac{9(2I+1)(2I'+1)}{4\pi}}(\beta_4 + \tfrac{9}{7}\beta_2^2) \begin{pmatrix} I & 4 & I \\ 0 & 0 & 0 \end{pmatrix}^2 \end{aligned} \tag{2.70}$$

The total coupling matrix element is given by the sum of V$_{mn}^N$ and V$_{mn}^C$.
The limit of the rotational coupling obtained this way consists in the treatment of the nucleus as a pure quantum rigid rotator.

### Transfer coupling

Recent studies have highlighted the influence of transfer processes on the fusion reactions at sub-barrier energies, where an enhancement of the cross sections is observed with respect to the CC calculations including the coupling to the vibrational and rotational states.
CCFULL includes in the CC calculations the coupling of the pair-transfer between the ground states of the interacting nuclei. In this perspective, a macroscopic form factor is included [8]

$$F_{trans}(r) = F_t \frac{dV_0^N}{dr} \tag{2.71}$$

where F$_t$ is the coupling strength.

## 2.3 Barrier distribution

The barrier distribution allows to reveal detailed structures in the energy dependence of the measured fusion cross sections at energies close to the Coulomb barrier. Indeed, the barriers show up significant differences among different systems, according to the structure of the interacting nuclei or to the dynamics of the reaction.

Rowley et al. [6] proposed a method to directly extract from the experimental fusion cross sections the barrier distribution, which is defined as the second derivative of the energy-weighted cross section.

$$D(E) \sim \frac{d^2(E\sigma_{fus}(E))}{dE^2} \tag{2.72}$$

This expression can be obtained starting from the estimate of the fusion cross section in the presence of channel couplings, which is expressed as the sum of the cross sections relative to the single barriers $B_i = V(r) + \lambda_i$

$$\sigma_{fus}(E) = \sum_i W_i \sigma_i^{fus}(E, V + \lambda_i) \tag{2.73}$$

where $W_i$ is the weight factor of each cross section $\sigma_i^{fus}$ (see Eq. 2.49).
If the fusion cross section is assumed to be a continuous distribution, the sum can be replaced with an integral

$$\sigma_{fus}(E) = \int_0^\infty \sigma^{fus}(E, B) D(B) dB \tag{2.74}$$

with the normalization condition $\int_0^\infty D(B)dB = 1$.
The fusion cross section $\sigma^{fus}(E, B)$ is linked to the tunnelling of the barrier $B$. The amount $D(B)$ is defined assuming that for each $i$-th channel the fusion takes place only after the crossing of the corresponding barrier $B_i$. $D(B)$ can therefore be expressed as the discrete spectrum of the barriers obtained by the coupling of each reaction channel with a barrier $B_i$.

$$D(B) = \sum_i W_i \delta(B - B_i) \tag{2.75}$$

In the classical treatment of the potential barrier, the transmission coefficient is a step function of the energy (as shown in the example of Fig. 2.4 left panel) and for each single barrier the fusion cross section weighted in energy is

$$E\sigma_{cl}^{fus}(E, B) = \begin{cases} \pi R^2 (E - B) & E > B \\ 0 & E < B \end{cases} \tag{2.76}$$

The second derivative, at energies above the barrier, is

$$\frac{d^2(E\sigma_{cl}^{fus}(E, B))}{dE^2} = \pi R^2 \delta(E - B) \tag{2.77}$$

By calculating the second derivative of the energy-weighted cross section of Eq. 2.74 and applying it to the classical case (Eq. 2.77), the previous $D(E)$ definition is obtained:

$$\frac{1}{\pi R^2}\frac{d^2(E\sigma_{cl}^{fus}(E))}{dE^2} = \frac{1}{\pi R^2}\int \frac{d^2(E\sigma_{cl}^{fus}(E,B))}{dE^2}D(B)dB \tag{2.78}$$

$$= \int \delta(E-B)D(B)dB = D(E) \tag{2.79}$$

For a complete treatment of the problem it is necessary to introduce quantum mechanical effects related to barrier penetration, which are dominant at sub-barrier energies and are neglected by the classical model. Quantum tunneling can be included by employing the Wong formula (Eq. 2.25), which allows to obtain the following expression of the energy-weighted cross section

$$E\sigma^{fus}(E,B) = \frac{\hbar\omega R^2}{2} ln\left\{1+exp\left[\frac{2\pi}{\hbar\omega}(E-B)\right]\right\} \tag{2.80}$$

The second derivative of the weighted cross section is therefore

$$\frac{1}{\pi R^2}\frac{d^2(E\sigma^{fus}(E,B))}{dE^2} = \frac{2\pi}{\hbar\omega}\frac{e^x}{(1+e^x)^2} = G(E-B) \tag{2.81}$$

where $x = \frac{2\pi}{\hbar\omega}(E-B)$.
By integrating on the continuous barrier distribution, $D(E)$ in the quantum mechanical treatment can be expressed as

$$\frac{1}{\pi R^2}\frac{d^2(E\sigma^{fus}(E))}{dE^2} = \int \frac{2\pi}{\hbar\omega}\frac{e^x}{(1+e^x)^2}D(B)dB \tag{2.82}$$

$$= \int G(E-B)D(B)dB = D(E) \tag{2.83}$$

The barrier distribution is smeared out by the function $G(E-B)$.
Alike $\delta(E-B)$, $G(E-B)$ is peaked at E = B, is symmetric around that point, and has unit area. The only difference is its finite width, FWHM $\simeq 0.56\,\omega\hbar$.
Assuming that the barrier distribution $D(B)$ is discrete, to each peak corresponding to the function $G(E-B_i)$, having the same FWHM $\simeq 0.56\,\omega\hbar$, a channel of the reaction is associated. The spectrum of barriers $D(E)$ can therefore be expressed as

$$D(E) = \sum_i^N W_i G(E-B_i) = \frac{1}{\pi R^2}\frac{d^2(E\sigma_W^{fus}(E))}{dE^2} \tag{2.84}$$

The main difference between the two distributions of Eq. 2.75 and 2.84 is the width of the peak associated with each barrier. In the latter case the distribution is represented by a bell distribution with a defined structure and amplitude, so that the spacing between two successive barriers has to be greater than their single width at half height in order to be distinguishable as two different contributions.

### 2.3.1 Obtaining the barrier distribution from experimental data

The barrier distribution yields detailed insight into the influence of nuclear structure on the fusion process, especially at energies below the Coulomb barrier. Since the theoretical fusion cross section can be obtained analytically, the barrier distribution can be easily calculated with the method described in the previous section. On the contrary, the experimental cross sections can be determined only at a finite number

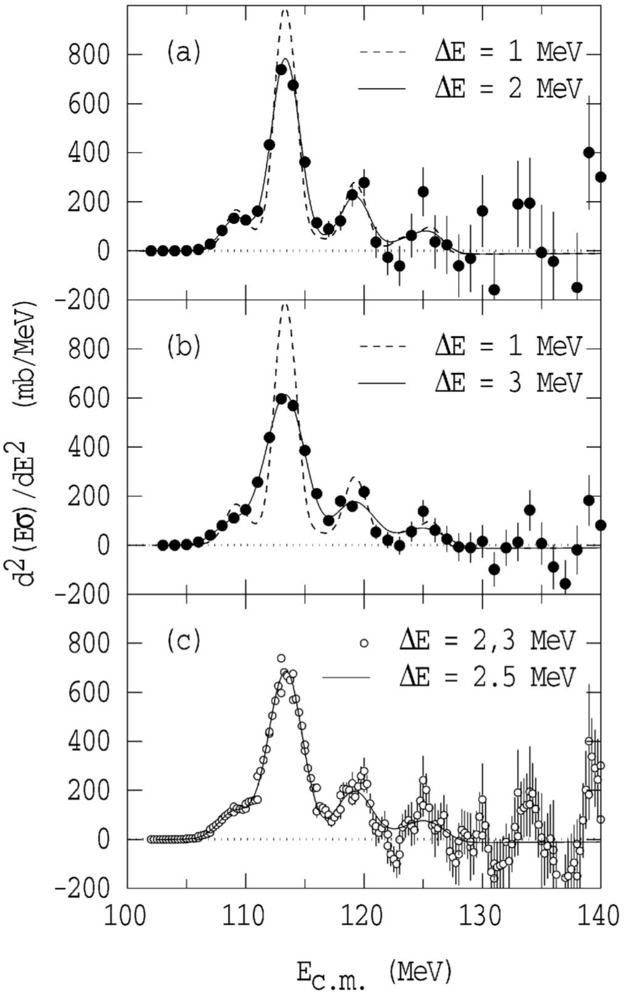

FIGURE 2.5: Barrier distributions of hypothetical systems [25], evaluated using the point difference formula with different energy steps.

of energies. From experimental or calculated cross sections with finite energy intervals, the second derivative of the weighted cross section E$\sigma$ can be obtained approximately from the successive determination of the first derivative using a point difference formula, where for three fusion cross sections $\sigma_{1,2,3}$ measured at the consecutive energies $E_{1,2,3}$, the second derivative at the average energy $(E_1 + 2E_2 + E_3)/4$, is given by

$$\frac{d^2(E\sigma(E))}{dE^2} \simeq 2\left(\frac{E_3\sigma_3 - E_2\sigma_2}{E_3 - E_2} - \frac{E_2\sigma_2 - E_1\sigma_1}{E_2 - E_1}\right)\left(\frac{1}{E_3 - E_1}\right) \tag{2.85}$$

For data with equal energy steps, $\Delta E = (E_3 - E_2) = (E_2 - E_1)$, the expresssion above can be semplified to

$$D(E) = \frac{d^2(E\sigma(E))}{dE^2} \simeq \left(\frac{E_3\sigma_3 - 2E_2\sigma_2 + E_1\sigma_1}{\Delta E^2}\right) \tag{2.86}$$

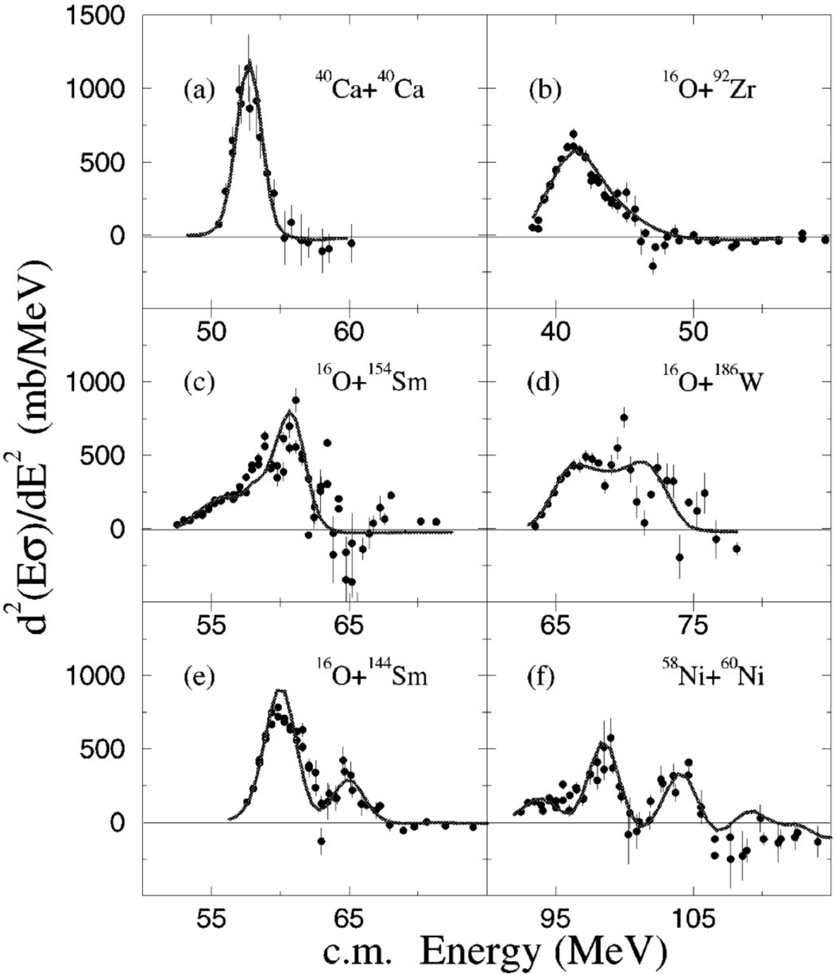

FIGURE 2.6: Barrier distributions for six different systems [25]. (a) The $^{40}$Ca + $^{40}$Ca system shows up the typical single barrier shape due to the spherical structure of the doubly magic $^{40}$Ca nucleus. (b) In the $^{16}$O + $^{92}$Zr a continuous distribution is observed although the theoretical result is a set of several discrete barriers very close in energy. (c) The $^{16}$O + $^{154}$Sm and (d) $^{16}$O + $^{186}$W show the typical continuous distribution for deformed nuclei, differing by the deformation parameter $\beta_4$ positive for $^{154}$Sm and negative for $^{186}$W. (e) The high energy peak in $^{16}$O + $^{144}$Sm is due to the coupling to the low energy phonon state in $^{144}$Sm. (f) The three-barriers structure of the system $^{58}$Ni + $^{60}$Ni is due to the complex surface vibrations induced in this reaction.

The statistical error $\delta_c$ associated with the second derivative at the energy E is obtained by the quadratic propagation of the absolute cross section uncertainties $\delta\sigma_i$

$$\delta_c = \left(\frac{E}{\Delta E^2}\right)[(\delta\sigma)_1^2 + 4(\delta\sigma)_2^2 + (\delta\sigma)_3^2]^{\frac{1}{2}} \tag{2.87}$$

In a measurement, the relative uncertainty $\delta\sigma/\sigma$ reaches minimum values with increasing the cross section, and therefore beyond this minimum the statistical uncertainty $\delta_c$ is proportional to the cross section and increases proportionally to the beam energy. Assuming this constant relationship the following expression is obtained

$$\delta_c \simeq \sqrt{6}\left(\frac{\delta\sigma}{\sigma}\right)\frac{E\sigma(E)}{(\Delta E)^2} \tag{2.88}$$

The barrier distribution is therefore well defined at lower energies where the cross section is smaller, despite that the relative uncertainty can be large, while it gets less defined when energy increases. The statistical uncertainty $\delta_c$ is inversely proportional to the energy step $\Delta E^2$, so that in principle it can be reduced by using larger energy intervals. On the other hand, a large value of $\Delta E$ smooths the extracted distribution by damping characteristic structures originating from couplings to different inelastic channels.

The choice of the energy step is therefore of great importance for a well-defined estimate of the barrier distribution. Usually, a good compromise between sensitivity and precision is to use different energy steps $\Delta E_i$: smaller steps at low energies, in order to highlight possible structures below the Coulomb barrier, and larger steps at higher energies to reduce the uncertainties.

Fig. 2.5 shows the barrier distributions of hypothetical systems [25], extracted using the point difference formula from cross sections estimated with CC calculations. The distributions obtained employing energy steps of 1 MeV are compared to the ones resulted from energy steps from 2 MeV to 3 MeV. As the energy step increases the distributions show increasingly damped structures at low energies (see again Fig. 2.5), while they are better defined at higher energies. The uncertainty, on the other hand, decreases as the energy step increases.

The measurements of the cross section from which the distribution of barriers is extracted require a high precision and accuracy. Indeed, with the point difference formula the second derivative is determined by the variations of the cross section of three neighboring points, and therefore the fluctuation of one measurement leads to a displacement of three points of the distribution.

The fusion barrier distributions have been extracted for many systems and have proven to be sensitive to the effects of channel couplings, providing a clear way of understanding their effects on the fusion process, as illustrated in Fig. 2.6.

Barrier distributions therefore renewed the interest in studies of heavy-ion subbarrier fusion reactions.

## 2.4 Fusion at deep-subbarrier energies

The availability of advanced set-ups allowed to extend the fusion cross sections measurements for several systems down to extremely low cross sections, in the range of a few nanobarn (nb). These experimental data showed that, although the coupled-channels approach resulted successfully in reproducing the excitation function for heavy ion reactions at energies above and below the barrier, the experimental cross sections at far sub-barrier energies were overestimated for a number of systems.

This phenomenon is named as "hindrance" and one of the first evidences is shown in Fig. 2.7 (a), where the experimental excitation function of the system $^{64}$Ni + $^{64}$Ni [18, 30] is hindered at deep-subbarrier energies compared to the standard coupled-channels calculations (dashed line).

Two different models have been proposed in order to describe the deep-subbarrier fusion hindrance.

The first model, proposed by Misicu and Esbensen [12, 32] and called "sudden approach", treats the nuclei density as frozen during the collision, assuming in this way

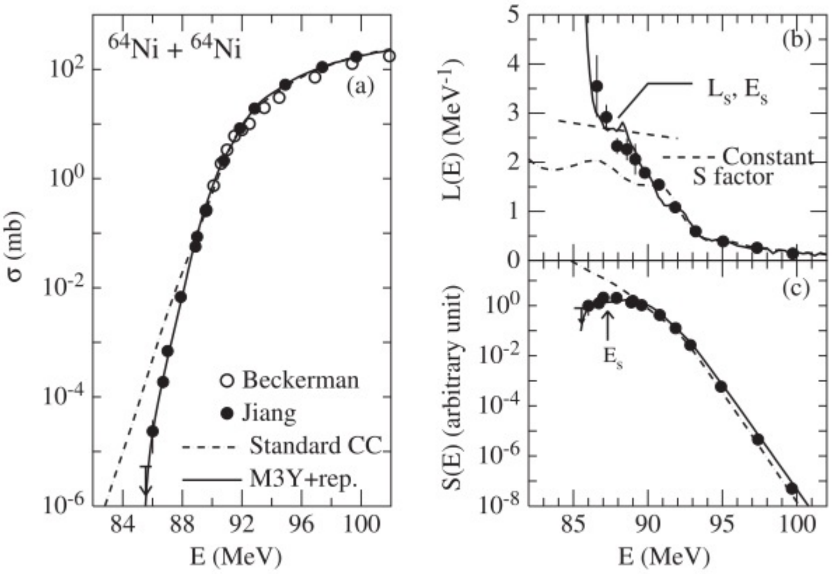

FIGURE 2.7: Excitation function (a), logarithmic derivative L(E) (b) and astrophysical S factor S(E) (c) of the system $^{64}$Ni + $^{64}$Ni [18, 30], where hindrance was observed in early experiments of this kind [31].

that fusion occurs rapidly. They suggest that the incompressibility of nuclear matter becomes effective at small internuclear distances, thus generating a repulsive core in the ion-ion potential, which is then much shallower than standard potentials (see Fig. 2.8). This hinders the fusion probability.

On the contrary, Ichikawa et al. [33] have proposed an "adiabatic approach" where the fusion proceeds through the formation of a neck between the colliding nuclei in the overlap region (Fig. 2.8). In this model, the fusion occurs in the time necessary for the density distribution to adjust to the optimal distribution and the hindrance originates from the tunneling of a one-body potential due to the neck formation. The two models, despite the origins of the deep-subbarrier hindrance are considerably different from each other, reproduce several experimental data equally well.

Hindrance typically shows up with varying intensities and distinct features in different systems. Two model independent representations of the measured cross section are therefore usually employed in order to highlight the appearance of hindrance: the logarithmic slope L(E) of the excitation function and the astrophysical S factor S(E).

The logarithmic derivative of the energy-weighted cross section L(E) represents the slope of the excitation function [7]

$$L(E) = \frac{d[ln(E\sigma)]}{dE} = \frac{1}{E\sigma}\frac{d(E\sigma)}{dE} \tag{2.89}$$

where $E$ is referred to the center of mass system. $L(E)$ increases as energy decreases, as shown in Fig. 2.7 (b).

The astrophysical S factor is a quantity widely used in nuclear astrophysics [35]. It is defined as:

$$S(E) = E\sigma(E)e^{2\pi\eta} \tag{2.90}$$

where $\eta$ is the Sommerfeld parameter: $\eta = (0.157Z_1Z_2)/\sqrt{\epsilon}$ and $\epsilon = E_{CM}/\mu$.

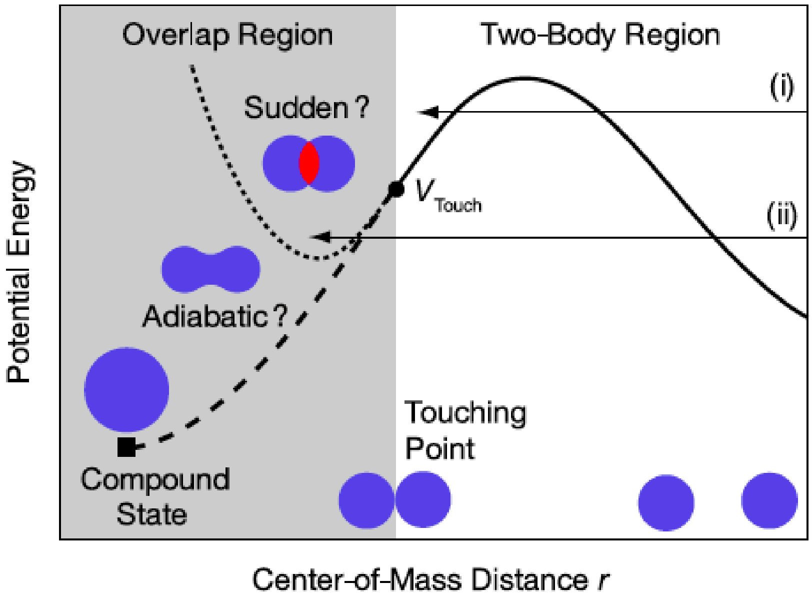

FIGURE 2.8: Scheme of a heavy ion-ion potential as a function of the center-of-mass distance r between colliding nuclei [34]. In the picture, the touching point of the colliding nuclei $V_{touch}$ and its compound state are shown with a circle and square point, respectively. The gray area represents the overlapping region of the colliding nuclei. The dashed and dotted lines indicate the potential energy curves for the adiabatic and sudden approach, respectively.

Plotting the S factor is a useful way of representing the trend of the excitation function in the energy region below the barrier, since $S$ is directly extracted from the cross sections. On the contrary, the logarithmic slope $L(E)$ and the barrier distribution $B(E)$ are derivatives of the excitation function and are therefore subject to larger experimental errors in the lower and higher energy regions, respectively, as shown in Fig. 2.6 and 2.7 (b). The two quantities $L(E)$ and $S(E)$ are algebraically related, since it is easy to show that the energy derivative of $S(E)$ is

$$\frac{dS(E)}{dE} = S(E)\left[L(E) - \frac{\pi\eta}{E}\right] \tag{2.91}$$

And thus the S factor develops a maximum at the energy where the slope reaches the value

$$L(E) = L_{CS}(E) = \frac{\pi\eta}{E} \tag{2.92}$$

The threshold for deep-subbarrier hindrance is conventionally taken at the energy where the astrophysical S factor reaches its maximum, as shown in Fig. 2.7 (c).

However, for some systems no maximum of the S factor can be observed in the measured energy range, so that the comparison of the experimental data with the results of standard CC calculations is necessary. An overprediction of the calculation with respect to experimental fusion cross section at low energies indicates the presence of hindrance. Moreover, there are several other cases where even the comparison of the experimental S factor with standard CC calculations does not indicate the presence of the hindrance [36]. This situation may be due to a different influence of nuclear structure and/or strong transfer couplings, which probably shift the hindrance threshold towards energies lower than measured ones.

## Chapter 3

# Fusion with exotic beams and the SPES project at LNL

## 3.1 Reactions with radioactive beams

The studies of near- and sub-barrier fusion reactions with stable ions have shown that there is a connection between the fusion mechanism and the underlying nuclear structure of projectile and target.
The availability of radioactive beams has greatly extended this investigation. Indeed, radioactive beams can be used to emphasize certain nuclear properties that are found to influence the fusion process. This can be exemplified by the cases of nuclei with weakly bound neutrons or protons, as the "halo nuclei" ($^{8}$B, $^{11}$Li, $^{15}$C, $^{17}$F), nuclei that exhibit strong transfer channels ($^{6,8}$He), nuclei with a large neutron excess (e.g., $^{132}$Sn, $^{134}$Te), or nuclei with a pronounced vibrational structure ($^{76}$Kr). In this section a few measurements employing medium-heavy or heavy exotic beams are described.

At Oak Ridge National Laboratory (ORNL) the Holifield Radioactive Ion Beam Facility (HRIBF) developed very neutron rich exotic beams as $^{132}$Sn and $^{130,134}$Te for a series of experiments on lighter targets as $^{58,64}$Ni and $^{40,48}$Ca. The aim of these measurements was the investigation of the effect of transfer couplings on sub-barrier fusion when the neutron excess is very large and consequently the transfer Q-values are positive even for 12-14 transferred neutrons.
Several experiments and theoretical analyses [25, 37, 38] gave strong evidences of sub-barrier fusion enhancement due to the coupling with nucleon transfer channels. A model-independent way to highlight these effects is the comparison of the fusion of calcium and zirconium isotopes [39, 40], where the $^{40}\mathrm{Ca}+{}^{96}\mathrm{Zr}$ system showed a significant increase in the sub-barrier fusion cross sections with respect to $^{40}\mathrm{Ca}+{}^{90}\mathrm{Zr}$. This has been attributed to the existence of positive Q-value neutron transfer channels for the $^{96}$Zr case [41]. The additional comparison with $^{48}\mathrm{Ca}+{}^{90,96}\mathrm{Zr}$ [39] and $^{40}\mathrm{Ca}+{}^{94}\mathrm{Zr}$ [40] systems confirmed this interpretation. In order to determine the presence of such enhancement also in heavy systems, the role of transfer has been investigated with both radioactive and stable heavy ion beams.

First experiments concerned $^{132}\mathrm{Sn}+{}^{64}\mathrm{Ni}$ [42] and, later on, $^{132}\mathrm{Sn}+{}^{58}\mathrm{Ni}$ and $^{130}\mathrm{Te}+{}^{58,64}\mathrm{Ni}$ [43]. The $^{132}\mathrm{Sn}+{}^{58,64}\mathrm{Ni}$ measurements were of particular interest since both neutron transfer couplings and the use of neutron-rich exotic beams have been predicted to provide enhanced fusion probabilities for the synthesis of superheavy elements [44, 45]. The two systems have been compared with stable Sn + Ni fusion measurements, where the Q-values for transfer of nucleons from the Ni to Sn nuclei are negative. Figure 3.1 (left panel) reports the excitation functions measured for various Ni+Sn systems in direct (with Ni stable beams) and inverse (with $^{132}$Sn beam) kinematics. The Q-values for two-neutron transfer are also indicated. The

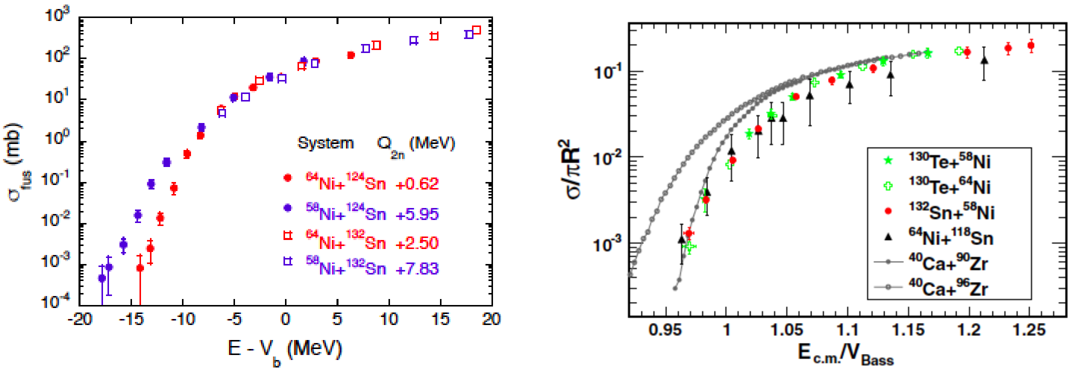

FIGURE 3.1: On the left, fusion excitation functions of the $^{58,64}$Ni + $^{124}$Sn and $^{132}$Sn + $^{58,64}$Ni systems, where the abscissa is the distance of the energy from the Akyüz-Winther Coulomb barrier [36]. On the right, comparison of the excitation functions of the $^{130}$Te + $^{58,64}$Ni, $^{132}$Sn + $^{58}$Ni, $^{64}$Ni + $^{118}$Sn, and $^{40}$Ca + $^{90,96}$Zr systems [43]. The fusion cross sections and center-of-mass energies were scaled by the geometrical cross section ($\pi R^2$) and Bass barrier height ($V_{Bass}$) respectively

comparison demonstrates no significant differences between the excitation functions of $^{132}$Sn + $^{58}$Ni and $^{132}$Sn + $^{64}$Ni and no enhancement with respect to $^{58,64}$Ni + $^{124}$Sn. These results indicate that for such rather heavy systems, the extra-enhancement possibly due to transfer couplings becomes appreciable only at rather low energies (cross sections below $\sim 1$ mb).

The $^{130}$Te + $^{58,64}$Ni fusion measurement showed that this situation is not limited to the Sn + Ni systems. The comparison of the Te + Ni and Sn + Ni excitation functions, shown in Fig. 3.1 (right panel), indicates no significant difference in the region of the barrier. Nevertheless, the presence of positive Q-value transfer channels does not seem to influence the fusion process of these systems, in contrast to the enhancements observed in lighter cases (see the $^{40}$Ca + $^{90,96}$Zr systems in Fig. 3.1, right panel).

Different results are obtained in the more recent measurements performed using the exotic beam on Ca targets. Figure 3.2 (left panel) reports the excitation function of the $^{134}$Te + $^{40}$Ca [46] and of several Sn + Ca systems involving stable and radioactive Sn isotopes [47]. The fusion excitation functions are separated into two groups according to the $^{40}$Ca and $^{48}$Ca targets, with a significant enhancement in the sub-barrier fusion for the reactions with $^{40}$Ca in comparison to $^{48}$Ca. As shown from the systematics of ground state Q-values in Fig. 3.2 (right panel), the two systems with only negative Q-values for neutron transfer channels, $^{132,124}$Sn + $^{48}$Ca, have smaller cross sections with respect to the other cases, where many positive Q-value transfer channels exist. The results suggest that the influence of the transfer channels is similar in the Te + Ca and Sn + Ca reactions, where they strongly influence sub-barrier cross sections when the Q-value is positive. This effect was already investigated and clarified in studies with stable beams [39], but the use of very neutron rich exotic beams like $^{132}$Sn and $^{134}$Te has allowed to confirm this evidence.

Additional experimental and theoretical efforts are needed to clarify the relationship between transfer and fusion reactions. Experimental measurements of both fusion and transfer cross sections will provide a deeper understanding of transfer couplings effects on fusion.

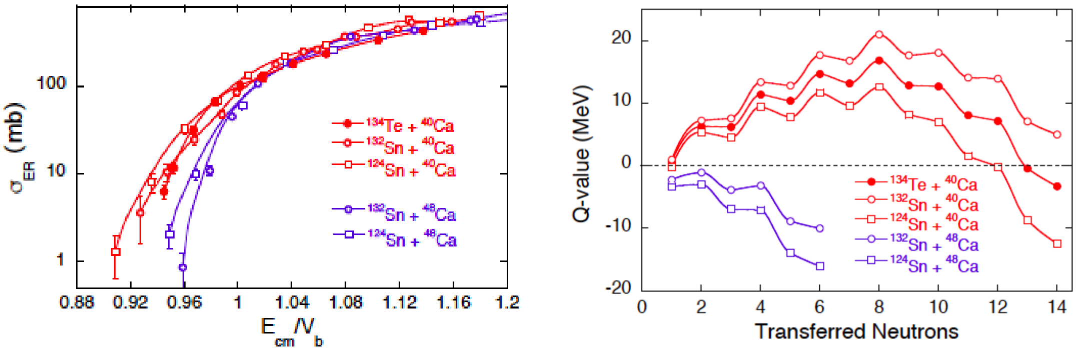

FIGURE 3.2: ER cross sections (on the left) and ground state Q-values for increasing number of transferred neutrons to the light fragments (on the right) for $^{134}$Te + $^{40}$Ca [46] and for $^{132,124}$Sn + $^{40,48}$Ca reactions [47]. On the left panel the energy scale is normalized to the Akyüz-Winther Coulomb barrier [36].

## 3.2 The SPES project

### 3.2.1 Techniques of radioactive beam production

Moving away from the valley of beta stability, the production of exotic nuclei runs into several difficulties originated by the extremely low production cross sections, the huge production of unwanted species in the same nuclear reaction and the very short half lives of the nuclei of interest.
Originally two complementary ways to make good quality radioactive ion beams (RIBs) were developed: the isotope separation on line (ISOL) technique and the in-flight separation technique (see Figs. 3.3 and 3.4, respectively).

In the ISOL technique an intense beam of neutrons or charged particles bombards a "thick" production target, producing a variety of radioactive nuclei. If these particles have a sufficiently long half-life, a high vapor pressure and do not chemically react within the production target, they will effuse out of the target and can be subsequentely ionized and accelerated in a secondary accelerator [48]. The RIBs produced in this way are characterized by beam-spot size, emittance and energy width that are similar to the ones of stable beams. The beam energy is, in most cases, in the range needed for measuring heavy-ion fusion reactions. The difficulties originating from isobaric impurities, which is a problem inherent to all secondary beams, can in some cases be overcome by using the mass selectivity of a cyclotron [49] or by accelerating a particular charge state. However, because of its chemical dependence and the finite effusion times, the isotopic access of the ISOL technique is limited. Among the facilities that presently use the ISOL technique ISOLDE (CERN), ISAC (TRIUMF, Canada) and SPIRAL (GANIL, France) are the most important ones.

In the in-flight separation method, a "thin" production target is bombarded by an energetic heavy-ion beam in inverse kinematics [51]. The reaction products are emitted in a narrow cone in the forward direction and are focused and transported through mass separators. At energies near and below 10 MeV/nucleon, direct reactions are often used and the reaction products can be selected and focused by solenoids or by a combination of solenoid, bunching resonator, and bending magnet (see Fig. 3.4 upper panel). At energies of a few tens to several hundreds MeV/nucleon,

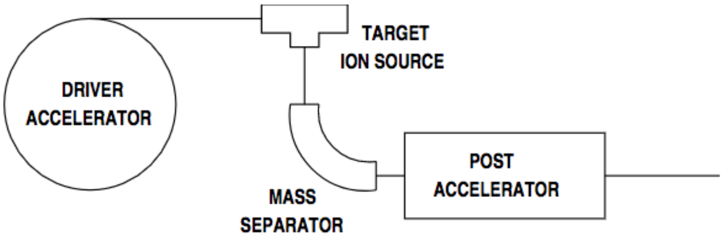

FIGURE 3.3: A schematic illustration of RIB production based on the ISOL technique [50].

the production reaction is essentially fragmentation, and more sophisticated fragment mass separators are used for filtering the beam (Fig. 3.4 bottom panel). Since there is no time delay for effusion out of the target, the widest range of secondary nuclei are produced without any chemical dependence. However, reaction mechanisms and target thickness introduce significant energy and angular spreads which lead to a poor energy resolution and large emittance of the secondary beam. Inflight beams are available at ANL (USA), ANU (Australia), CIAE (China), FSU (USA), INS Tokyo (Japan), LNL and LNS (Italy), Notre Dame (USA), RIBRAS (Brazil), and TAMU (USA).

The main difficulty present in all secondary beam experiments is the low beam intensity. Indeed, beam intensities are usually in the range of $10^3$–$10^7$ particles/s, which are $3-6$ orders of magnitude lower than what is typically available with stable beams. To overcome the limit coming from these low beam intensities, the detection systems have to assure high efficiencies or the experiments should be limited to reactions with large cross sections.

### 3.2.2 Selective Production of Exotic Species (SPES)

SPES is an INFN project to develop a second generation ISOL facility for reaccelerated exotic beams, mainly neutron-rich ions [52, 53]. The construction of SPES involves the two national laboratories: LNL and LNS and other INFN sites in Italy. The choice of the Laboratori Nazionali di Legnaro (LNL) as the facility site is due to the presence of the PIAVE-ALPI accelerator complex, which will be used as reaccelerator for the RIBs.

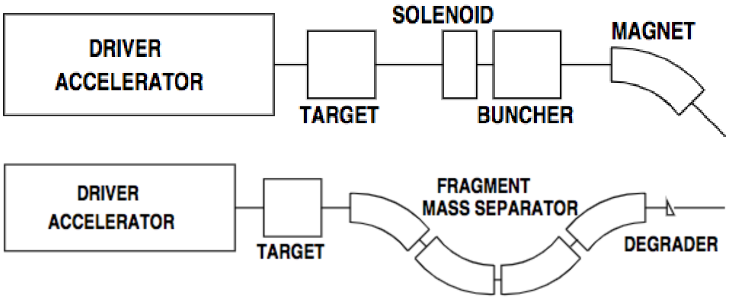

FIGURE 3.4: A schematic illustration of RIB production in-flight with direct (top) and fragmentation reactions (bottom) [50].

The key feature of SPES is to provide high intensity and high-quality beams of neutron-rich nuclei to perform forefront research in nuclear structure, reaction dynamics and interdisciplinary fields like medical, biological and material sciences.
The facility consists of a primary accelerator, the production target coupled to the ion source (TIS), the charge breeder, the beam transport system and the re-accelerator. A High Resolution Mass Spectrometer (HRMS) can be part of the transport system, according to the requirements of the experimental needs.
According to the ISOL method, the driver accelerator provides a primary beam which induces nuclear reactions inside a thick target. Because of the high temperature of the target-ion source system, the reaction products are extracted from the target by thermal process. Once the products reach the source, they are ionized (1+) ionized and extracted. After an isotopic selection and a further ionization to N+, the exotic beam is injected into a re-accelerator. The exotic isotopes will be re-accelerated by the ALPI superconducting linac up to energies of 10 AMeV and higher for masses in the region of A=130 amu, with an expected rate on the secondary target of $10^9$ pps for selected cases.

### Proton driver

The proton driver consists of a cyclotron (P70) able to supply proton beams with energy in the range of 40-70 MeV reaching a maximum current of 750 $\mu$A. Under these conditions, a maximum total beam power of 52 kW has to be managed. The use of a cyclotron as proton driver is very interesting from the point of view of a multi-user proton facility. Indeed it is equipped with two exit ports with stripper extraction, allowing for dual proton beam operation which permits to employ the accelerated beams for the production of RIBs and the development of applied physics at the same time.

### ISOL front-end

The ISOL front-end is the system which couples the proton beam with the UCx target, the ion source and the first part of the transport line of the exotic beam. At present the whole system is completed and is in operation at LNL for off-line tests.

The production target is carefully designed in order to optimize the radiative cooling, taking at the same time advantage of its high operating temperature (of the order of 2000°C). The adopted configuration maximizes the release efficiency and the heat dissipation. The target is made of 7 UCx disks (diameter and thickness of 40 and 1.3 mm, respectively), spaced in the axial direction in order to dissipate, by thermal radiation, the average power of 8 kW generated by the passing of the proton beam which induces nuclear reactions. The disks are placed in a cylindrical graphite box housed inside a tubular hollow tungsten ohmic heater. Indeed, both simulation and experimental tests showed that, because of the intense heat exchange by radiation, the energy released by the proton beam is not sufficient to make the system reach the operating temperature. The container provides an additional external power and allows a thermal control of the target operation. The target proved to be able to sustain the power necessary to produce $10^{13}$ fissions/s.

The neutron-rich fission fragments produced in the target are extracted by thermal motion and ionized to 1+ charge state by an ISOL source directly connected to the production target (TIS). The choice of the type of ion source to be used has been dictated by the efficiency and by its capability for selective ionization. In the first phase of the SPES the TIS is equipped with a Surface Ionization Source which can be

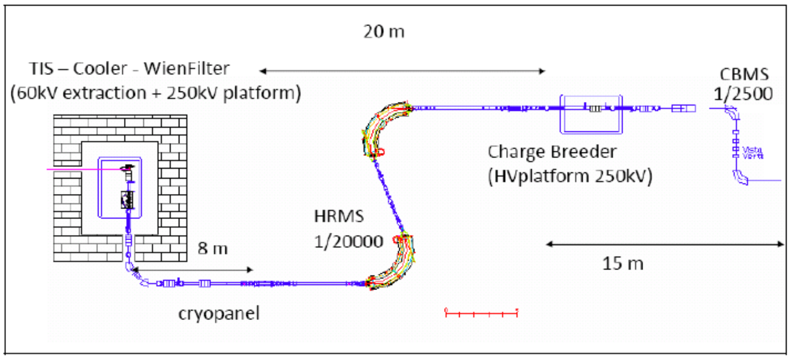

FIGURE 3.5: Scheme of the transport line for the SPES exotic beams [53].

coupled to a Resonant Ionization Laser Ion Source.
The isotopes produced in the target diffuse and then effuse through the transfer tube into the ionizer cavity, which is a tungsten tube (34 mm length, 3 mm inner diameter and 1 mm wall thickness) resistively heated to near 2000°C. From the cavity the isotopes undergo surface or laser ionization. In the surface ionization process an atom comes into contact with a hot metal surface and transfer a valence electron to the metal surface. This process is energetically favorable for elements with an ionization potential lower than the work function of the metal.
The laser resonant photo-ionization allows to achieve sufficiently selected ionization. This method produces beams as pure as possible (chemical selectivity) also for metal isotopes. In order to ionize elements with high ionization potential, as rare gases, the plasma source is needed, although the ionization occurs without any selectivity.

### Beam transport and re-acceleration

The secondary beam line transport system leads the radioactive beam provided by the ionization source to the low-energy experimental area and to the reaccelerator complex. Figure 3.5 reports a scheme of the transport line described below.

One typical problem of ISOL facility is to assure a high beam purity, since the extracted species are transported according to their A/q value. The low rigidity of the beam allows to adopt electrostatic quadrupoles to focus and transport the beam. The first mass selection is performed by a Wien Filter with 1/100 mass resolution, installed after the first electrostatic quadrupole triplet. The transfer line towards ALPI is equipped with several beam handling systems to purify the beam. A Beam Cooler and a High Resolution Mass Separator (HRMS) with 1/20000 mass resolution will be installed inside the new building.

Before the injection in the ALPI superconducting linac, an increase of the charge state from 1+ to N+ is necessary, which is performed employing of a Charge Breeder. After the Charge Breeder a second mass separator with $\sim 1/1000$ mass resolution, will be installed to remove the contaminants introduced by the Charge Breeder itself.

The exotic species will be reaccelerated by the acceleration complex PIAVE-ALPI. The linear accelerator ALPI is built of superconducting resonant cavities and can be operated also with the PIAVE injector which is based on an ECR source followed by a superconducting RFQ and by 8 dedicated resonant cavities able to accelerate ions

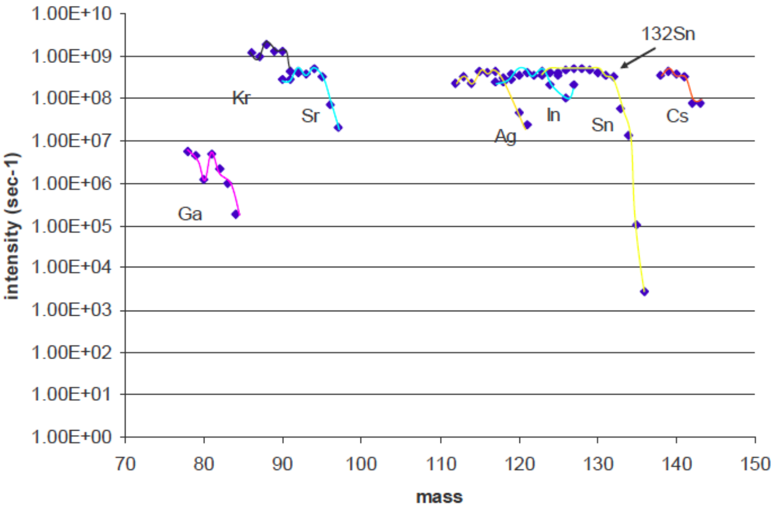

FIGURE 3.6: On-target intensities estimated considering emission, ionization and acceleration efficiencies of various isotopes [55].

with A/q ≤ 8.5 up to 1.2 AMeV. As mentioned before, ALPI accelerator will be able to push the RIBs energy up to 10 AMeV for masses in the region of A=130 amu.

In order to determine the intensities and the ion species available for experiments in the SPES facility, several factors have been taken into account. These estimations are based on simulations on the target release time, the fission fragment production yield and the diffusion and effusion of the exotic species. The simulations includes also the efficiencies of the source ionization and extraction, charge breeding, beam transport and reacceleration. The final estimated beam currents for the SPES facility are shown in Fig. 3.6 for some interesting species (more details can be found in [54]). In the first phase of SPES, the cyclotron will provide proton currents up to 5 $\mu$A on the UCx target. Under these conditions intensity of only $\sim 10^5$ pps will be available as re-accelerated beams.

### 3.2.3 Fusion with SPES beams

As mentioned in the previous section, studies of fusion reactions with exotic beams may highlight unexpected phenomena. It is therefore of our interest to start immediately an experimental activity in this field by exploiting selected very neutron rich beams produced by the SPES facility. Hence, we plan to use the low intensity beams ($\sim 10^5$ pps) which will be provided in the first phase of SPES.

Selenium, strontium and kripton beams, starting from the two isotopes $^{96}$Sr and $^{94}$Kr (provided with intensities of $10^5$ pps) will be used on $^{40}$Ca and $^{28}$Si targets. For these systems indeed neutron pick-up reactions with Q-values as large as +26 MeV are available. Furthermore, the low-energy structure of the two projectile nuclei $^{96}$Sr and $^{94}$Kr is well known so they can be included in CC calculations, in order to highlight possible effects of transfer on fusion.

When heavier beams like $^{134}$Sn and $^{136}$Te will be produced with comparable intensities, their fusion with lighter targets will be investigated. In particular, by measuring cross sections smaller than 1 mb, transfer couplings effects should show up more clearly, as described in Sec. 3.1. In the second phase of SPES, other attractive exotic beams like $^{94}$Sr, $^{92}$Kr, $^{132}$Sn, $^{134}$Te and $^{140,142}$Xe will be provided at higher intensities (ranging from $10^6$ to $10^8$ pps).

In order to perform the proposed fusion experiments, the beam quality (stability, energy definition and size of the spot on target) and its purity will be essential, especially below the Coulomb barrier. Furthermore, the reduced intensity of the radioactive beams of our interest, with respect to the stable beams usually provided by the XTU Tandem, makes it impossible to measure with low-efficiency set-ups. New detection systems which will assure an efficiency close to 100% are therefore foreseen for the upcoming SPES beams. In the next chapter the set-up used in LNL for near- and sub-barrier fusion reaction with stable beams and its upgrade for radioactive beams will be described.

# Chapter 4

# The fast ionization chamber

## 4.1 PISOLO: a set-up for the direct detection of evaporation residues

Fusion cross sections, when fusion-fission has a negligible probability, can be experimentally determined by direct detection of evaporation residues (ER) or by the detection of characteristic gamma-rays or/and light particles emitted during the deexcitation of the compound nucleus. The direct detection of ER is the most accurate method but it's very challenging and requires addressing various technical problems. The ER are forward peaked and must be physically separated from the direct beam and the intense flux of elastically scattered beam particles at small angles. This separation can be achieved using electric and/or magnetic fields.

At the Laboratori Nazionali di Legnaro (LNL) of INFN, the beam intensity of the TANDEM accelerator is typically around $10^{10}$ pps. Conventional particle detectors do not withstand such rates so that beam rejection is necessary in order to allow ER detection at small angles. Moreover, the fraction of beam particles involved in a fusion reaction is small. That fraction can be estimated as:

$$\frac{N_{fus}}{N_{beam}} = \frac{\sigma_{fus} N_A t}{A} \tag{4.1}$$

where $N_{fus}$ ($N_{beam}$) is the number of fusion events (beam particles), $t$ and $A$ are respectively the thickness (g/cm$^2$) and the mass number of the target and $\sigma_{fus}$ is the fusion cross section in cm$^2$ ( $N_A$ is the Avogadro number ). Typical values of the fraction are of the order of $\sim 10^{-7}$. Under these conditions, an electrostatic field applied perpendicularly to the direction of the particles between the target and the detection system allows to efficiently separate the beam from the ER, by exploiting the difference in electrical rigidity usually existing between ER and beam or beam-like particles.

The electrostatic deflector PISOLO is currently used at LNL in studies of fusion dynamics above and below the Coulomb barrier through the direct detection of ER events produced with stable beams. This set-up has been designed to allow a fast and reliable measurement of relative and absolute fusion cross sections. The apparatus consists of a reaction chamber, an electrostatic deflector and an energy, energy loss and time of flight telescope based on micro-channel plates, an ionization chamber and a silicon surface barrier detector. A picture of the experimental set-up is shown in Fig. 4.1.

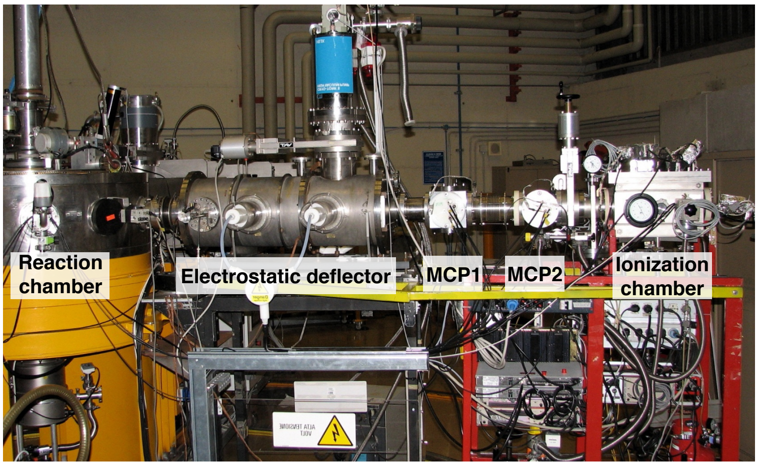

FIGURE 4.1: Picture of the experimental set-up PISOLO.

### 4.1.1 The reaction chamber

The reaction chamber is made of stainless steel and has a cylindrical structure with an internal radius of 50 cm. One of its main properties is to allow a rotation keeping the vacum inside ($10^{-6}$ mbar) by means of a sliding seal, so to perform angular distribution measurements.

Targets are fixed in a six-position holder, shown in Fig. 4.2. One of the positions is normally used for a quartz plate with a small central hole (1.5 mm in diameter), used to focus the beam. The target support is attached to the upper cover of the reaction chamber, and is moved through an external control system, so to be able to focus the beam at each change of energy and to change the target or its angle with respect to the beam direction.

Four 50 mm$^2$ silicon detectors are placed at a variable distance from the target. That distance is normally 195 mm, corresponding, when they are mounted on a circular support, to a detection angle of $\theta_{lab} = 16.05°$ with respect to the beam line (Fig. 4.2). These detectors are essential for the precision measurements necessary to normalize the fusion yields to the Rutherford scattering cross section and to monitor

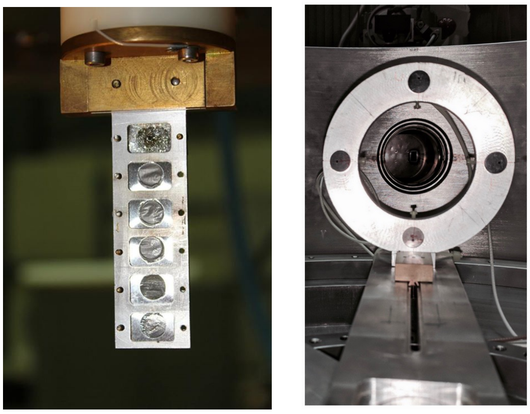

FIGURE 4.2: The target holder (left) and the four monitors (right).

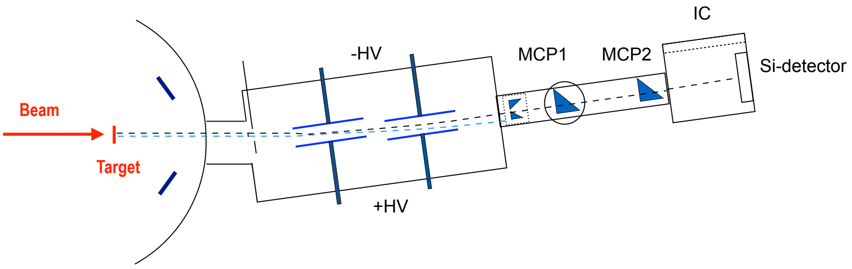

FIGURE 4.3: Horizontal view of the set-up. From the left: reaction chamber, electrostatic deflector and TOF-ΔE-E telescope.

the changes in beam position on the target, usually associated with the effects of the magnets installed on the beam line upstream of the reaction chamber. The monitor detectors have collimators with a diameter of 1.5 mm to reduce the counting rate and consequently the radiation damage. Taking into account that the surface of the detectors is not perpendicular to the line connecting each of them to the target, the total calculated solid angle is $\Delta\Omega_{mon}$ =(166.7±1.7) $\mu$sr for the four monitors.

### 4.1.2 Electrostatic deflector

The maximum of the ER differential cross section is found in a narrow peak centered at 0°, with a FWHM of few degrees. The electrostatic deflector allows their separation from the residual beam (see Fig. 4.3).

The deflector exploits the difference in electrical rigidity between the ER and the particles of the transmitted beam. This rigidity is defined as $\eta = E/q$, where $E$ is energy and $q$ is the ion charge state. The deflector is placed at an angle of 4.7° with respect to the beam direction. For deflection angles of this order, the trajectory of charged particles in the electrostatic field region can be approximated to an arc of circumference, which radius of curvature is given by the relation between centrifugal force and Lorentz force:

$$\frac{mv^2}{r} \sim q\epsilon \tag{4.2}$$

where $v$ and $m$ are the velocity and mass of the ion respectively, while $\epsilon$ is transverse electric field. Given that for the momentum conservation law the momentum of ER and beam particles are approximately equal, the ratio between the radii of curvature of the residues ($r_{ER}$) and of the beam particles ($r_b$) is proportional to the respective electrical rigidities.

$$\frac{r_{ER}}{r_b} \sim \frac{(E/q)_{ER}}{(E/q)_b} \sim \frac{(mq)_b}{(mq)_{ER}} \tag{4.3}$$

Since mass and charge state of the residues are usually greater than those of the beam ions, the evaporation residues have more pronounced curvature. The different trajectories allow a clear separation between the two types of particles, also for measurements performed at 0°.

The electrostatic deflector is contained in a stainless steel cylinder 30 cm in diameter and 85 cm in length. Inside the cylinder two pairs of stainless steel rectangular electrodes with smooth surface are placed (see Fig. 4.4 left panel). Each electrode has dimensions of 25 cm x 12 cm and a thickness of 0.5 cm. The distance between the plates is adjustable externally and separately for each electrode. Two different

FIGURE 4.4: The internal part of the electrostatic deflector with the two pairs of electrodes (left) and a picture of the MCP in use (right).

and independent field regions are generated, which allow a good adjustment for the different experimental conditions by minimizing the scattering of the beam on the plates. Two high voltage power supplies bring the electrodes up to a maximum voltage of around 40 kV and a collimator placed between the reaction chamber and the electrostatic deflector (entrance collimator) defines the acceptance angle of the deflector.

The applied voltage together with the geometry of the deflector plates bend slightly the primary beam that is stopped on a side of a collimator (exit collimator) placed at the end of the deflector. The ER, having lower electric rigidity, pass through the collimator and reach the detection system.

The applied voltage is chosen to ensure the maximum transmission of residues, but not all the primary beam is stopped. In typical fusion systems the rejection factor, defined as the ratio between the number of incoming and outgoing beam particles from the deflector, is $\sim 10^{7-8}$, according to the beam energy. Indeed, following the scattering in the target and the multiple collisions with the electrodes or the edges of the collimators, a fraction of the beam particles, degraded in energy, enters the exit collimator. A further separation of the two types of ions is therefore necessary, which is realized by the detector telescope downstream of the exit collimator.

### 4.1.3 Telescope Time of flight - Energy

The telescope discriminates the particles by exploiting the longer time of flight of more massive particles with respect to lighter particles of the same kinetic energy. Since the ER have a non-relativistic speed ($\beta \sim 0.03$ for the measured system $^{36}\mathrm{S} + {}^{51}\mathrm{V}$), their mass is related to the kinetic energy by the following relation:

$$M = \frac{2\,E\,TOF^2}{d^2} \tag{4.4}$$

The ER have a longer time of flight TOF through the telescope with respect to the lighter ions of the trasmitted beam. This allows to distinguish the two types of particles by measuring their TOF and their energy E. The mass resolution is obtained as follows, if energy and time are treated as independent variables:

$$\left(\frac{\Delta M}{M}\right)^2 = \left(\frac{\Delta E}{E}\right)^2 + 4\left(\frac{\Delta TOF}{TOF}\right)^2 \tag{4.5}$$

The relative error on the time $TOF$ can be reduced by increasing the flight length at the expense of the solid angle.

The telescope consists of two micro-channel plates detectors (MCP), a ionization chamber (IC) and a heavy-ion partially depleted silicon surface barrier detector inside the IC.

The two MCPs yield the TOF together with the silicon detector and the two flight bases are 666 mm and 1047 mm. The time resolution of the MCP detectors is comparable to that of the Silicon detector, and overall they sum up to around 300 ps. This contribution ($\Delta TOF/TOF \sim 0.7\%$) is therefore comparable to the energy resolution of $\Delta E/E \sim 1\%$. The mass resolution is therefore around $\Delta M/M \sim 1/58$ in typical cases.

Before reaching the silicon detector, the particles pass through an ionization chamber which provides their differential energy loss. In this configuration the silicon detector measures the residual energy and provides both the trigger for data acquisition and the start signal for the time of flights, as will be described below.

The telescope and the deflector are mounted on a platform which can be rotated in order to perform angular distribution measurements. When the detection system is placed at 0° the deflector is tilted by 4.7° with respect to the beam line whereas the telescope is shifted by 47 mm with respect to the symmetry axis of the deflector. This is the typical configuration employed in fusion reaction studies. A horizontal section of the set-up is shown in Fig. 4.3.

### Micro Channel Plates detectors

The use of MCP detectors is required by the need of detecting low-energy heavy ions without significantly altering their energy [57].

They are based on 43 x 63 $\text{mm}^2$ glass plates appropriately built to act as very compact electron multipliers with high gain (around $10^3$), see Fig. 4.5 (right). In the installed MCP detectors two glass plates are mounted in chevron configuration to get as output a fast time signal, large enough for further processing. With two plates, an

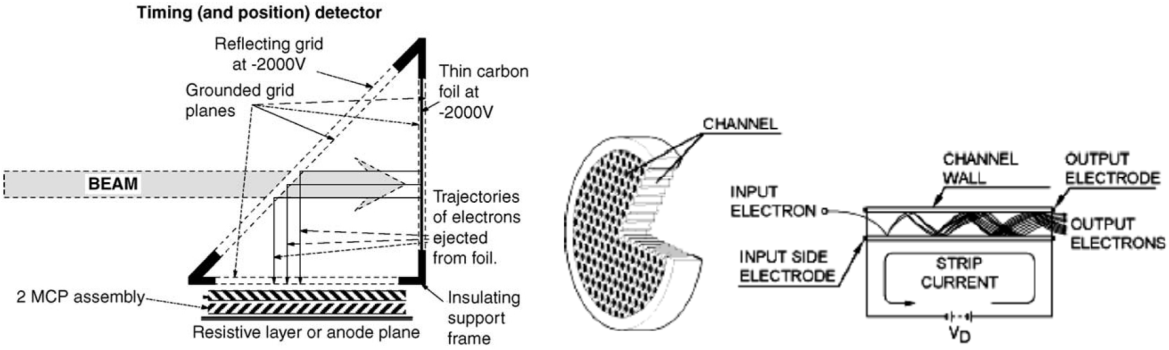

FIGURE 4.5: Scheme of a MCP detector with electrostatic mirror [56] (on the left) and of a MCP plate (on the right).

overall gain of the order of $10^6$ is achieved. They operate in high vacum conditions ($10^{-5}-10^{-6}$ mbar ).

The ions do not collide directly on the plates: they pass through a thin carbon foil of about 20 $\mu$g/cm$^2$ placed perpendicularly to their direction. Following the ion interaction with carbon, delta-electrons are emitted and successively accelerated and bent onto the plates by a 45° electrostatic mirror placed, where a voltage of about 1 kV is applied. A MCP detector of this kind is shown in the scheme of Fig. 4.5 (left).

The burst of produced electrons is collected on a metallic anode. They generate negative output signals with amplitudes of 10-100 mV or more, depending on the ions and on their energy, and a rise time of few nanoseconds. The geometry of the detectors guarantees the isochronism of the signals generated by the electrons, regardless of the crossing point in the carbon foil. Each MCP detector has a transparency of 85%, due to the presence of several grids, whereas their measured instrinsic efficiency is close to 100% for heavy ions.

The last detector of the telescope is an ionization chamber containing a silicon detector.

### 4.1.4 Electronic chain

The scheme of the electronics used for processing the signals from the monitors, MCP, IC and Si detector is shown in Fig. 4.6.

Most of the electronic chain is built up using standard NIM modules, due to the limited number of the parameters to be acquired and to the superior versatility of such kind of modules.

The signals from the four monitors are fed to the preamplifier (CANBERRA 2003BT) which gives as outputs time and energy signals. The energy signals are connected to the inputs of two ORTEC 855 dual fast shaping amplifiers. Despite using the lowest possible gain, the typical amplitude of the signals often exceeds the range of the peak-sensitive Analog-to-Digital Converter (ADC), thus an appropriate attenuator (Quad Rotary Attenuator) is employed. Finally, the signal is stretched by an ORTEC 542 module, before it is processed by the ADC. The time signals follow a different way. First they are amplified with a fast amplifier (ORTEC 9309-4) and subsequently sent to a Constant Fraction Discriminator (CFD) model PHILLIPS 715. The output signals of the CFD are sent to a gate generator (ORTEC GG8010) and then to a logical unit, where the four monitor signals are put in OR with the time signal of the silicon detector placed in the IC.

Each MCP provides a time signal. This signal is passed through a time pick-off pre-amplifier (PHILLIPS 6955) and fed into the CFD (PHILLIPS 715). The output signals of the CFDs are delayed and used as stop and/or start of the TAC module ORTEC-566. Three TAC modules are currently in use providing three time of flight signals (TOF). Each TAC is started by the signal of the detector with lower rate, in order to prevent that the TAC receives signals not followed by a stop. Therefore, the signals of the MCP, conveniently delayed, provide the stop for the two TACs, measuring the time of flight between the first (second) MCP and the silicon detector, referred to as $TOF_1$ ($TOF_3$). Another TAC is employed to measure the time of flight between the two MCP ($TOF_2$).

The electronic chain of the silicon detector is similar to the ones of monitors. Following the pre-amplification, the energy signal is further amplified (CANBERRA 2024), sent to the linear gate and stretcher (ORTEC 542) and subsequently to the ADC. The time signal feeds a fast amplifier and subsequently a CFD. Two output signals of CFD are used as start of $TOF_1$ and $TOF_3$, while a third one is sent to the gate generator (ORTEC GG8010). The output of this gate generator is sent in logical OR with monitors and the output of the logic unit provides the trigger which enables the data acquisition. The full dynamic range of the ADC (i.e. 4096 channels) is used.

The ionization chamber with transverse field, used before that the new detector was installed, provides an energy signal which passes through a pre-amplifier (ORTEC 2006E) and then is further amplified by a CANBERRA 2020 shaping amplifier. The output feeds the linear gate and stretcher to be finally processed by the ADC.

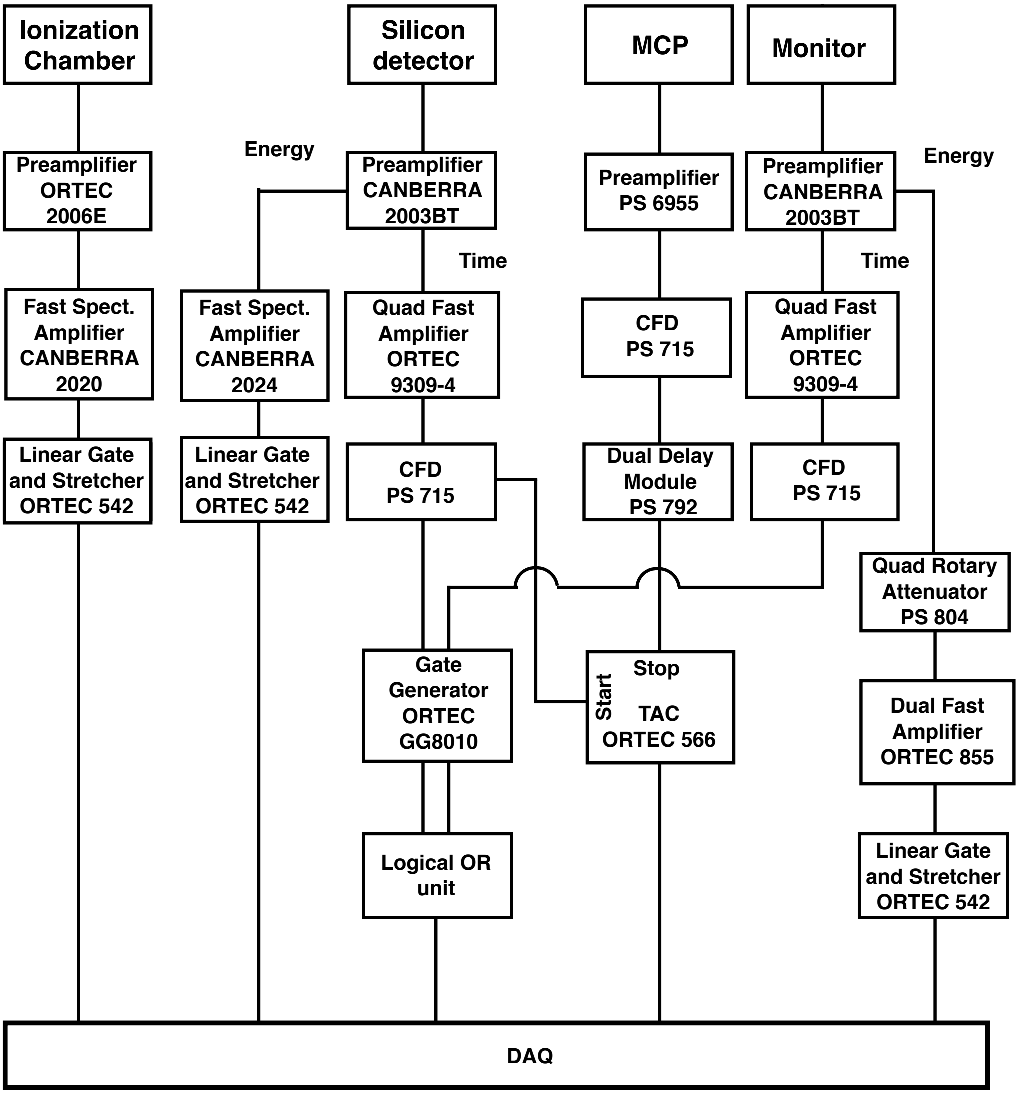

FIGURE 4.6: Electronic chain of the ionization chamber, the silicon detector, the MCPs (shown on an exemple of one) and the monitors (shown on an exemple of one).

## 4.2 The ionization chamber

Ionization chambers are simple gas-filled detectors. Their operation is based on the collection of all charges created by the direct ionization within the gas through the application of an electric field. The electric field which separates the positive and negative charge-carriers (*ion pairs*) can be either parallel (longitudinal IC) or perpendicular (transverse IC) to the particle's trajectory.

The total number of ion pairs created along the radiation track serves as the basic costituent of the electrical signal developed by the IC and depends linearly on the energy the particle has lost in the gas volume of the chamber. This linear response of the IC indicates that a fixed mean energy (defined as the W-*value*) is required in order to create one ion pair. This energy amounts to about 30 eV. The independence of $W$ on the particle's energy (at least above few hundreds keV) comes about because the competition between ionization and excitation process is rather independent on the energy and the amount of energy being transfered into kinetic energy of gas atoms is negligible.

The ion pairs take part in the random thermal motion and therefore have the tendency to diffuse away from regions of high density, with a more pronounced diffusion for free electrons because of their greater thermal velocity.

Among the many type of collisions that take place between free electrons, ions and neutral gas molecules, the most important in the understanding of gas-filled detectors behavior are: the charge transfer collisions, electron attachment and the recombination (Fig. 4.7). In particular, the last process occurs when the electron is captured by the positive ion, returning into a charge neutrality state, or the positive ion collide with a negative ion and both are neutralized through the transmission of the extra electron to the positive ion. In both cases of recombination the charge of the original ion pair is lost and consequently can not contribute to the signal. In order

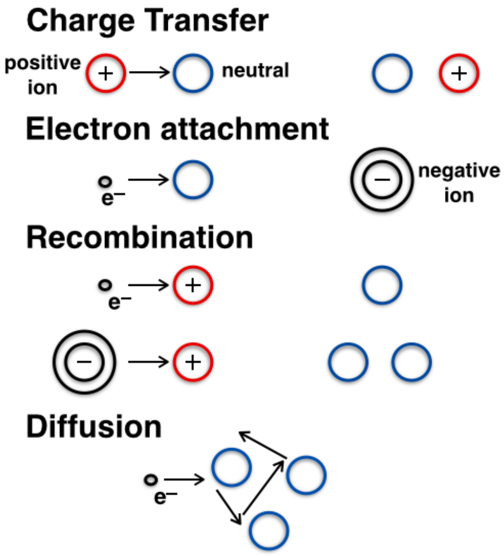

FIGURE 4.7: Different types of interactions of charge species in a gas. The interacting species are on the left whereas the products of such interaction are on the right. These are the main interactions that can influence the performances of gas-filled detectors.

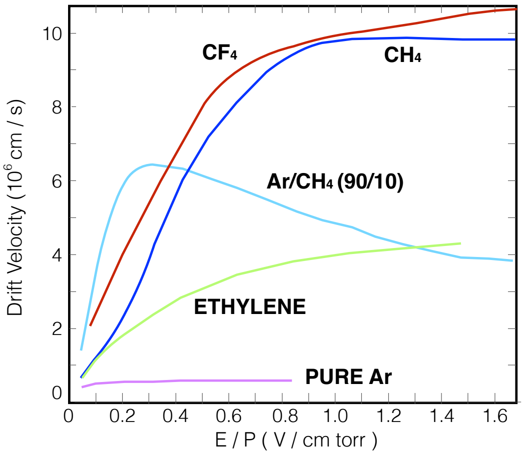

FIGURE 4.8: Electron drift velocity as a function of reduced electric field for different gases [59].

to minimize the recombination process, the charge separation and collection should be as fast as possible, and the employment of high electric fields are recommended for this purpose.

When an external field is applied, the ions and electrons have a net motion as result of the superposition of the random thermal velocity with a drift velocity in the given field direction. This drift velocity is proportional to the ratio of the electric field and pressure (defined as *reduced field*) through the mobility $\mu$. The mobility is nearly costant over a wide range of electric fields and for different gas pressures, and for free electrons is usually 1000 times greater than for positive ions because of their smaller mass. The typical collection time of electrons is then of the order of microseconds, whereas for the ions it is of milliseconds. For this reason the IC are usually operated in an electron sensitive mode, where the pulse amplitude of the signal reflects only the electron drift and is characterized by faster rise and fall times. Under these conditions the IC can therefore reach higher rates and shorter shaping times of the amplifiers can be adopted.
Operating in the electron sensitive mode however has the disadvantage that the pulse signal amplitude is sensitive to the position of the original radiation interaction, not reflecting only the total number of ion pairs formed [58]. Frisch gridded chambers allows to overcome this disadvantage [58].

The drift velocity depends also on the type of gas employed as shown in Fig. 4.8, where the drift velocity is reported as a function of the reduced field for various gases of common use. A saturation effect is observed in some gases as hydrocarbon and some mixtures, whereas for other gases the drift velocity increases until a maximum, and then decreases at higher applied electric field. In many other gases the electron drift velocity continues to increase with increasing electric field.

The ionization chamber basically allows to determine two important parameters of the charged particles: the total energy, when the particle is stopped in the chamber, and the nuclear charge Z, by measuring the differential energy loss in the gas, plotted vs. the total energy. Very often IC, especially small size ones, are used as energy loss detectors, whereas the total energy is measured by silicon detectors mounted directly in the chamber. Additionally, ionization chambers can be made position-sensitive by various methods [60]. This is of special importance for large-size detectors.

One advantage of ionization chambers with respect to solid state detectors, is the possibility to be built with large size. In this way, a broad range of the angular distribution of the emitted particles can be measured with one set-up and the large solide angle saves beam time. Another advantage is that, at variance with solid state detectors, ionization chambers are featured by negligible radiation damage for commonly used gasses as methane, iso-butane of tetrafluor-methane (freon). Furthermore, the dynamic range (i.e. the range of Z-values and energies which can be measured simultaneously) is much broader than for a solid state detector telescopes and the effective thickness of the detector can be easily adjusted to experimental requirements by changing the gas pressure [60].

### 4.2.1 The ionization chamber in the PISOLO set-up

A conventional ionization chamber using a Frisch grid [58] has been used for several fusion reaction measurements with stable beams at PISOLO (see Fig. 4.9).
The two parallel electrodes generate an electric field perpendicular to the beam line. The advantage of this transverse field ionization chamber is a fast separation of the formed ion pairs from the beam line. In addition, the Frisch grid removes the dependence of the anode pulse amplitude on the transverse position of the interaction. The cathode consists of one single plate of stainless steel, whereas the anode is segmented into three parts of 8 cm, 6 cm and 14 cm. This division of the anode allows to provide three differential energy loss signals which enable particle identification, however in normal working conditions the three signals are combined in a single one.

The pressure is chosen so that the ER lose about half of their energy in the gas, and is therefore typically few mbar and up to 20-30 mbar, for fusion reaction studies. The applied voltage is then chosen to maximize the electron drift velocity. The separation between the electrodes is 10 cm and the applied voltage in typical working conditions is of about 300 V, so that the tranverse electric field is of about 3000 V/m. The gas normally used is methane $CH_4$, which is kept flowing during the measurements in order to assure its purity, despite the interactions with crossing ions and the impurities that may be produced by the walls and various components of the circuit. The gas flow also reduces the recombination and assures a good energy resolution.

The beam ions and the evaporation residues enter in the chamber through one thin Mylar window of 200 $\mu$g/cm$^2$, pass through the gas and then they stop in a 600 mm$^2$ silicon detector (100 $\mu$m thickness), which provides a signal proportional to their residual energy. The transparency of the window is of 80%.

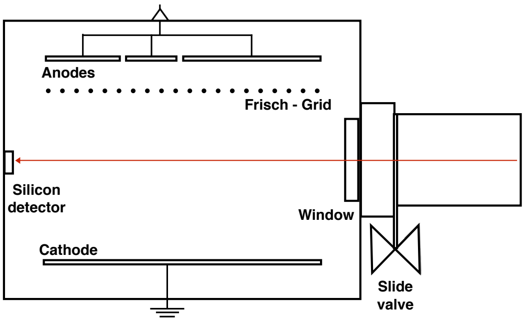

FIGURE 4.9: Scheme of the transverse field IC with Frisch grid of the PISOLO set-up.

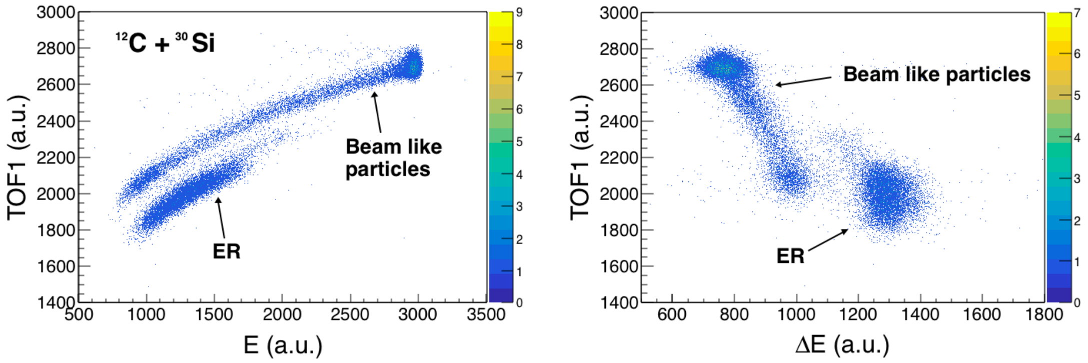

FIGURE 4.10: Time of flight $TOF_1$ vs. residual energy (left) and vs. the energy loss (right), measured for ${}^{12}$C+${}^{30}$Si in inverse kinematics [61]. The energy of the ${}^{30}$Si beam was 51 MeV, which is above the Coulomb barrier, therefore the ER energy was 33.6 MeV.

In Fig. 4.10 the time of flight is shown as a function of the energy loss provided by the IC (right) and the residual energy of the silicon detector (left). The ER are well identified and separated from the degraded beam even in this case where the reaction was studied in inverse kinematics [61].

The counting rate of this IC is limited to a few $10^3$ particles per second (pps). This limit originates from the distance between the two electrodes because the electrons generated along the particle trajectory must travel relatively long distances to reach the anode planes.

## 4.3 The Fast IC

### 4.3.1 Upgrading the PISOLO set-up

As mentioned in Chapter 3, the detection of evaporation residues (ER) is a difficult task when radioactive ion beams are employed in fusion studies. This detection becomes more challenging at very forward angles and in inverse kinematics. In addition, radioactive beams are usually highly contaminated by other elements with similar masses and energies.

Under these experimental conditions, detection systems should provide an efficiency close to 100%. Therefore, it is very important to design detectors minimizing energy straggling and angular dispersion and providing a fast response time. Gas−filled ionization chambers are well suited for these applications, since they have a moderately good energy resolution and can withstand prolonged exposure to high beam intensities without damage, in contrast to fragile semiconductor detectors.

The present PISOLO set-up has been largely employed in fusion reaction studies near and below the Coulomb barrier, with several interesting results [61, 62, 63]. The use of unstable beams allows to extend this investigation to regions far from stability where nuclear structure changes substantially. However, the experimental set-up described above is not suitable for such studies because of its low absolute efficiency, typically less than 1% for the detection of evaporation residues.

This low efficiency is due to *i*) the geometrical structure of the apparatus whose effective solid angle is very small because of the length of electrostatic deflector and

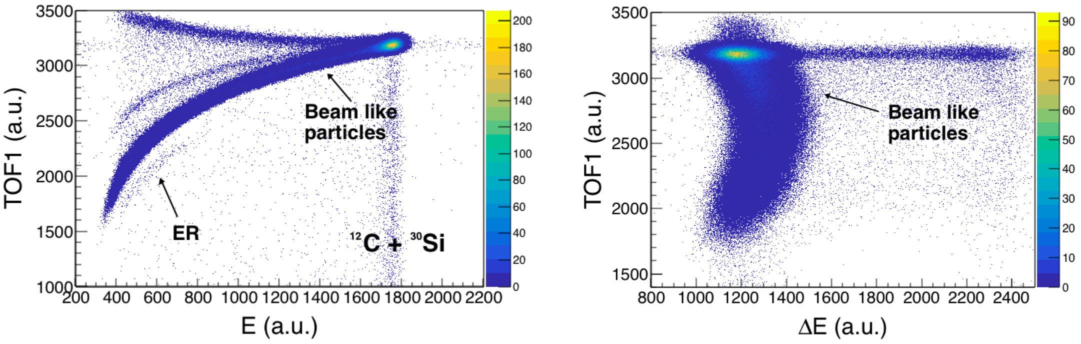

FIGURE 4.11: Time of flight TOF$_1$ as a function of the energy loss provided by the ionization chamber (right) and of the residual energy measured by the silicon detector (left). The reaction is $^{12}$C+$^{30}$Si studied in inverse kinematics. At variance with Fig. 4.10, the energy of this measurement is 39 MeV, i.e. below the Coulomb barrier. The ER are not easily identified through the energy signals provided from the IC, because of the high background, which increases at low energies because of the longer time of measurement.

the subsequent telescope, and *ii*) to the low counting rate tolerated by the ionization chamber. One way to increase the efficiency is to place the apparatus in the direction of the beam and as close as possible to the target, without any electrostatic beam separation. This requires using very fast detectors. While MCP detectors have a very fast response, and can withstand rates up to hundreds of kHz, the conventional IC used in PISOLO can only work up to a few kHz, and therefore would anyway limit the performance of the whole set-up.

The low counting rate of the transverse field ionization chamber depends on the large distance between the two electrodes. The anode pulses have various time delays which depend on the distance of the particle tracks from the Frisch grid. The spread of these delays hampers high-rate operation of gridded ionization chambers. In particular, this limit becomes clear in one of the last measurements where a sub-barrier fusion study of the system $^{12}$C+$^{30}$Si in inverse kinematics was performed [61]. Figure 4.11 shows the plots of TOF$_1$ vs. the residual energy provided by the silicon detector (left panel) and vs. the energy loss $\Delta$E provided by the IC (right panel). The beam energy was 39 MeV, which is of about 10% below the barrier. At such energies the ER are not identified in the plot TOF$_1$ vs. $\Delta$E because of the high background due to random coincidences. This example shows that the IC is not suitable for ER identification at very low energies.

A set-up with high efficiency was built at Oak Ridge National Laboratory (ORNL) for the study of fusion reactions with exotic beams [56], shown schematically in Fig. 4.12. With a typical beam intensity of 20000 ion/s and a target thickness of 1 mg/cm$^2$, the lowest measured ER cross section reached by this set-up was 1 mb[64]. Following the good performance of the ORNL equipment, a new set-up based on the use of fast ionization chamber has been developed and will be installed at LNL, with the aim of significantly improving the performance of the ORNL equipment, both from the point of view of the solid angle and allowing measuring at high counting rates. The scheme of the new set-up is shown in Fig. 4.13. It has been specifically designed for the use with relatively low-intensity beams ($10^5$ ion/s) and should allow, thanks to the high counting rate capability of the new ionization chamber, to

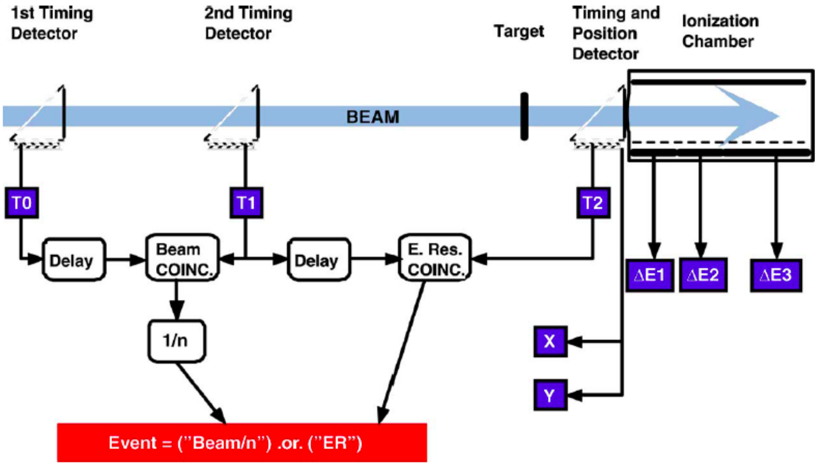

FIGURE 4.12: The ORNL set-up for measurements of fusion with exotic beams [56].

measure the fusion excitation function down to around 100 $\mu$b.

In the new configuration, the detection system will be placed at 0° with respect to the beam in the following sequence (see Fig. 4.13): two MCP position-sensitive detectors upstream of the target and a third position-sensitive MCP and a fast ionization chamber, placed very close to the third MCP, downstream of the target to identify ER events. The first two MCPs will provide the event trigger and will be used to monitor the beam quality and direction, to get rid of unwanted beam-like components, to normalize the cross sections and to yield a timing reference. Exploiting the lower velocity of the ER with respect to the beam, the events with a longer time of flight between the 2nd and 3rd MCPs will be selected. The third MCP will also allow to examine the beam profile, verifying that the beam is well centered, and possibly measure the ER angular distribution. The distance of this third MCP from the target will be chosen according to the contrasting needs of simultaneously maximizing the efficiency for detecting ER and the time of flight difference between

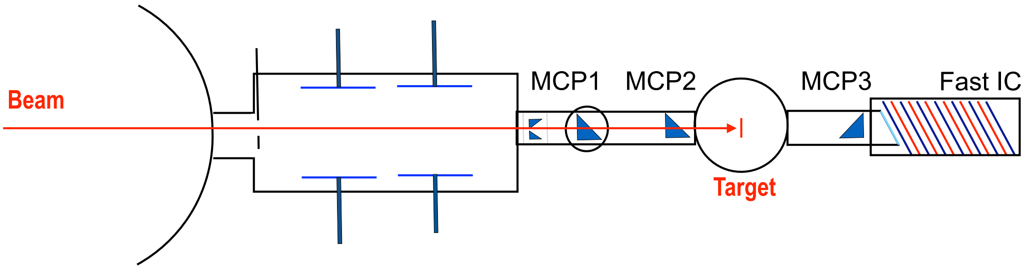

FIGURE 4.13: Scheme of the upgraded PISOLO set-up for the low intensity beams of SPES. From the left: the electrostatic deflector in transmission (no field applied), the first and second MCP, the reaction chamber, the third MCP and the fast IC.

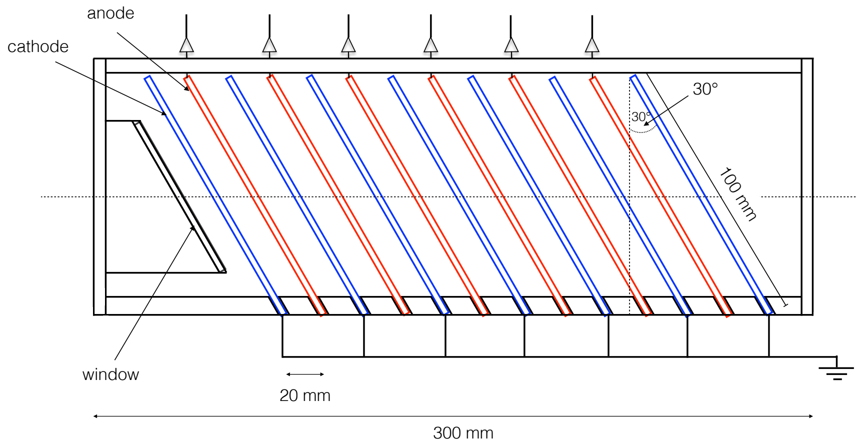

FIGURE 4.14: Scheme of the fast ionization chamber at LNL. Some dimensions are given.

beam and ER events. The energy-loss and the total energy signals from the IC will discriminate the ER according to their atomic numbers.
When the high intensity beams ($10^7$-$10^8$ pps) of SPES will be available, their physical separation from the reaction products will be necessary. Under these conditions, a configuration similar to the one currently in use for fusion studies induced by stable beams will be adopted, by placing the target in the sliding seal reaction chamber (see Fig. 4.3). The existing electrostatic beam deflector will be therefore used and placed between the target and the detection system made up of the three MCPs and the IC. As an alternative, a reduction in the random background count rate can be achieved by introducing a small, precisely placed, beam stop made of heavy material in front of the third MCP detector. This configuration would result in a lower efficiency for ER detection, but lead to a significant reduction in the random coincidence rates.

In order to allow higher counting rates in the IC of the upgraded set-up, a fast ionization chamber (Fast IC) has been developed at LNL.
This new IC is based on an existing detector described by Kimura et al. [65]. They introduced a new design based on multiple tilted parallel electrodes made of thin conductive foils. This IC was employed for high-energy heavy ion detection at the RIKEN accelerator facility. The new design significantly improves the counting rate capability and is effective in the separation of different particle species. The Frisch grid is not necessary because the electrodes are approximately perpendicular to the trajectories of incoming particles. A similar design was adopted by Chae et al. [66] for a new fast-counting ionization chamber developed at Oak Ridge National Laboratory for low energy measurements. This second ionization chamber differs from the previous one because the electrode planes are replaced by grids in order to avoid the energy losses that occur when charged particles pass through the foil electrodes used in Kimura design. Another improvement of this last ionization chamber is a tilted entrance window. This implementation is very important for the detection of low-energy particles, because in this way the passive thickness is reduced before the first anode.

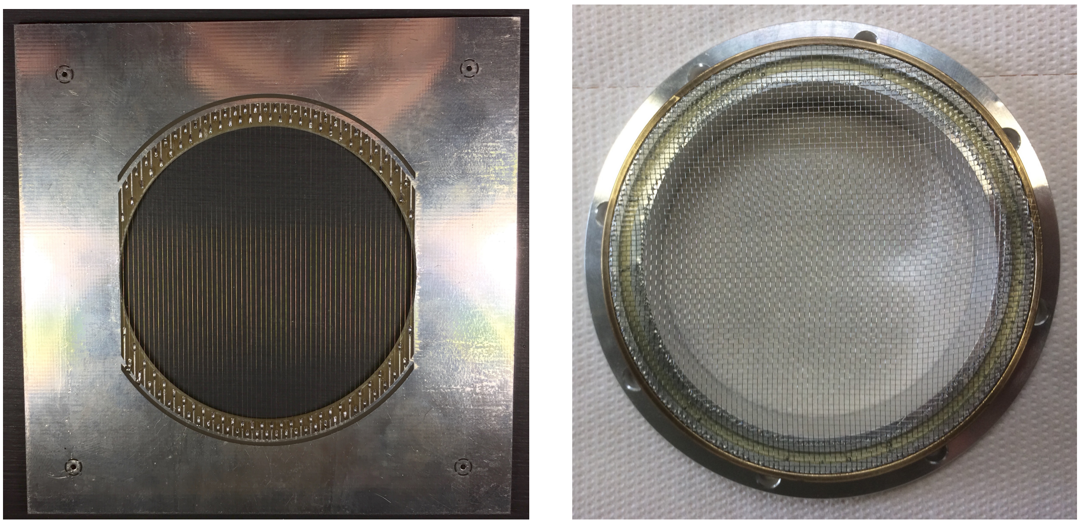

FIGURE 4.15: A gridded electrode (left) and the entrance window (right).

### 4.3.2 The fast ionization chamber at LNL

A schematic view of the new fast ionization chamber developed at LNL is shown in Fig. 4.14. Its structure is very simple: six anodes and seven cathodes are alternately placed in 20 mm steps and tilted of 30° with respect to the perpendicular to the beam line. The electric field is not parallel to the beam axis, so that the electrons and positive ions produced in the gas drift away from each others, which allows to minimize the recombination. In addition, the alternating electrode arrangement results in short drift time for the electrons and positive ions to be captured by anode and cathode, respectively.

The 13 electrodes are inserted in a insulating Delrin support allowing an easy

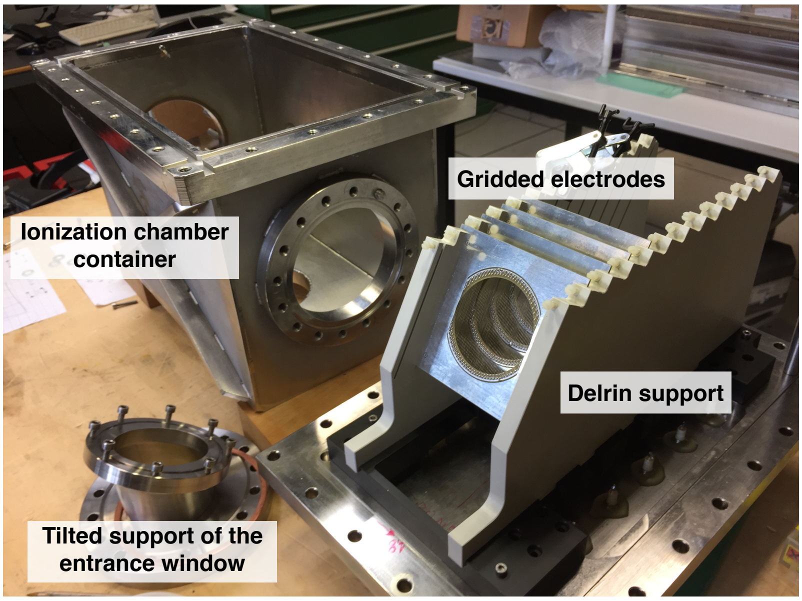

FIGURE 4.16: The various components of the IC.

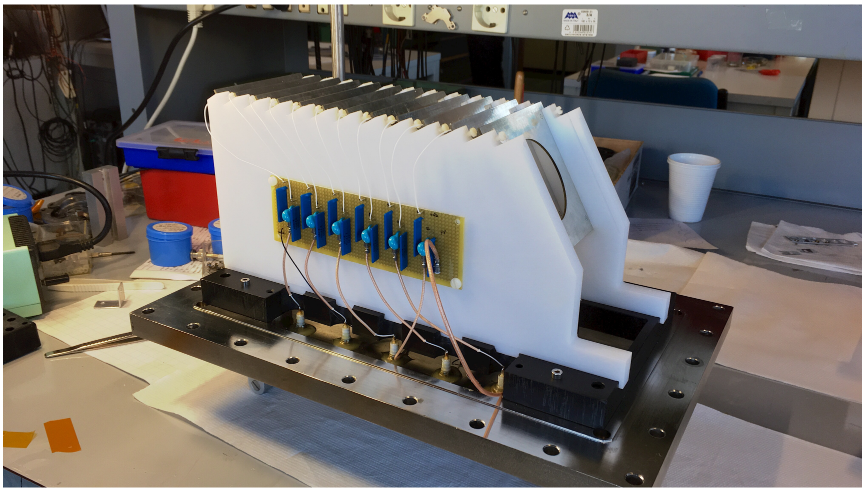

FIGURE 4.17: The fully assembled fast ionization chamber.

and fast replacement of electrodes if damaged. Each electrode has a 10 cm x 10 cm copper coated fiberglass frame. The frames have 6 cm diameter circular openings and 20 $\mu$m gold coated tungsten wires are soldered to them with 1 mm spacings. As shown in Fig. 4.15 (left), each wire is individually soldered to the copper frame so to allow replacing damaged wires without affecting nearby ones. The total depth of the IC is 30 cm.

Each anode is connected to a single BNC feedthrough whereas the cathodes are combined and grounded. In this configuration a signal of energy loss $\Delta E_i$ is provided by each section between two adjacent cathodes. These signals can be easily manipulated outside the chamber. They can be summed to give a total energy signal, otherwise different options can be configurated without opening the IC.

The entrance window is parallel to the electrodes (tilted by 30°) and is made of a thin Mylar $(C_{10}H_8O_4)_n$ film glued on a metallic mesh, having a thickness of

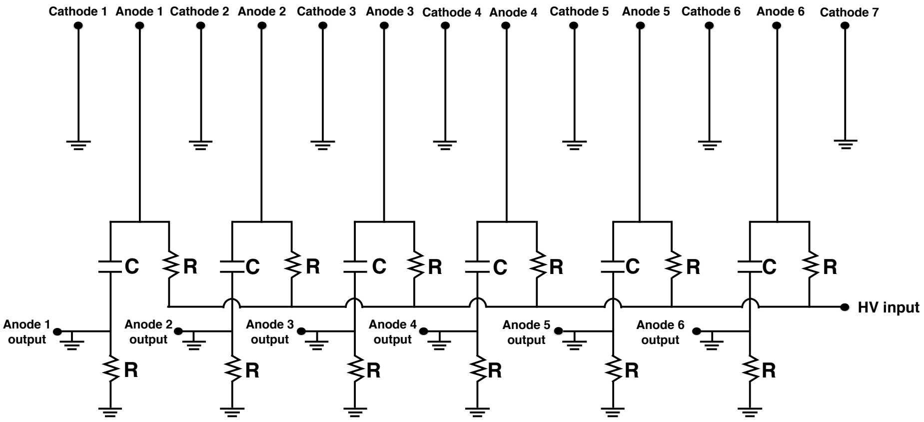

FIGURE 4.18: RC circuit of the fast ionization chamber. The cathodes are all grounded whereas the signals provided by the anodes are extracted. All the resistors, indicated as "R" are 100 Ω and the capacitors "C" are 10 $\mu$F.

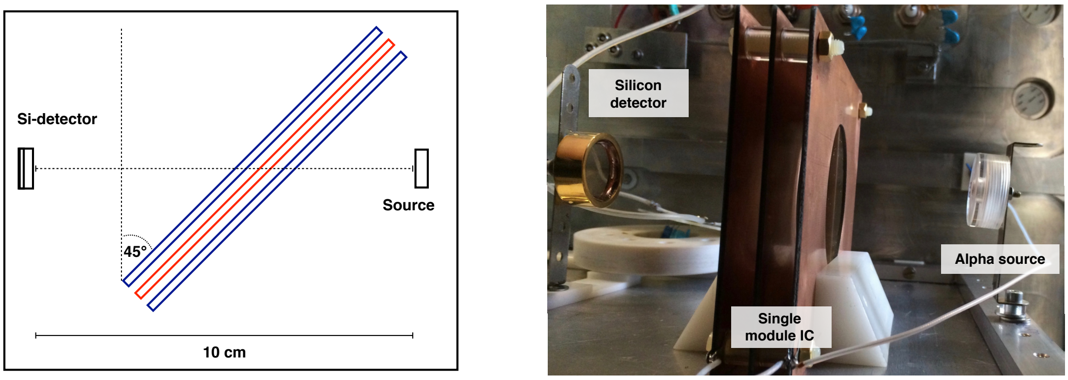

FIGURE 4.19: On the left the arrangement for the $\alpha$-test. On the right a picture of the set-up installed in the vacuum chamber.

$200\,\mu g/cm^2$ (Fig. 4.15 right panel). The film and the mesh are fixed on a metallic flange attached to the tilted support, as shown in Fig. 4.16. This configuration allows to easily replace the window, and to keep constant the distance between the window and the first cathode. This geometry is important for low-energy ion detection, to have a small dead space in the gas independent of entrance position.

As discussed in the previous section (Sec. 4.2), when an incident particle goes across the ionization chamber, a fast negative voltage pulse is obtained from the anodes due to the electron collection. Since the mobility of electrons is typically three orders of magnitude greater than that of positive ions, only the electron part of the anode pulse is sufficient to obtain the energy loss information, disregarding the part due to positive ions. The output pulses are proportional to the energy released by the ion in the various sections, and they are fed into charge-sensitive preamplifiers.

The layout of the circuit which allows to polarize the six anodes and to extract the energy signals is shown in Fig. 4.18. The circuit for the single anode output signal is the typical one used in pulse operational mode [58].
Each output from the anodes of the ionization chamber is preamplified and subsequently fed into pulse-shaping amplifiers. To optimize the performance of the ionization chamber, various types of preamplifiers and amplifiers have been tested, as described in the next chapter. The output of the shaping amplifier feeds the linear gate and stretcher to be finally processed by the ADC (as shown in Fig. 4.6).

### 4.3.3 First test with alpha source

A first test with an alpha source was performed on a prototype of the detector. This prototype was a single module of the IC made up of two cathodes and one anode placed in between.

The test was performed by placing the module between the source and a silicon detector ($50\,mm^2$), which was used to trigger the signal provided by the module. Figure 4.19 shows a picture (right) and a scheme (left) of the adopted set-up. The module was placed at 45° with respect to the axis between the $\alpha$-source and the silicon detector in order to simulate the tilted configuration of the IC. Both $\alpha$-source and detector were placed in a vacuum chamber first pumped down to vacuum and then filled with $CH_4$ gas at 200 mbar. In order to detect the $\alpha$ particles, the gas pressure was higher than the one normally adopted in working conditions and consequently the voltage applied to the module was 1 kV.

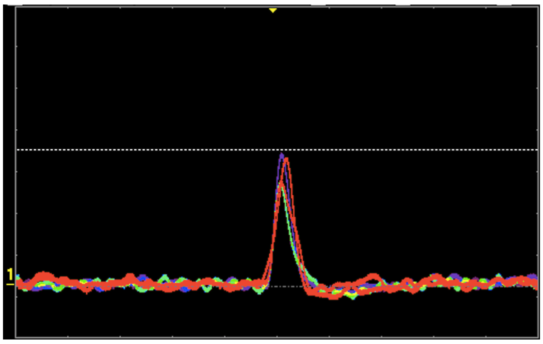

FIGURE 4.20: The output signal of the IC module obtained in the test with alpha particles (see text).

The cathodes were grounded whereas the signal of the anode was first processed with a RC circuit (as the one showed in Fig. 4.18) and passed through the pre-amplifier and the CANBERRA 2020 amplifier (with a shaping time of 2 $\mu$s).

The output of the shaping amplifier is shown in Fig. 4.20. The signals have an average amplitude of 160 mV and a noise of 10 mV. Following the good result obtained on the single module, several tests with intense stable beams have been performed and are described in the next chapter.

## Chapter 5

# Tests of Ionization Chamber with stable beams

## 5.1 Tests with stable beams

The performance of the fast ionization chamber has been tested in different fusion and transfer reactions with stable beams. At the Laboratori Nazionali di Legnaro heavy ion beams are delivered by the Tandem–ALPI–PIAVE accelerator complex [67, 68]. The Tandem XTU is a Van de Graaff accelerator and can be employed in stand–alone mode or as an injector for the linac booster ALPI. At present, the accelerator complex delivers ion beams of stable isotopes from proton to lead.
A total of four reactions have been performed in five different tests, each one-day long:

- $^{28}$Si+$^{100}$Mo: The Tandem accelerator provided a $^{28}$Si beam on a $^{100}$Mo target at the energy of 125 MeV. The target thickness was 150 $\mu g/cm^2$ on a 15 $\mu g/cm^2$ carbon backing. The averange current was 5 pnA;
- $^{58}$Ni+$^{28}$Si: A $^{58}$Ni beam was delivered by the Tandem accelerator on a $^{28}$Si target at the energy of 190 MeV. The target thickness was 50 $\mu g/cm^2$ on a 30 $\mu g/cm^2$ carbon backing. The average current was 4 pnA;
- $^{64}$Zn+$^{54}$Fe,$^{197}$Au: The PIAVE-ALPI accelerator provided a $^{64}$Zn beam at the energy of 275 MeV. The intensity of the beam was about 3 pnA. The $^{54}$Fe target was 40 $\mu g/cm^2$ thick on a 15 $\mu g/cm^2$ carbon backing. The $^{197}$Au target thickness was 200 $\mu g/cm^2$.

In all the measurements, the fast ionization chamber replaced the transverse field ionization chamber in the experimental set-up (see Chapter 4.2.1 and Fig. 4.14 for the details).

The new detector has been tested in different configurations by employing various electronic module parameters (shaping time, veto, trigger gate, . . . ) and physics conditions (gas type and pressure, detection angle, type of reaction).

For the various systems listed above, several tests were also carried out to verify the performance of the IC by adopting the MCP signal as the trigger of the data acquisition system (DAQ). In typical working conditions used in fusion studies, the residual energy of ER is measured by the silicon detector (covering the small solid angle of $d\Omega = 0.0358 \pm 0.0004$ msr), which provides the trigger for the DAQ (Chapter 4). This avoids overloading the DAQ with useless events missing the residual energy signal, but of course the absolute efficiency of the whole set-up is determined by the solid angle of the silicon detector. If ER are stopped within the IC, on the contrary, using the time signals of MCP1 (see Fig. 4.3) as trigger of DAQ, the effective solid angle increases to $(0.2359 \pm 0.0004)$ msr. This situation encourages the choice of using the MCP as DAQ trigger, also because the future heavy SPES beams would quickly damage the silicon detector, as described in Chapter 3, due to their relatively high intensity not filtered out by the electrostatic deflector as in the previous version of PISOLO.

Another key point is that the present DAQ of the PISOLO set-up can not handle a high rate (more than $\sim 18$ kHz), which will be reached because of the geometry and absence of the electrostatic deflector foreseen in the upgraded set-up for the SPES beams. The main limit is originated by the fact that when the data server is busy saving previous data, a veto signal is produced and fed into the DAQ system to prevent additional events from being processed. This causes a long dead time. Various tests have been anyway performed with very high counting rates in the IC, measured by a scaler, even if not all those events could be effectively handled by the DAQ system.

The following sections report on the most important results which were obtained.

### 5.1.1 Shaping time and the acquisition gate width

Initial tests were performed on the shaping time that has to be set on the amplifier because at very high counting rates, such as expected with SPES beams, pile-up effects and random coincidences may significantly deteriorate the quality of the acquired data.

Pile-up of signals may occur when two pulses from the same detector are very close in time to each other. This produces a single pulse with an amplitude equal to the sum of the two ones. This effect can be minimized by making the width of the pulses as small as possible and this condition is reached by adopting a shorter shaping time. This results in a faster return to the baseline and reduces the probability of having pile-up events at high counting rates.

Random coincidences, as the word suggests, are generated when two signals from different detectors, not related to the same physical event, are so close in time that they arrive within the same trigger gate. The rate of random coincidences ($R_{random}$) is given by:

$$R_{random} = R_1 * R_2 * \Delta T \tag{5.1}$$

where $R_1$ and $R_2$ are the counting rates of the two detectors and $\Delta T$ is the time width of the trigger gate (coincidence time). It is then clear that having fast signals from detectors allows to reduce $\Delta T$ and consequently the rate of random coincidences that produce background in two dimensional spectra. Additionally, the effect of noise has to be considered. By definition, noise is an undesired fluctuation that gets superimposed on a signal. A typical noise that affects ionization chambers is the microphonic one, which is due to vibrations transmitted to the detector-preamplifier and can generate small fluctuations in capacitance, that results in a modulation of the output signal. Using short shaping times minimizes this contribution to the total noise.

Shaping time tests have been performed employing the fusion reaction $^{28}$Si+$^{100}$Mo in direct kinematics. The applied voltage provided to the ionization chamber was 100 V and the gas was $CH_4$ at the pressure of 16 mbar. The pressure was chosen to ensure that the ER reached the silicon detector so that its time signal was employed for both the trigger of DAQ and the start of the two times of flight $TOF_1$ and $TOF_3$ (see Fig. 4.3). During these tests the signals provided by the anodes have been

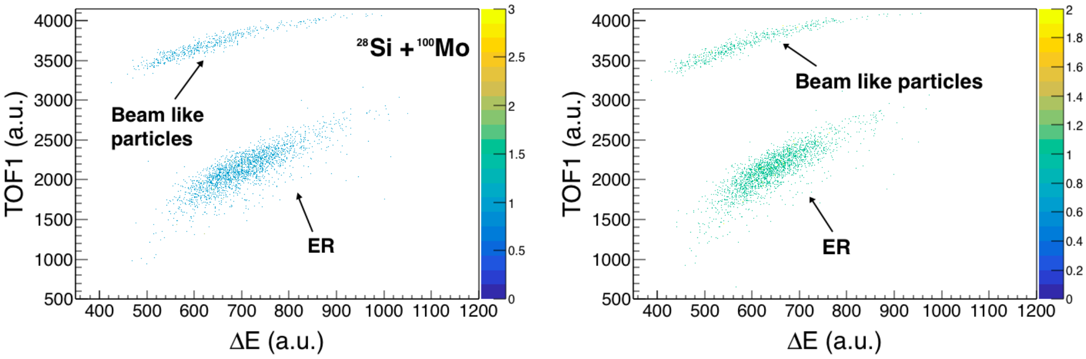

FIGURE 5.1: Time of flight $\mathrm{TOF}_1$ as a function of the total energy loss ΔE provided by the fast ionization chamber using a shaping time of 1 $\mu$s (left panel) and 0.25 $\mu$s (right panel).

summed to have a unique total energy loss ΔE signal. The amplifier and preamplifier used were Canberra2020 and ORTEC2006E, respectively. Two measurements have been carried out using shaping times of 1 $\mu$s and 0.25 $\mu$s for the CANBERRA2020. In Fig. 5.1 the time of flight $\mathrm{TOF}_1$ is plotted as a function of the energy loss for the two measurements.

The quality of the spectra, judged by the resolution and separation of the evaporation residues from the beam like particles is not affected by the use of the very short shaping time of 0.25 $\mu$s (Fig. 5.1, right panel). In order to estimate the improvement obtained using a smaller shaping time, the ratio of the random background events to the total number of events (which includes beam, evaporation residues and background), defined as $N_{noise}/N_{total}$, has been calculated for the two measurements. As shown in the Table 5.1, this ratio is smaller by 21% for the shaping time of 0.25 $\mu$s. Therefore a shaping time of 0.25 $\mu$s was used in all subsequent tests.

The availability of fast signals allows to reduce not only the shaping time but also the width of the gate of the data acquisition. The choice of the width is strictly related to the type of signals that have to be acquired. The slow response of the transverse field ionization chamber, with respect to the other detectors in use, imposed a gate width not shorter than 4 $\mu$s. It is expected that the response of the fast ionization chamber allows to overcome this limit and to reduce the width of the gate.

In order to check this, two measurements have been performed using fusion reactions both in direct and inverse kinematics. For the direct reaction $^{28}\mathrm{Si} + {}^{100}\mathrm{Mo}$ gate widths of 4 $\mu$s and 2 $\mu$s have been used. As in the case of the shaping time test, the applied voltage was 100 V and the pressure of $\mathrm{CH}_4$ gas was 16 mbar. In this test, the MCP placed closest to the ionization chamber (defined as $\mathrm{MCP}_1$ in Fig. 4.1) provided the trigger for the data acquisition. The anodes have been combined in two energy loss signals ($\Delta E_1 + \Delta E_2 + \Delta E_3$ and $\Delta E_4 + \Delta E_5$). The plots showing the time of flight $\mathrm{TOF}_2$ as a function of the two energy losses are reported in Fig. 5.2. The

TABLE 5.1: The $\mathrm{N}_{noise}/\mathrm{N}_{total}$ values for the measurements performed employing different shaping times.

| Reaction | Shaping time ($\mu$s) | $\mathrm{N}_{noise}/\mathrm{N}_{total}$ (%) |
|---|---|---|
| $^{28}$Si+$^{100}$Mo | 1.00 | 0.327 ±0.006 |
| | 0.25 | 0.258 ±0.005 |

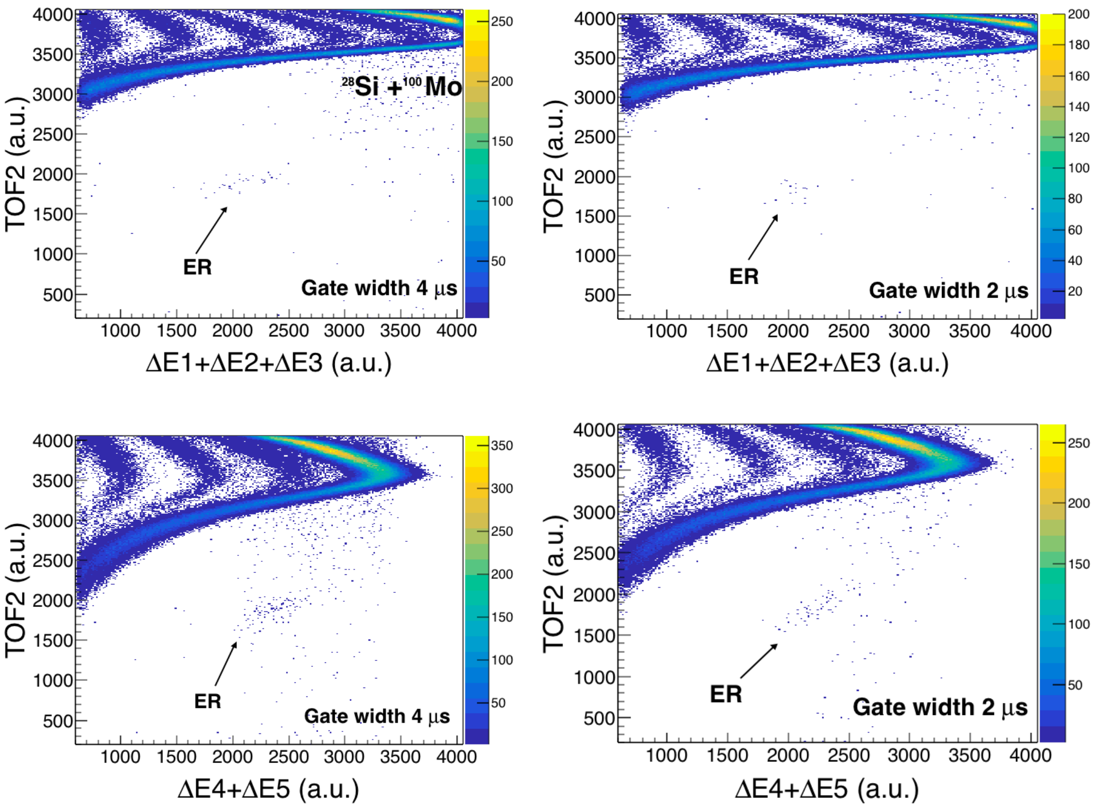

FIGURE 5.2: Time of flight $TOF_2$ as a function of the combined energy loss signals provided by the anodes $\Delta E_1$, $\Delta E_2$ and $\Delta E_3$ (upper panels) and $\Delta E_4$ and $\Delta E_5$ (bottom panels). The spectra obtained using a gate width of 4 $\mu$s and 2 $\mu$s are on the left and right panels, respectively.

measurements have been performed at a detection angle of 0.5° with a beam current of 10 pnA. Under these conditions, the counting rate of the ionization chamber was 13 kHz and the background was reduced in the case of 2 $\mu$s gate width, as shown

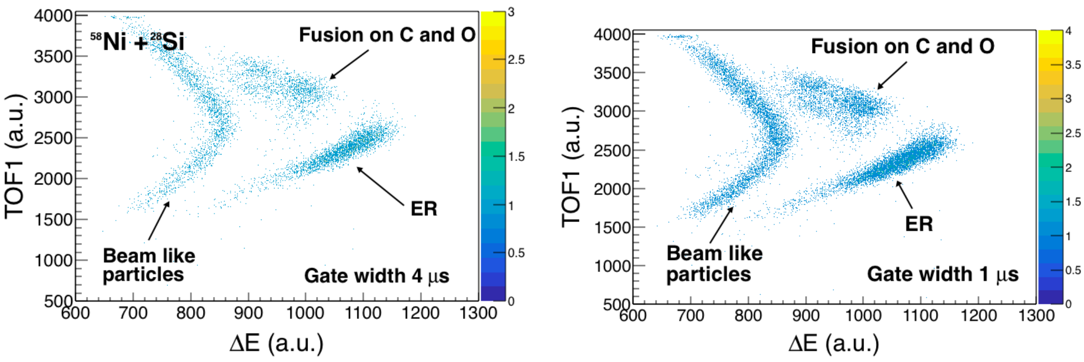

FIGURE 5.3: Time of flight $TOF_1$ as a function of the total energy loss ΔE provided by the fast ionization chamber using a gate width of 4 $\mu$s (left panel) and 1 $\mu$s (right panel).

in Fig. 5.2 (left panel) (the two measurements have been performed in comparable acquisition time). Also for this test, in order to estimate the improvement obtained using narrower acquisition gates, the ratio $N_{noise}/N_{total}$ has been calculated, and its values are reported in Table 5.2. The use of a 2 $\mu$s gate results in a reduction of the $N_{noise}/N_{total}$ of ∼16% (1.562/1.855) and ∼11% (0.764/0.858) for the combination of the first three and the last two anodes' signals, respectively.

In the case of the fusion reaction $^{58}$Ni+$^{28}$Si in inverse kinematics, the measurements were taken with gates of 4 $\mu$s and 1 $\mu$s. The silicon detector provided the trigger and start signals of the time of flights. The pressure of the gas ($CH_4$) was 30 mbar and the applied voltage 300 V. During these measurements the preamplifier Mesytec MS-L16 and the Fast Spectroscopy Amplifier Canberra 2024 have been employed, and the anodes' signals have been combined in a single energy loss signal. Also in this inverse kinematic reaction a good quality of ER separation from the residual beam particles is obtained by using a 1 $\mu$s gate width, as shown in Fig. 5.3 (right panel). The fusion on the carbon backing of the target and on the oxygen (originated from the target oxydation) is also well identified. The noise to total ratio for the measurements performed with 4 $\mu$s and 1 $\mu$s gate are shown in Table 5.2. The shortest width of 1 $\mu$s gives a reduction of 20% of the $N_{noise}/N_{total}$.

TABLE 5.2: The $N_{noise}/N_{total}$ values for the measurements performed employing different gate widths and different reactions.

| Reaction | Gate ($\mu$s) | $N_{noise}/N_{total}$ (%) |
|---|---|---|
| $^{28}$Si+$^{100}$Mo | | |
| $\Delta E_1+\Delta E_2+\Delta E_3$ | 4 | 1.855 ±0.004 |
| $\Delta E_4+\Delta E_5$ | 4 | 0.858 ±0.001 |
| $\Delta E_1+\Delta E_2+\Delta E_3$ | 2 | 1.562 ±0.004 |
| $\Delta E_4+\Delta E_5$ | 2 | 0.764 ±0.001 |
| $^{58}$Ni+$^{28}$Si | | |
| $\Sigma\Delta E$ | 4 | 1.09 ±0.04 |
| $\Sigma\Delta E$ | 1 | 0.88 ±0.03 |

### 5.1.2 Transparency of the electrodes

One of the important parameters for the use of this IC is the transparency of the electrodes, defined as the fraction of ions which pass through a given electrode.
Gridded electrodes avoid the additional energy loss which occurs when charged particles pass through the electrode planes (as in the case of the IC described in [65]). In the present case, a fraction of particles is stopped by the wire grids, resulting in a reduction of the transmitted beam and evaporation residues during fusion experiments. Knowing the transparency of each electrode is therefore necessary to evaluate the cross section. From simple geometrical considerations one can expect that the transparency of each grid is given by

$$Transparency = 1 - \frac{wire\ thickness}{wire\ spacing} = 0.98 \tag{5.2}$$

Nevertheless, this has been checked using both fusion and scattering reactions. In order to identify and count the particles stopped by the wires, the $MCP_1$ detector was used to provide the trigger for the data acquisition, since the particles which reach the silicon detector pass anyway through all electrodes.

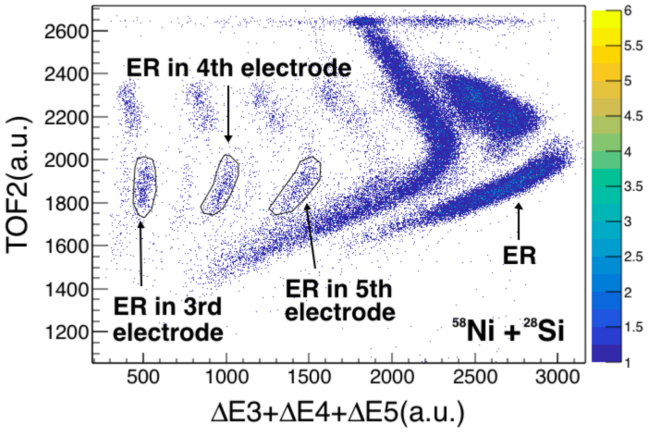

FIGURE 5.4: Time of flight between the two MCPs (TOF$_2$) as a function of the sum of energy loss of signals provided by three anodes. The ER stopped in the electrodes' grids are well identified.

The study of transparency in fusion reactions has been performed for the case of $^{58}$Ni+$^{28}$Si reaction in inverse kinematics, where the experimental conditions have been reported in Sec. 5.1. Fig. 5.4 shows TOF$_2$ as a function of the energy loss obtained by combining three anodes $\Delta E_3 + \Delta E_4 + \Delta E_5$. On the left of ER, groups of particles stopped in the three anodes wires are well visible. All of them have the same TOF$_2$ but different energy losses. In Fig. 5.5 (left panel) the energy loss signal $\Delta E_3 + \Delta E_4 + \Delta E_5$ is plotted as a function of $\Delta E_1 + \Delta E_2$. By selecting the ER observed in Fig. 5.4 including also the stopped ones, we obtain the spectrum shown in Fig. 5.5 (right panel), where the ER show up very clearly.

By counting the ER events in each island, the average transparency for each electrode is estimated to be (97.76±0.05)% , very close to the geometrical value.

The transparency has also been measured in the quasi-elastic reaction $^{64}$Zn (beam at 275 MeV) on $^{197}$Au. The scattered beam particles have been detected at 30° with a CH$_4$ pressure of 200 mbar, that stopped them within the IC. A voltage of 200 V was applied and the Mesytec MS-L16 preamplifier and Mesytec MSCF16 amplifier were

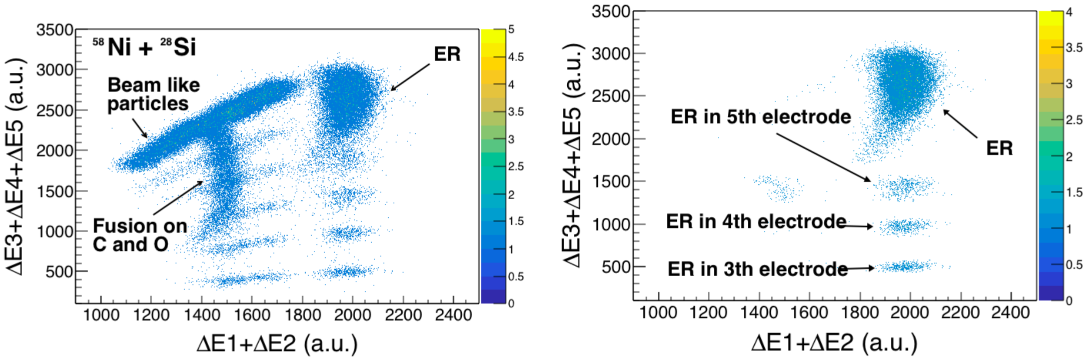

FIGURE 5.5: Energy loss signal provided by the three anodes $\Delta E_3 + \Delta E_4 + \Delta E_5$ as a function of the energy loss in the first two ones $\Delta E_1 + \Delta E_2$. The plot on the right shows the ER stopped in the $\Delta E_3 + \Delta E_4 + \Delta E_5$ - TOF$_2$ matrix (see Fig. 5.4).

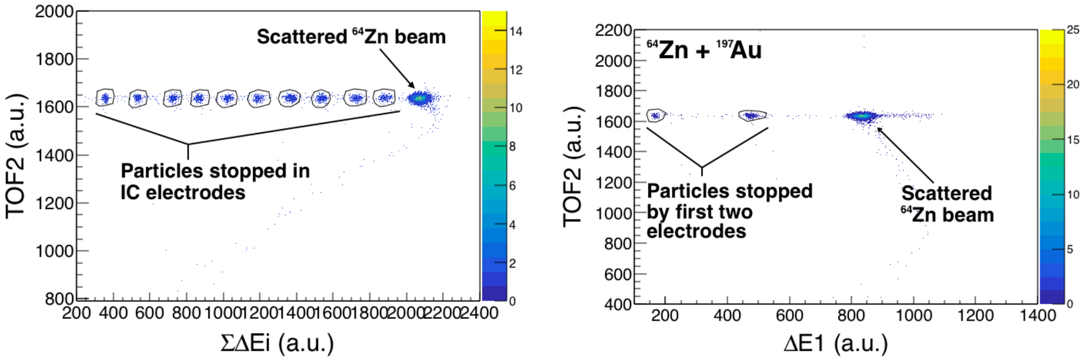

FIGURE 5.6: Time of flight $\mathrm{TOF}_2$ as a function of the total energy loss $\Sigma_i^6 \Delta E_i$ (left panel) and of the energy loss signal provided by the first anode $\Delta E_1$ (right panel). The scattered beam particles stopped by the electrodes are highlighted with the gates.

employed. In particular, the Mesytec amplifier can provide the individual signal of each electrode and their sum. Fig. 5.6 (left panel) shows the time of flight $\mathrm{TOF}_2$ as a function of the total energy loss $\Sigma_i^6 \Delta E_i$. The most intense particles group was produced by the scattered beam. On the left side there is a series of groups with the same time of flight and different energy loss. Those groups are formed when incoming particles are stopped by the tungsten wires on one of the thirteen grids which provide the $\Sigma_i^6 \Delta E_i$ energy loss signal. A similar situation is shown in the matrix of Fig. 5.6 (right panel), where the time of flight $\mathrm{TOF}_2$ vs. the energy loss from the first anode $\Delta E_1$ is plotted. The scattered particles stopped in the first anode and cathode are distributed horizontally on the left side of the scattered beam.

At 30° also the recoiling $^{197}$Au nuclei were detected even if their energy allowed them to only reach the fourth anode. This is clearly visible in the spectrum of $\Delta E_1$ vs. $\Sigma_i^6 \Delta E_i$ in Fig. 5.7. The heavier recoiling $^{197}$Au nuclei have a higher energy loss $\Delta E_1$ with respect to the scattered beam. The corresponding events stopped by the wires are visible.

By selecting only the scattered beam, the particles stopped in each electrode have

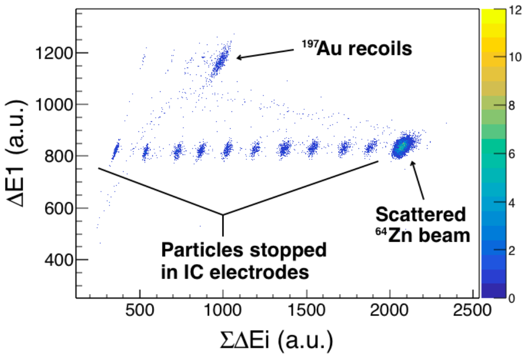

FIGURE 5.7: Matrix of the energy loss $\Delta E_1$ vs. energy loss $\Sigma_i^6 \Delta E_i$. The scattered nuclei of $^{197}$Au and $^{64}$Zn are shown as well as their fraction stopped by the electrodes.

been identified and the transparency has been calculated for each of them. The average transparency of the electrodes is (97.95±0.04)%, which is compatible with the value obtained for the fusion reaction.
The average transparency of one electrode, obtained in the two tests, is (97.88±0.03)%. The transparency of the tilted entrance window is of 69.3%, so that the overall transparency of the ionization chamber is ∼52.5%, if all the thirteen grids are employed.

### 5.1.3 Direct and inverse kinematics reactions

The electrostatic deflector has been used in several studies involving both direct and inverse kinematics fusion reactions. From an experimental point of view, inverse kinematics reactions are more challenging, since the electric rigidities of the beam particles and of the ER are similar. Therefore, the ER and the transmitted beam particles are less separated from each other with respect to a direct kinematics case. Recently, a fusion reaction in inverse kinematics has been succesfully performed using a $^{30}$Si beam on a $^{12}$C target [61]. For this measurement the transverse field ionization chamber was used. The fast IC has to be able to work in inverse kinematics reactions with both stable and radioactive beam, at high counting rates.

The first exotic beams produced by SPES will be of neutron-rich radioactive nuclei with mass in the range 90-160 [54]. The emphasis on neutron-rich isotopes is justified by the fact that this region of the isotope chart has been little explored so far (except for some decay and in-beam gamma spectroscopy following fission) and unexpected phenomena may show up from studies of reaction dynamics. Interesting fusion reactions will be therefore studied with the first SPES beams, as mentioned in 3.2.3.

Test measurements using inverse kinematics have been performed for the fast IC to resemble the future SPES experiments.
The system $^{58}$Ni + $^{28}$Si has been studied. The typical configuration for sub-barrier fusion reaction studies has been adopted, where the separation and identification of ER from the transmitted beam is performed by using the electrostatic deflector and the subsequent detector telescope. A good separation of the ER from the beam has been observed, as well as the identification of the ER from the fusion of $^{58}$Ni on the target C backing and on oxygen generated by target oxydation. This is shown in Fig. 5.3, where the time of flight $TOF_1$ is plotted as a function of the energy loss. As discussed in Sec. 5.1.1, the width of the DAQ gate was 1 $\mu$s and a shaping time of 0.25 $\mu$s for the amplifier was used.

### 5.1.4 Counting rates

The relatively low intensity of the radioactive beams available in the first phase of SPES, makes it impossible to measure fusion reactions with low-efficiency set-ups. An interesting possibility will be placing a detector right along the beam path and detecting the forward-peaked ER with almost 100% efficiency. For this purpose, detectors which can withstand high counting rates have therefore to be employed because of the overwhelming beam and beam-like background. With respect to the transverse-field IC, the collection time has been reduced by a factor of ∼5 in the fast IC, as the distance between the anode and the cathode is smaller. This enables ER identification at high-rate.

In order to test the high-rate performance of the new IC, several tests were performed in both direct and inverse kinematics. High counting rates were obtained by changing both the beam current and the detection angle. The shaping time 0.25 $\mu$s was adopted in all the measurements. The DAQ was triggered by MCP1 signals.

The inverse kinematic fusion reaction $^{58}$Ni+$^{28}$Si was performed with different rates by placing the set-up at detection angles close to 0°. The signals provided by the anodes were combined in two energy loss signals $\Delta E_1 + \Delta E_2$ and $\Delta E_3 + \Delta E_4 + \Delta E_5$. The pressure (30 mbar) did not stop the ER inside the ionization chamber so that an energy signal was provided also by the silicon detector. The set-up was placed at 0.5° with a beam current of 10 pnA. In this condition the counting rate of the IC was about 11 kHz. Figure 5.8 reports the 2D spectra of the time of flight TOF$_3$ as a function of the energy ($E$) provided by the silicon detector and the energy loss ($\Delta E_1 + \Delta E_2$ and $\Delta E_3 + \Delta E_4 + \Delta E_5$) signals. At this rate the background is high, so that a quantitative identification of ER is not easy. The background has been therefore reduced off-line by imposing software conditions. In particular, in one case the ER have been selected as shown in the matrix TOF$_3$-$E$ (Fig. 5.8 upper left panel). In the second case the ER identified through the energy loss signals have been used, which are shown in the 2D spectrum $\Delta E_3 + \Delta E_4 + \Delta E_5$ vs. $\Delta E_1 + \Delta E_2$ of Fig. 5.8 (upper right panel). The matrices obtained with these conditions are plotted in Fig. 5.9, where the time of flight TOF$_3$ as a function of the two energy loss $\Delta E_1 + \Delta E_2$ (upper panels) and $\Delta E_3 + \Delta E_4 + \Delta E_5$ (bottom panels) are shown for the two selection gates. In this way

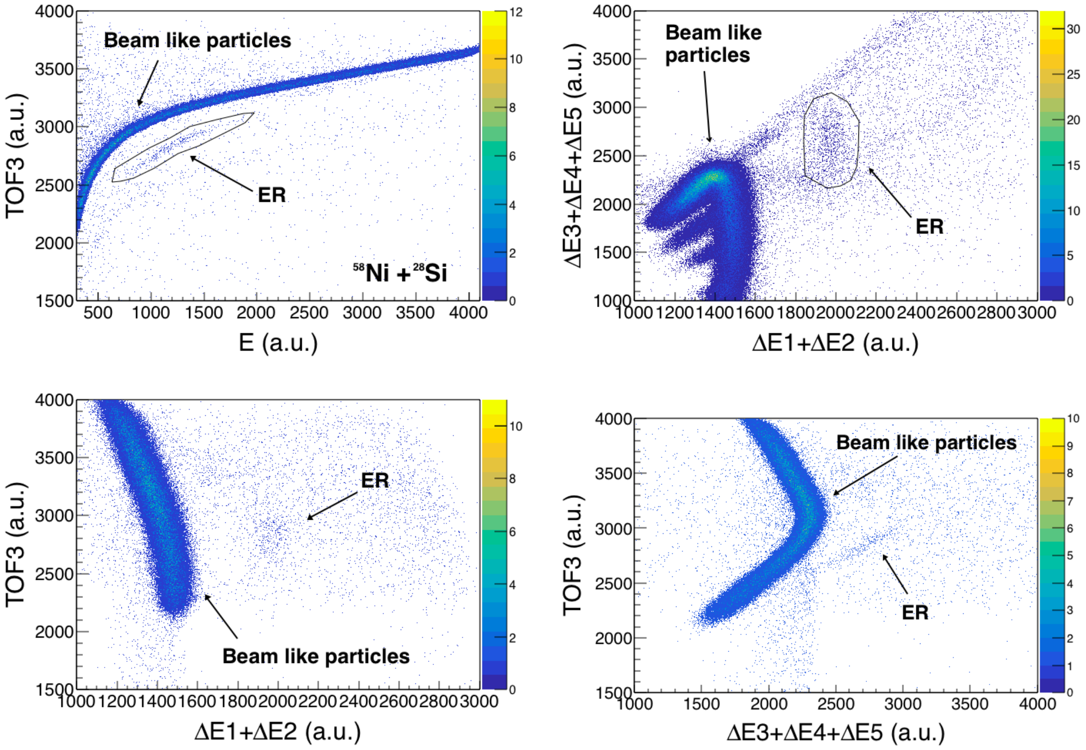

FIGURE 5.8: (Upper left panel) Time of flight TOF$_3$ (silicon detector - MCP$_2$) as a function of the energy $E$ signal provided by the silicon detector. The ER used for the first software selection are inside the gate. (Upper right panel) Energy loss signal $\Delta E_3 + \Delta E_4 + \Delta E_5$ plotted as a function of the energy loss $\Delta E_1 + \Delta E_2$. The ER inside the gate have been used for the second software selection. (Bottom panels) Time of flight TOF$_3$ as a function of the energy loss signals $\Delta E_1 + \Delta E_2$ (left panel) and $\Delta E_3 + \Delta E_4 + \Delta E_5$ (right panel).

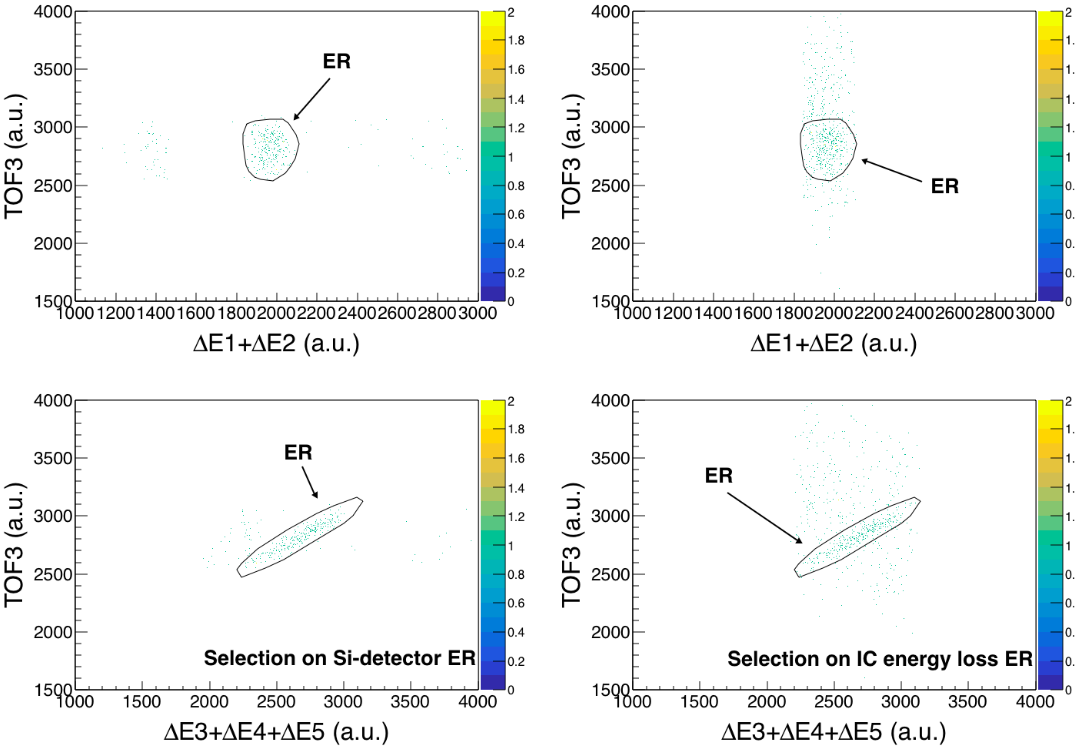

FIGURE 5.9: Time of flight $TOF_3$ as a function of the energy loss signals $\Delta E_1 + \Delta E_2$ (upper panels) and $\Delta E_3 + \Delta E_4 + \Delta E_5$ (bottom panels). On the left a software selection of the ER detected in the matrix $TOF_3$-E (Fig. 5.8 upper left panel) was performed. On the right the selection was done on the ER detected in the matrix $\Delta E_3 + \Delta E_4 + \Delta E_5$ - $\Delta E_1 + \Delta E_2$ (Fig. 5.8 upper right panel).

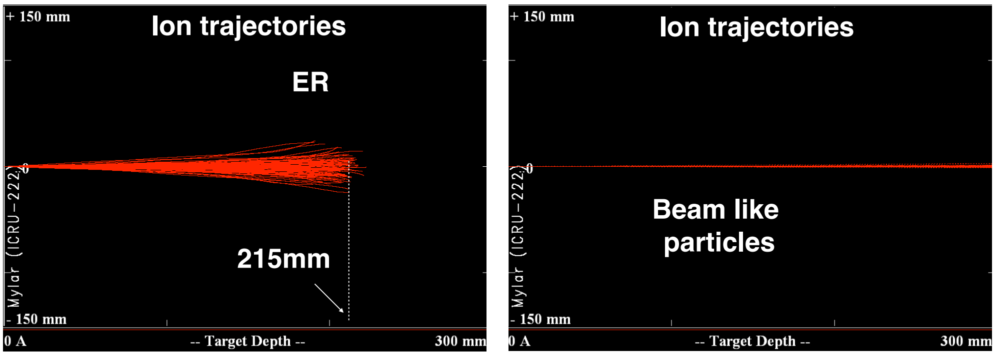

FIGURE 5.10: Ions trajectories in the x-y projection of the IC estimated for the ER (on the left) and the beam (on the right) of the fusion reaction $^{28}Si + ^{100}Mo$. The simulations were performed with the SRIM program [69]. In the simulation of ER, $^{123}Cs$ ions have been considered since they have the highest probability to be formed after the evaporation of the compound nucleus (according to PACE4 [70]). The estimated energy of the $^{123}Cs$ ions is 31.5 MeV. In the case of the beam, $^{28}Si$ ions at the energy of 125 MeV have been considered. The simulation includes the crossing of the Mylar window ($200\mu g/cm^2$) and the methane gas at a pressure of 50 mbar.

the beam-like particles are removed and the background reduced. The selection on the ER detected by the silicon detector (Fig. 5.9 left panels) leads to a more appreciable reduction of the background with respect to the case of the energy loss signals of the IC (Fig. 5.9 right panels). The ER counts obtained by the two selection methods are consistent.

Higher rates have been reached in the $^{28}$Si + $^{100}$Mo reaction, where $^{28}$Si beam had the energy of 125 MeV (above the barrier). During this measurement the pressure inside the chamber was 50 mbar in order to stop the ER before the fifth section. Indeed, as shown in Fig. 5.10 , at the chosen pressure the heavier ER have a range of ∼21 cm (left panel), whereas the beam ions pass through all the detector length (right panel). So the last section of the IC can provide a veto signal to the DAQ for the beam-like particles, which will not be acquired. More details about the advantages of imposing a veto on the sixth IC section will be discussed later.

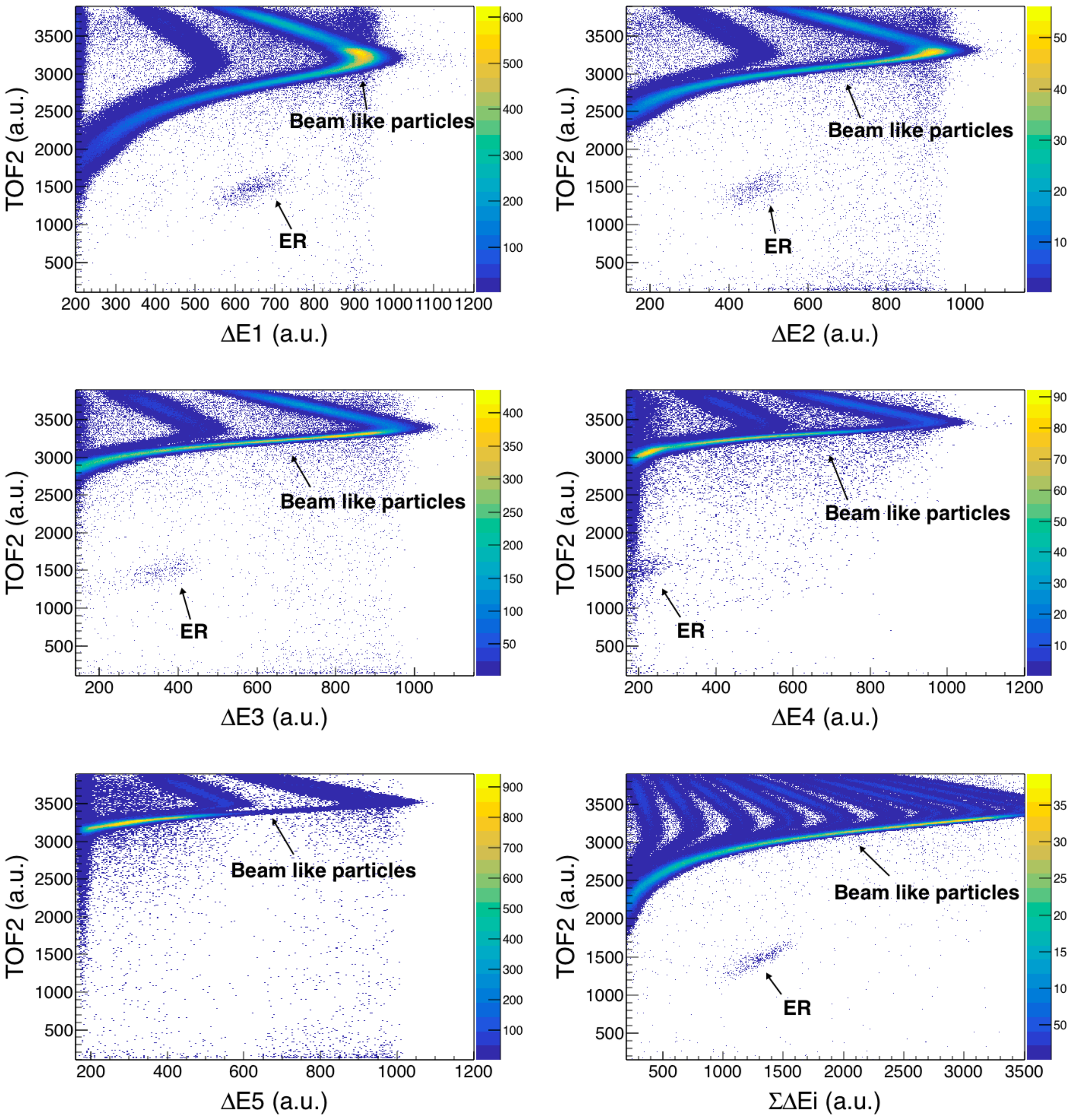

FIGURE 5.11: Time of flight TOF$_2$ (MCP$_1$ - MCP$_2$) as a function of the energy loss signals $\Delta E_i$ (with $i = 1, 2, 3, 4, 5$) and of their sum $\Sigma_i^5 \Delta E_i$ at the rate of 34 kHz.

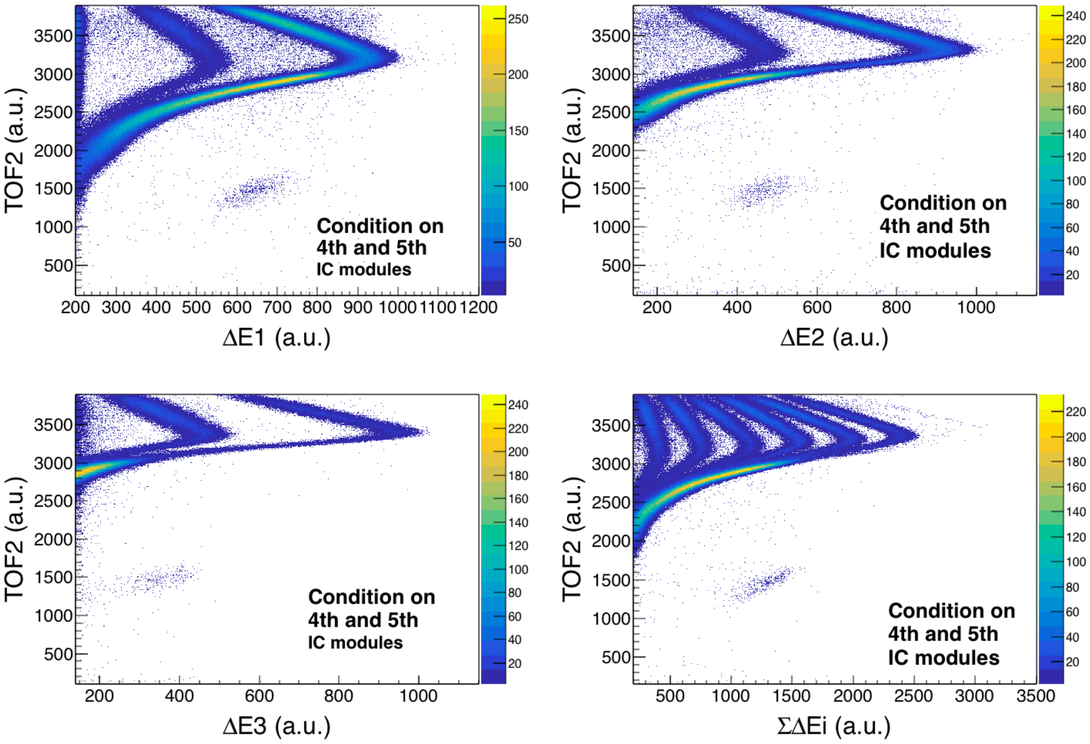

FIGURE 5.12: Time of flight $TOF_2$ as a function of the energy loss signals $\Delta E_i$ (with $i = 1, 2, 3$) and of the sum $\Sigma_i^5 \Delta E_i$ at the rate of 34 kHz. The background of beam like particles events detected by the forth and fifth modules (reported in the matrixes $TOF_2$- $\Delta E_4$ and $TOF_2$- $\Delta E_5$ of Fig. 5.11) were removed by software.

The shaping amplifier Mesytec MSCF16 has been employed in order to acquire the signals provided by each anode and their sum. As in the previous reaction, the $MCP_1$ was used for the trigger of data acquisition.

Figure 5.11 shows the plots obtained using the time of flight $TOF_2$ as a function of the energy loss signals provided by each section $\Delta E_i$ (with $i = 1, 2, 3, 4, 5$) and by their sum $\Sigma_i^5 \Delta E_i$. The set-up was placed at 0° with a beam current of 10 pnA. In this conditions the counting rate of the IC was about 34 kHz. Since the ER were stopped before the fifth section of the IC, the plot of the $TOF_2$ vs. $\Delta E_5$ shows only beam like particles and background signals. Due to the wide energy distribution of the ER a small part of them are detected by the fourth section $\Delta E_4$. Removing by software the background and the beam like particles events detected by fourth and fifth sections, the ER are more clearly identified in the 2D spectra of $TOF_2$ vs. $\Delta E_{1,2,3}$ and vs. the total energy loss $\Sigma_i^5 \Delta E_i$, as shown in Fig. 5.12.

The highest rate measured in the IC is 139 kHz. This has been reached at 0° with a beam current of 5 pnA. The 2D spectra of the time of flight $TOF_2$ vs. $\Delta E_{1,2,3}$ and of the total energy loss $\Sigma_i^5 \Delta E_i$, are shown in Fig. 5.13. Also in this case, the background was reduced by removing unwanted events detected by the fourth and fifth anodes. The background is still high but less with respect to the case where no selections were applied and it is possible to identify the ER. In addition, by selecting the ER detected by the first section $\Delta E_1$ (upper left panel of Fig. 5.13) a further background reduction is possible in the $TOF_2$ vs. $\Sigma_i^5 \Delta E_i$ matrices as shown in Fig. 5.13 (bottom panel). This selection allows a clear identification of the ER. The events on the left

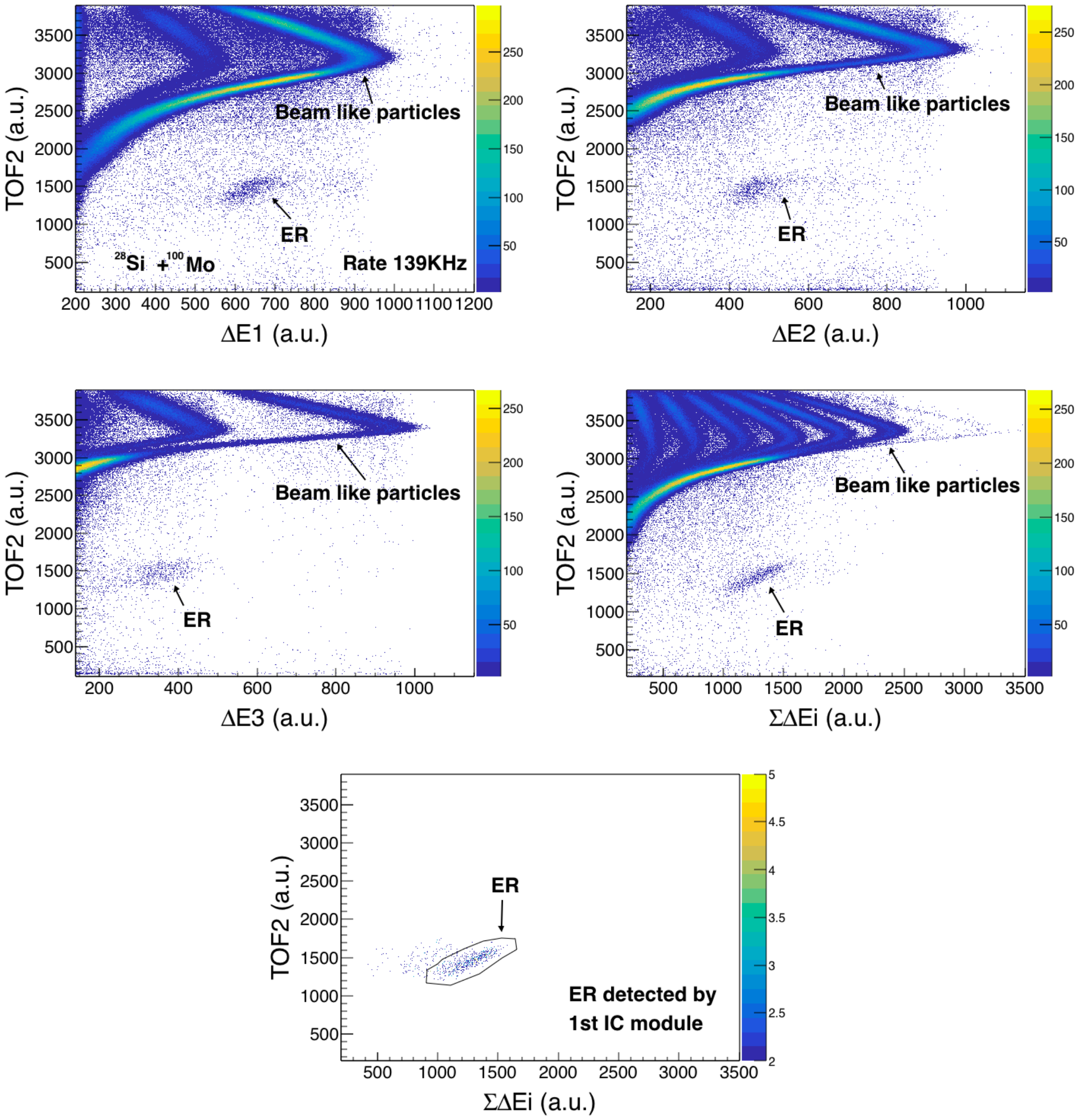

FIGURE 5.13: Time of flight TOF$_2$ as a function of the energy loss signals $\Delta E_i$ (with $i = 1, 2, 3$) and of the sum $\Sigma_i^5 \Delta E_i$ at the rate of 139 kHz. In the bottom panel the TOF$_2$ is plotted as a function of the total energy loss $\Sigma_i^5 \Delta E_i$ following a further selection of the ER detected in the first module of the IC (upper left panel).

of the main ER island are ions stopped by the various electrode grids. These results demonstrate the capability of the Fast IC to work at very high counting rates, much higher than the few kHz reachable with the transverse-field IC.

### 5.1.5 Test with different gases

The performance of the IC has been tested at high counting rates using two gases methane ($CH_4$) and freon ($CF_4$). An important gas property is the stopping power, which determines the pressure required to stop the ions over a certain distance. The stopping power of freon is higher than the one of methane. Therefore, in the same pressure conditions the ions have a shorter range in $CF_4$ with respect to $CH_4$. This is shown in Fig. 5.14 where the range of $^{123}$Cs ions in the two gases is plotted as a function of the energy. At the pressure of 50 mbar the range in freon (red line) is about 2.5 times shorter with respect to methane (blue line). On the other hand, since freon is an electronegative gas, the electrons produced following ionization have a tendency to attach to neutral gas atoms, thus producing negative ions that may deteriorate the signal. Another disadvantage of freon is the possibility of producing the hydrofluoric acid which can damage the wires of the electrodes and the mylar of the entrance window.

The two gases have been employed in two different measurements of the same fusion reaction $^{28}$Si+$^{100}$Mo. The pressure was chosen in order to stop the ER at the fifth section of the IC. The methane pressure was therefore 50 mbar, whereas the freon pressure was 21 mbar, because of the higher stopping power. The MCP$_1$ provided the trigger of the DAQ and the amplifier Mesytec MSCF16 was employed. Figure 5.15 reports the time of flight TOF$_2$ vs. the energy loss provided by the first anode $\Delta E_1$ and vs. $\Sigma_i^5 \Delta E_i$ for the two different gases. The rate of the IC for both measurements was 139 kHz. As shown in the plots, using freon leads to a higher background. This effect can be attributed to the presence of gas impurities in the IC, although the usual gas flow procedure has been applied.

The noise to total ratio $N_{noise}/N_{tot}$ has been obtained for the runs with both gases and was reduced by $\sim 77\%$ in the case of methane with respect to freon, employing the total energy loss (Fig. 5.15, bottom panels). Therefore, no advantages related to the use of freon were observed. This is also partially due to the voltages applied to the detector which did not exceed 500 V. Indeed, the higher drift velocity of electrons in freon occurs at high voltage. In the working voltage range of the IC the electrons drift velocity is comparable for the two gases.

### 5.1.6 Veto conditions

In all the present tests employing the direct kinematic reaction $^{28}$Si+$^{100}$Mo, the signal provided by the sixth section of the IC has been used as veto of the data aquisition. For this purpose, the energy loss signal $\Delta E_6$ was pre-amplified (Mesytec MS-L16) and subsequently fed into a Timing Filter Amplifier (TFA). The output signal of the

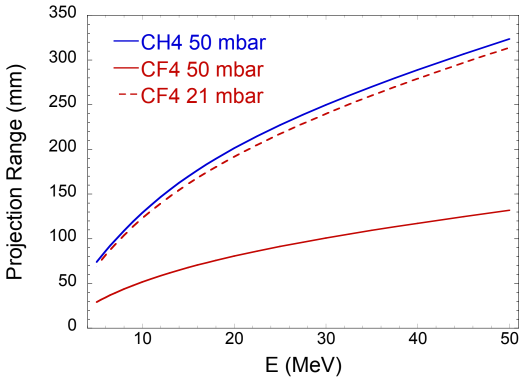

FIGURE 5.14: Range as a function of the energy of the compound nucleus $^{123}$Cs for methane ($CH_4$) (blue line) and freon ($CF_4$) (red line) at 50 mbar. The dashed red line is the result obtained for $CF_4$ at the pressure of 21 mbar employed during the measurement where the energy of $^{123}$Cs was around 39 MeV.

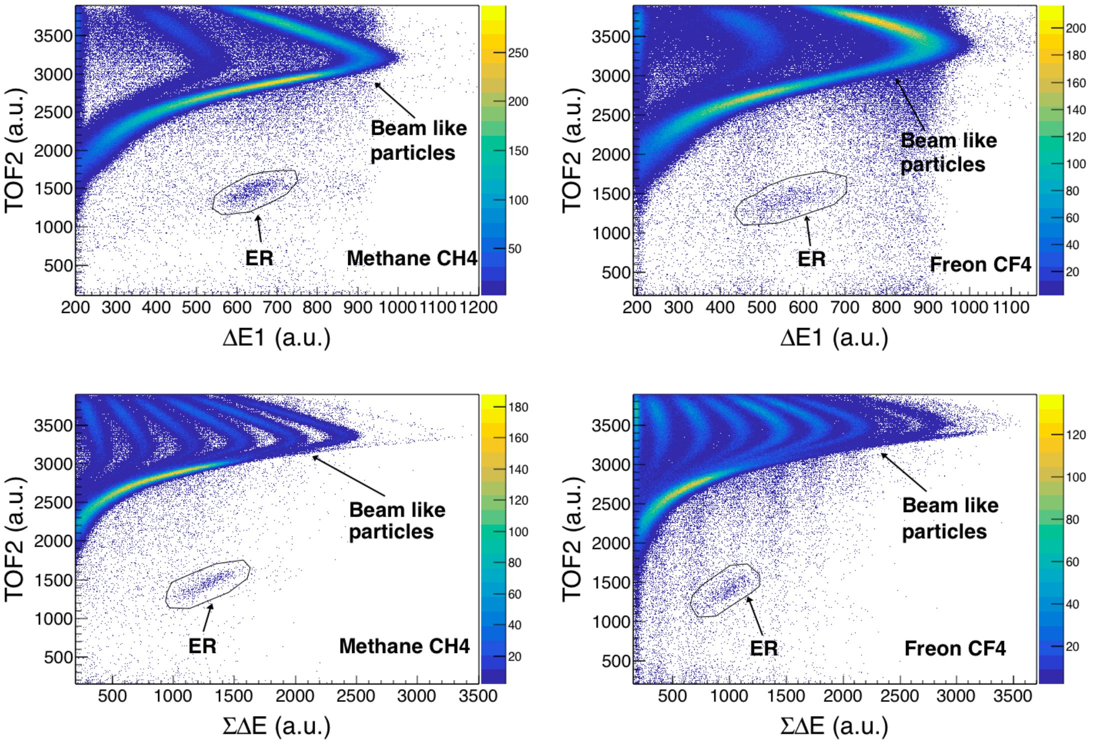

FIGURE 5.15: Time of flight $TOF_2$ as a function of the energy loss $\Delta E_1$ and of the total energy loss $\Sigma_i^5 \Delta E_i$. The measurements performed with methane and freon are on the left and right panels respectively.

TFA was sent to a Leading Edge Discriminator (LED) whose output fed the Gate Generator. The output was sent to the DAQ providing the veto on beam like particles detected by the last section of the IC.

Figure 5.16 shows $TOF_2$ vs. $\Sigma_i^5 \Delta E_i$ measured without any veto condition (left) and imposing the veto (right) as described above. The counting rate during the test was of about 14 kHz, with the detector at 0° and beam current of 2 pnA. The ER are not affected by the use of veto, since the pressure of the gas inside the IC stops the ER

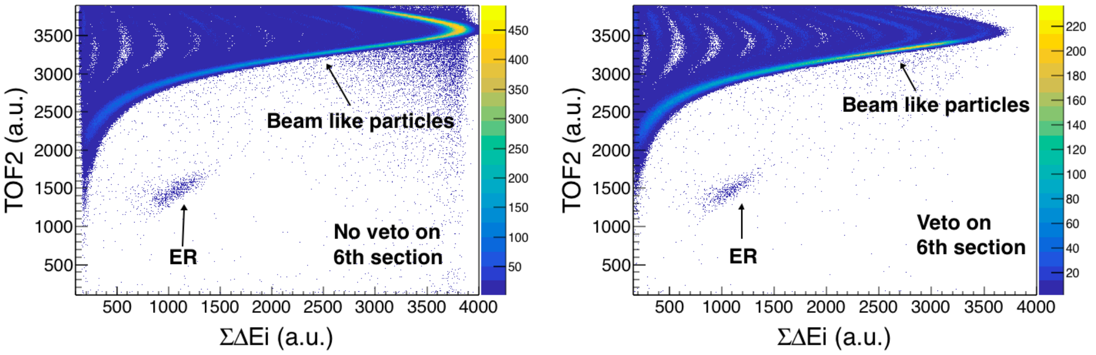

FIGURE 5.16: Time of flight $TOF_2$ as a function of the total energy loss $\Sigma_i^5 \Delta E_i$ of two measurements performed employing the last section of the IC as veto (right panel) and without any veto (left panel).

within the fourth section. On the contrary, the most energetic part of the beam-like particles as well as a fraction of the background is removed.

### 5.1.7 Unipolar vs. bipolar shaping

To optimize the performance of the ionization chamber, various types of preamplifiers (ORTEC2006, Mesytec MS-L16) and shaping amplifiers (Canberra 2020, Mesytec MSCF16) were used. In particular, the Canberra 2020 amplifier provides both unipolar and bipolar output. Kimura et al. [65] adopted a bipolar shaping of the spectroscopy amplifier in order to filter the residual positive ion tails, which lead to baseline fluctuation of the amplifier output. Bipolar shaping is used therefore to restore the baseline of the spectroscopy amplifier and facilitate high counting rate operation.

The possible benefits deriving from the use of a bipolar output were studied using the direct kinematic reaction $^{28}$Si+$^{100}$Mo. For this test a Canberra 2020 amplifier has been provided for each anode signals, following the pre-amplification with the Mesytec MS-L16. As in the previous cases, the gas (freon) pressure stopped the ER inside the detector, before the fifth section. Under these conditions, the signal provided by the sixth section of the IC was employed as veto of the DAQ. The counting rate of the two measurements was 14 kHz, at a detection angle of 0° and with a beam current of 0.5 pnA. The MCP$_1$ provided the trigger to DAQ.
Figure 5.17 reports the plots of TOF$_2$ vs. $\Delta E_1$ (upper panels) and of the total energy loss $\Sigma_i^5 \Delta E_i$ (bottom panels). The results using a bipolar signal from the amplifier

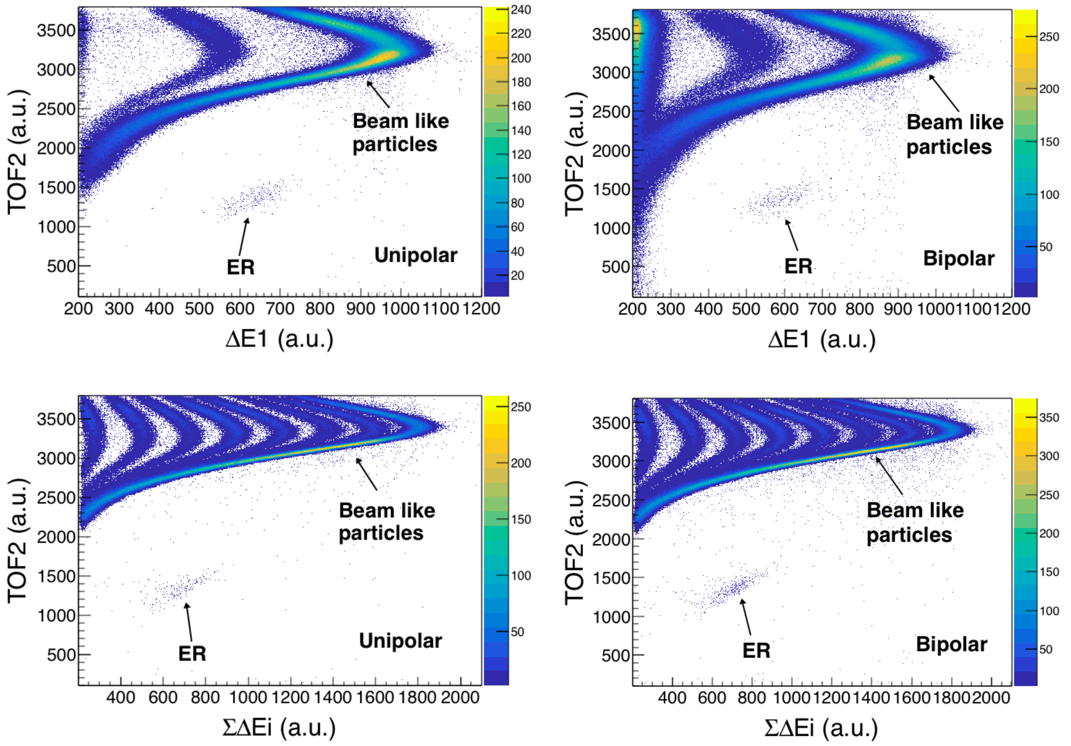

FIGURE 5.17: Time of flight TOF$_2$ as a function of the energy loss measured by the first anode $\Delta E_1$ and of the total energy loss $\Sigma_i^5 \Delta E_i$ for unipolar (left) and bipolar (right) shaping of the amplifier output.

have been shown on the right panels (Fig. 5.17) and no visible improvements are observable with respect to the unipolar one. The noise to total ratio $N_{noise}/N_{total}$ is reduced by 12% in the case of the unipolar shaping.
Since bipolar shaping amplification does not introduce significant advantages, the Mesytec MSCF16 amplifier, which provides only unipolar shaped output signals, will be used in future experiments.

### 5.1.8 Z and energy resolution

#### Z resolution

The ALPI-PIAVE accelerator provided a $^{64}$Zn beam at the energy of 275 MeV on a $^{54}$Fe target. In this reaction the proton stripping channels are the dominant quasi-elastic transfer channels and were used to estimate the Z resolution. For this purpose, the whole set-up was placed at $\theta_{lab}$=30° near the grazing angle of the reaction. At this detection angle the direct beam was stopped inside the reaction chamber, so that the electrostatic deflector was not necessary and no fields were applied. During this measurement the two single energy loss signals were summed together $\Delta E_1 + \Delta E_2$ and the Mesytec MSCF16 amplifier provided the total energy $\Sigma_i^6 \Delta E_i$. The pressure of methane in the IC was 200 mbar.
Figure 5.18 (upper panels) reports the plots of the time of flight TOF$_2$ as a function of the energy loss of the first two IC sections $\Delta E_1 + \Delta E_2$ and of the total energy $\Sigma_i^6 \Delta E_i$. The bottom panel shows $\Delta E_1 + \Delta E_2$ vs. $\Sigma_i^6 \Delta E_i$. In all the matrices the most intense particle group consists mainly of scattered beam and of a mionr contribution of neutron transfer channels (Z=30). The particles stopped in each electrode are well identified. The stripping channels are clearly visible in the TOF$_2$ vs. $\Delta E_1 + \Delta E_2$ and $\Delta E_1 + \Delta E_2$ vs. $\Sigma_i^6 \Delta E_i$ spectra. In Fig. 5.18 (bottom panel), they overlap with the particles stopped by the electrodes.

Typically, to estimate the resolution in Z the plot where the energy loss and the residual energy are correlated $\Delta E_1 + \Delta E_2$ vs. $\Sigma_i^6 \Delta E_i$ is preferred over the matrix TOF$_2$ vs. $\Delta E_1 + \Delta E_2$, since the separation of the transfer channels is more evident. However, in this case the identification of the transfer channels in the matrix $\Delta E_1 + \Delta E_2$ vs. $\Sigma_i^6 \Delta E_i$ requires the implementation of some changes via software. To clearly identify the stripping channels in this matrix, the particles stopped by the wires have been removed and the scattered beam as well as the transfer channels, identified in the TOF$_2$ vs $\Delta E_1 + \Delta E_2$ and TOF$_2$ vs $\Sigma_i^6 \Delta E_i$ spectra, have been selected by software (as shown in Fig. 5.18 upper panels). The resulting plot was rotated by 8.9° so that the islands of scattered particles and transfer channels are perpendicular to the y-axis, and the result is shown in Fig. 5.19. The two proton stripping (-2p) channel (Z=28) is well separated from the scattered beam (Z=30). Also the recoiling ions of the $^{54}$Fe target are detected and they overlap with -4p channel, resulting in a single cluster of ions with Z=26. The Z resolution ΔZ can be obtained from the following equation:

$$\Delta Z(Z) = \frac{2\Delta CH(Z)}{CH(Z+1) - CH(Z-1)} \tag{5.3}$$

where $\Delta CH(Z)$ denotes the FWHM of the peak corresponding to the atomic number Z and CH(Z) is the channel number of the centroid. The spectrum in Fig. 5.20 (left panel) is the projection in logarithmic scale onto the y-axis of the matrix in Fig. 5.19. The peak corresponding to the scattered beam is well separated from the two proton stripping (-2p) channel, whose atomic number is Z=28.

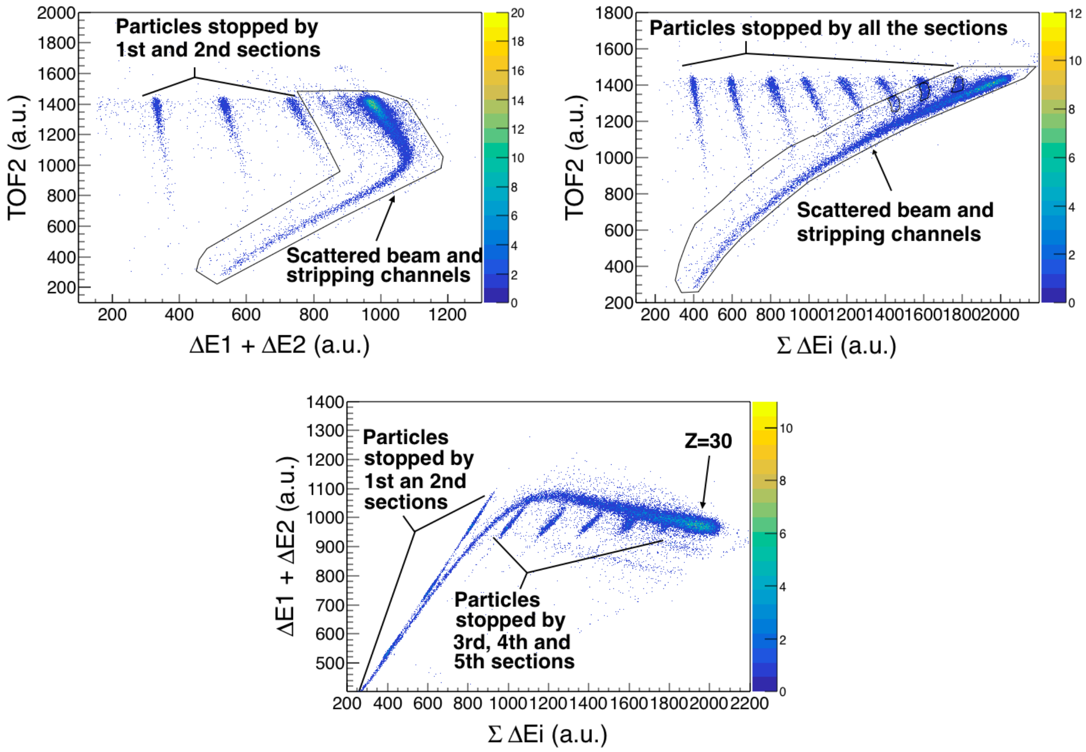

FIGURE 5.18: Matrices TOF$_2$ vs. $\Delta E_1 + \Delta E_2$ and TOF$_2$ vs. $\Sigma_i^6 \Delta E_i$ (upper panels). $\Delta E_1 + \Delta E_2$ plotted as a function of the total energy $\Sigma_i^6 \Delta E_i$ in the bottom panel. The scattered $^{64}$Zn beam (Z=30) and the particles stopped in various electrodes can be identified.

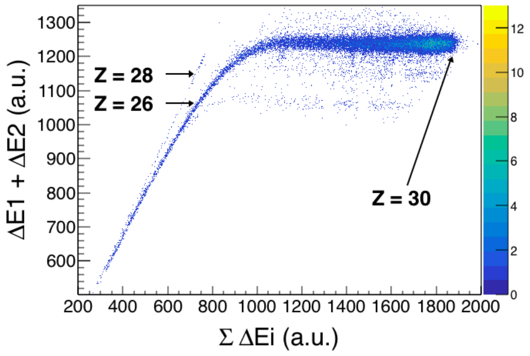

FIGURE 5.19: $\Delta E_1 + \Delta E_2$ as a function of the total energy $\Sigma_i^6 \Delta E_i$. Unlike the matrix in Fig. 5.18 (bottom panel), the particles stopped in the electrodes have been removed by software and the plot has been rotated by 8.9°. The stripping channels (-2p and -4p) as well as the recoiling $^{54}$Fe (Z=26) ions are well separated from the scattered $^{64}$Zn (Z=30).

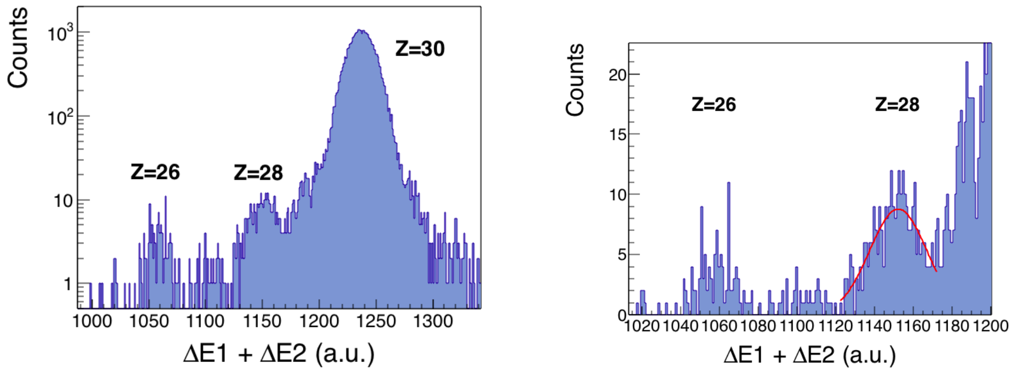

FIGURE 5.20: The y-axis projection of the matrix $\Delta E_1 + \Delta E_2$ vs $\Sigma_i^6 \Delta E_i$ (Fig. 5.19) in logarithmic scale (left panel). The scattered $^{64}$Zn beam peak (Z=30) is well separated from the two (-2p) and four (-4p) protons stripping channels, identified as Z=28 and Z=26 respectively. The recoiling $^{54}$Fe (Z=26) ions overlap with the -4p stripping chanel. The Z=26 and Z=28 peaks are shown in linear scale in the spectrum on the right. A gaussian fit was performed on the -2p stripping channel in order to extract the FWHM of the peak and estimate the Z-resolution of the IC.

The recoiling $^{54}$Fe ions overlap with the four proton stripping (-4p) channel resulting in a single peak at the location of Z=26. On the right panel of Fig. 5.20 the Z=26 and Z=28 peaks are reported in linear scale. By using Eq. 5.3, the Z resolution has been therefore estimated by taking into account the distance between the two centroids and the FWHM has been obtained through a gaussian fit of the Z=28 peak (plotted with a red line). The Z resolution is $\Delta Z/Z \sim 1/38$.

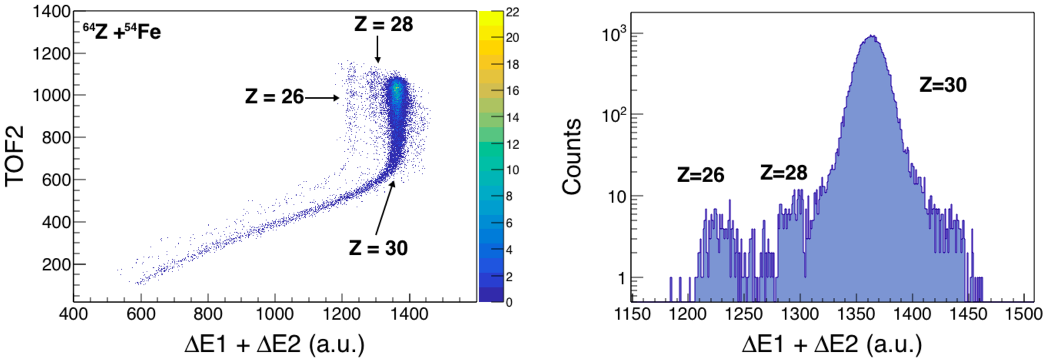

FIGURE 5.21: Time of flight TOF$_2$ plotted as a function of $\Delta E_1 + \Delta E_2$ (left panel). The matrix of Fig. 5.18 (upper left panel) has been rotated by 18°. The stripping channels (-2p and -4p) as well as the recoiling $^{54}$Fe (Z=26) ions are well separated from the scattered $^{64}$Zn (Z=30). The x-axis projection is reported in logarithmic scale on the right panel. The Z=30 peak is well separated by the two (-2p) and four (-4p) protons stripping channels, identified as Z=28 and Z=26, respectively. The $^{54}$Fe (Z=26) ions overlap with the -4p stripping channel.

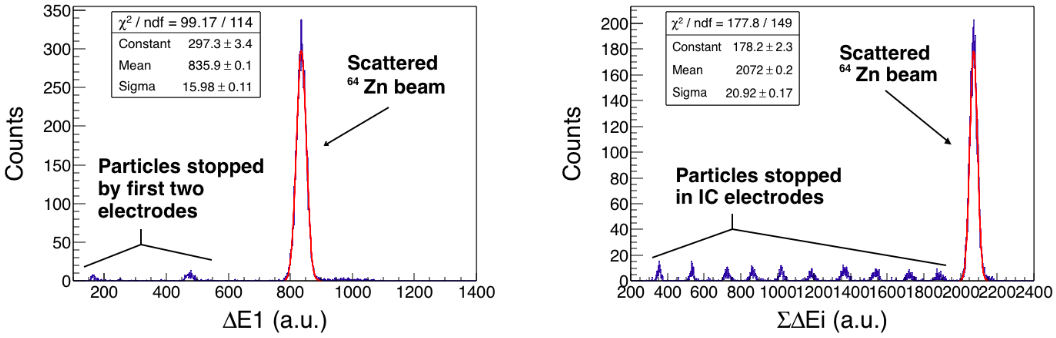

FIGURE 5.22: X-axis projections of the matrices TOF$_2$ vs $\Delta E_1$ (see Fig. 5.6) on the left and TOF$_2$ vs $\Sigma_i^6 \Delta E_i$ on the right. The recoiling $^{197}$Au ions have been removed by software. The scattered $^{64}$Zn beam peaks were fitted with a gaussian function in order to estimate the energy resolution.

As a further check, the Z resolution was also obtained from the projection on the x-axis of the matrix TOF$_2$ vs. $\Delta E_1 + \Delta E_2$, which has been rotated by 18° for an appropriate projection on the x-axis, as shown in Fig. 5.21 (left panel).
The right panel of Fig. 5.21 reports the x-axis projection of the plot. The peak corresponding to the scattered beam is well separated from the two proton stripping (-2p) channel, which corresponds to Z=28. The recoiling $^{54}$Fe ions overlap with the four proton stripping (-4p) channel resulting in a single peak at Z=26. In Fig. 5.21 (right panel) the Z=28 peak is less clearly defined than the one shown in Fig. 5.20. However a gaussian fit has been performed and the Z resolution has been obtained by using Eq. 5.3. In this way the Z resolution is slightly worse $\Delta Z/Z \sim 1/35$ but comparable with the result of 1/38.

### Energy resolution

The system $^{64}$Zn + $^{197}$Au was used in order to estimate the energy resolution of each section of the IC by measuring the elastic scattering of the beam. The detection angle was 30° also in this case and the recoiling Au ions could be observed (see Fig. 5.7 in the section 5.1.2). A methane pressure of 200 mbar was therefore chosen in order to stop the $^{197}$Au recoiling ions inside the chamber and to separate them from the scattered beam. No fields were applied to the electrostatic deflector and the Mesytec MSCF16 amplifier was used for the energy loss signal provided by each section $\Delta E_i$ and by their sum $\Sigma_i^6 \Delta E_i$. The MCP$_1$ provided the trigger for the DAQ.
The recoiling $^{197}$Au ions are well identified in the 2D spectra $\Delta E_1$ vs. $\Sigma_i^6 \Delta E_i$ of Fig. 5.7. The 2D spectra of TOF$_2$ as a function of the energy loss $\Delta E_1$ and by the combination of all the six sections $\Sigma_i^6 \Delta E_i$ are presented in Fig. 5.6 (Sec. 5.1.2). The projection on the x-axis of these matrices are shown in Fig. 5.22. In these 1D spectra the highest peak is the scattered beam whereas the lower ones on the left are the scattered beam particles stopped by the wires. In both spectra the recoiling $^{197}$Au ions have been removed by software. In order to estimate the energy resolution, the elastic scattering beam peaks were fitted with a gaussian function. The energy resolution of the single section is (4.35±0.03)%, whereas the resolution of the total energy signal is (2.09±0.02)%. These estimates take into account the straggling in the target (0.23 MeV, 0.09%), the kinematic widening (1.15 MeV, 0.5%) and spread (0.04%).

## 5.2 Summary of the obtained results

The performance of the new fast ionization chamber has been studied in several tests with stable beams. The 13 tilted grid electrodes (having a transparency of 98% each) significantly decrease the drift time of the electrons to anodes with respect to a conventional IC with transverse field, which enables ion detection at high counting rates. The detector has been used with a shaping time of $0.25\,\mu$s in the amplifier. The IC proved to be able to work with a gate width of the DAQ shorter than the $4\,\mu$s, usually adopted because of the delayed response of a conventional IC. It has been found that it is possible to work with the new IC with a gate width as short as $1\,\mu$s.

Despite the rate limitations of DAQ, various tests have been performed with very high counting rates in the IC, measured by a scaler, even if not all those events could be effectively handled by the DAQ system. Indeed, the detector has been tested up to a rate of $\simeq 140$ kHz. A veto signal can be produced, by adjusting the gas pressure so that only the transmitted beam (and not the ER) reaches the last anode. This veto helps cleaning up the spectra by rejecting the unwanted beam-like events. The ER can be therefore better identified, also by the use of software conditions. To overcome the limited acquisition rate, a new DAQ which can treat higher rates is planned to be developed and installed.

A proper gas selection has been performed by testing the IC with freon and methane, at the highest rate conditions. Following this test, the choice of methane resulted the most convenient one. This was expected since the electron drift velocity in freon is not higher than in methane for the voltage applied to the IC in typical working condition. Moreover, the use of freon is in general more critical due to stringent purity requirements.

A transfer reaction was performed in order to estimate the Z-resolution of the IC. The result is 1/38 for $^{64}$Zn ions at about 3 MeV/A. The energy resolution of the IC is of the order of $\cong 2.09\%$ with $^{64}$Zn ions at the energy of 2.3 MeV/A.

# Chapter 6

# Study of sub-barrier fusion of $^{50}$Ti,$^{51}$V+$^{36}$S systems

## 6.1 Physical motivation

Most of the existing studies on near- and sub-barrier fusion reactions concern even-even projectile and target nuclei since the theoretical analysis of the data is more straightforward in such cases. However, when non-zero spin nuclei are involved in the fusion process, interesting effects are expected, still awaiting experimental evidence.

The non-zero spin of the ground state can in general be associated with a deformation. Under this condition, the fusion cross section should be calculated for each magnetic substate of the ground state spin. The ion-ion potential and consequently the height of the Coulomb barrier would be different for each m-substate. This would affect the fusion cross section which is the average over the m-substates, and the effect should be particularly evident below the barrier.

At present, only few studies have been performed on this topic and one of them concerned the $^{9}$Be + $^{144}$Sm system [71, 72], where the ground state spin of $^{9}$Be is 3/2+. The fusion cross section was calculated for each initial magnetic quantum number, m = 1/2 and 3/2 and the average cross section was compared to the measurements. The Coupled Channels (CC) calculations which explicitly considered the two magnetic substates m = 1/2 and 3/2 (the m = -1/2 and -3/2 substates have not been included for symmetry reasons), were able to reproduce the data, see Fig. 6.1 (bottom panel).

Because of the large quadrupole deformation of the $^{9}$Be, conventional calculations based on a deformed Woods-Saxon potential were not performed since they could be unrealistic [73]. A double-folding potential was used, i.e. the effective M3Y interaction supplemented with a repulsive term (see Chapter 2). The entrance potentials were calculated separately for the two magnetic substates resulting largely different, as shown in Fig. 6.1 (upper panel). Indeed, the magnetic quantum numbers m = 1/2 and 3/2 refer to a z-axis that points in the direction of the relative position of projectile and target. Consequently, the m = 3/2 channel corresponds to an orientation where the tip of the deformed $^{9}$Be points towards the target, whereas the m = 1/2 channel corresponds to the belly pointing towards the target. As a result the Coulomb barrier in the entrance channel for the m = 3/2 is lower than the one observed for m = 1/2.

Another experiment used $^{27}$Al as projectile on several germanium isotopes [74]. These measurements and data analysis were focused on the effect on fusion of the vibrational excitations of the Ge isotopes. The experimental results were analyzed

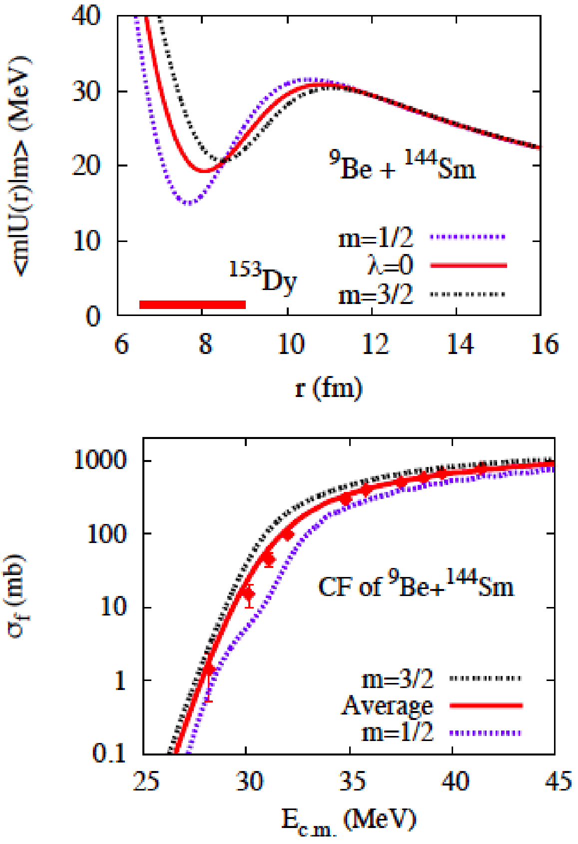

FIGURE 6.1: Upper panel: entrance potentials for $^{9}$Be + $^{144}$Sm [71]. The monopole potential (solid red line) and the potentials (dotted curves) for the magnetic quantum numbers $m = 1/2$ and 3/2 of the 3/2 ground state of $^{9}$Be. Lower panel: measured cross sections for the complete fusion of $^{9}$Be + $^{144}$Sm [72] compared to calculations for $m = 1/2$ and 3/2 and the average cross section (solid red curve). The curve for $m = 3/2$ dominates the cross section at all energies, consistently with the lower Coulomb barrier for this magnetic substate.

within the CC model using the rotating frame approximation [75], and the calculations were repeated with different values of the initial spin projection, $m = 1/2$, 3/2, and 5/2.

The last example is a more recent study of the $^{27}$Al + $^{45}$Sc system [76]. The results were focused on the possible consequence of the positive fusion Q-value of the system on the hindrance phenomenon. However the employed M3Y potentials showed a slightly different behaviour for the different substates ($m = 1/2$, 3/2, and 5/2), and the average values have been used.

In the present work a detailed comparative study of the two systems $^{36}$S + $^{50}$Ti, $^{51}$V has been performed, by measuring the fusion excitation functions for the two systems, where no previous data were available.

The shell-model structure of the nucleus $^{51}$V is relatively simple, consisting of three protons outside the doubly magic $^{48}$Ca core. In fact, the $^{51}$V has a $7/2^-$ ground state and the two lowest excited states are a $5/2^-$ at 0.320 MeV and a $3/2^-$ at 0.928 MeV, both connected to the ground state by strong B(E2) transitions.
The quadrupole moment of the ground state has been measured and its most recent value is $Q = -0.043 \pm 0.005$ b [77].

The $^{50}$Ti is a neutron closed-shell nucleus, having the lowest quadrupole vibration at 1.554 MeV with $\beta_2 = 0.16$. The $3^-$ state is high (4.410 MeV) and weak ($\beta_3 = 0.14$). The common projectile $^{36}$S has a N=20 closed shell, and its structure is rigid and well known, so that its effect on fusion cross sections can be safely calculated. The nominal barriers differ by 2 MeV for the two systems in the laboratory system, so that each $^{36}$S beam energy has been used for both targets.

The aim of the measurements was to identify differences in the fusion excitation function of the two cases, that may possibly be attributed to the rather large non-zero spin ($7/2^-$) of the $^{51}$V ground state. The four magnetic substates m = 1/2, 3/2, 5/2 and 7/2 produce different Coulomb barriers and have to be treated individually in the CC calculations. A different ion-ion potential and consequently a different barrier, is expected for each of them. It is therefore interesting to investigate if the shape of the barrier distribution keeps a trace of those different barriers and/or if a difference of the barrier distributions of the two systems shows up, that may be associated with the non-zero spin of $^{51}$V. The sections below describe how the two excitation functions have been measured with small energy steps and good statistical accuracy, as in previous measurements of this kind.

## 6.2 Experimental procedure

The experiment was designed to perform a detailed measurement of the fusion excitation function for the two systems $^{36}$S + $^{50}$Ti, $^{51}$V and was run for eight days. The XTU-Tandem accelerator provided the $^{36}$S beam at an average current of 10 pnA. The targets were 50 $\mu$g/cm$^2$ in thickness for both $^{51}$V and $^{50}$TiO$_2$, the later one enriched to 90.3% in mass 50. The carbon backing and the vanadium and titanium layers introduced an average beam energy loss of around 750 – 850 keV, which was taken into account in the analysis.

The energy range to study the excitation function was chosen around the value of the Coulomb barrier of the two systems, estimated using the Akyüz-Winther potential [9], whose parameters are shown in Table 6.1, together with the resulting barriers. The Coulomb barrier is higher by about 2 MeV for the reaction $^{36}$S + $^{51}$V with respect to the $^{36}$S + $^{50}$Ti system. Therefore, the measurements have been performed in two different energy ranges: $E_{lab} = 73 - 100$ and $76 - 100$ MeV, for $^{50}$Ti and $^{51}$V, respectively. The $^{51}$V and $^{50}$Ti targets were mounted on the six-position target holder.

The energy was gradually changed starting from the highest value, in order to minimize hysteresis phenomena in the analyzing magnet placed at the exit of the

TABLE 6.1: Well depth $V_0$, radius $r_0$ and diffusivity $a_0$ of the Akyüz-Winther potential and the height $V_B$, the position $R_b$ and the curvature $\hbar\omega$ of the Coulomb barrier for the two systems.

(a) $^{50}$Ti + $^{36}$S system

| $V_0$ (MeV) | $r_0$ (fm) | $a_0$ (fm) | $V_B$ (MeV) | $R_B$ (fm) | $\hbar\omega$ (MeV) |
|---|---|---|---|---|---|
| 62.43 | 1.17 | 0.66 | 46.90 | 10.05 | 3.41 |

(b) $^{51}$V + $^{36}$S system

| $V_0$ (MeV) | $r_0$ (fm) | $a_0$ (fm) | $V_B$ (MeV) | $R_B$ (fm) | $\hbar\omega$ (MeV) |
|---|---|---|---|---|---|
| 62.96 | 1.17 | 0.66 | 49.00 | 10.05 | 3.47 |

accelerator. At every energy change the beam was refocused on the target using a quartz .

Fusion cross sections have been determined by direct detection of the fusion evaporation residues by separating them from the beam and beam-like particles using the electrostatic deflector. The voltage applied to the electrodes was modified during the experiment to maximize the number of particles detected after the deflector stage (yield of ER). The yield measurement was performed at the highest energy (100 MeV) and the maximum transmission was reached at the voltage of ±16.5 kV on each deflector plate. For the other beam energies the applied voltage was scaled for the estimated electrical rigidity of the ER.

The ER were identified downstream of the deflector by a double Time-of-Flight (ToF)–ΔE–Energy telescope composed of two micro-channel plate time detectors followed by the ionization chamber IC and by the silicon detector placed in the same gas ($CH_4$) volume of the IC. The new Fast IC (see Chapter 4) was employed for the first time in a fusion reaction experiment. The signals provided by the five anodes were combined in a total energy loss signal ΔE. The silicon detector placed at the end (most downstream) of the detector telescope measured the residual energy of the ER and gave the start signal for the two TOF as well as the trigger for the data acquisition.

Four silicon detectors placed in the reaction chamber symmetrically around the beam direction at the same scattering angle have been used to monitor the beam and to normalize the fusion yields to the Rutherford scattering cross section.

Two ER angular distributions were measured at the energies of 80 and 90 MeV in the range from -6° to +9°.

## 6.3 Analysis

The telescope provides three times of flight $TOF_{1,2,3}$ (see Chapter 4.1), a total energy loss $\Delta E$ and a residual energy $E$. By correlating these variables, it is possible to identify the ER and estimate the fusion cross sections of both reactions.

Figure 6.2 shows the three times of flight as a function of the residual energy (on the left) and of the total energy loss $\Delta E$ (on the right) for the $^{36}$S + $^{50}$Ti system at 100 MeV incident energy. The ER are well separated from the degraded beam and from the fusion of $^{36}$S with the carbon and the oxygen of the target.

Following fusion, a fraction of the compound nuclei evaporates alpha particles resulting in ER lighter than the ones formed by nucleon evaporation. This fraction is well separated from the majority of ER as shown Fig. 6.2 (left panels) and obviously was included in the total yield of the ER.

The Monte Carlo code *PACE*4 [70] (determining the decay sequence of an excited nucleus) was used to calculate the fraction of ER following alpha particles emission. The calculations overestimates the experimental result by 77% and 52% above and below the barrier, respectively. However, according to the *PACE*4 calculations, the alpha emission probability decreases with decreasing energy, becoming negligible at energies below the Coulomb barrier, as observed in the experiment.

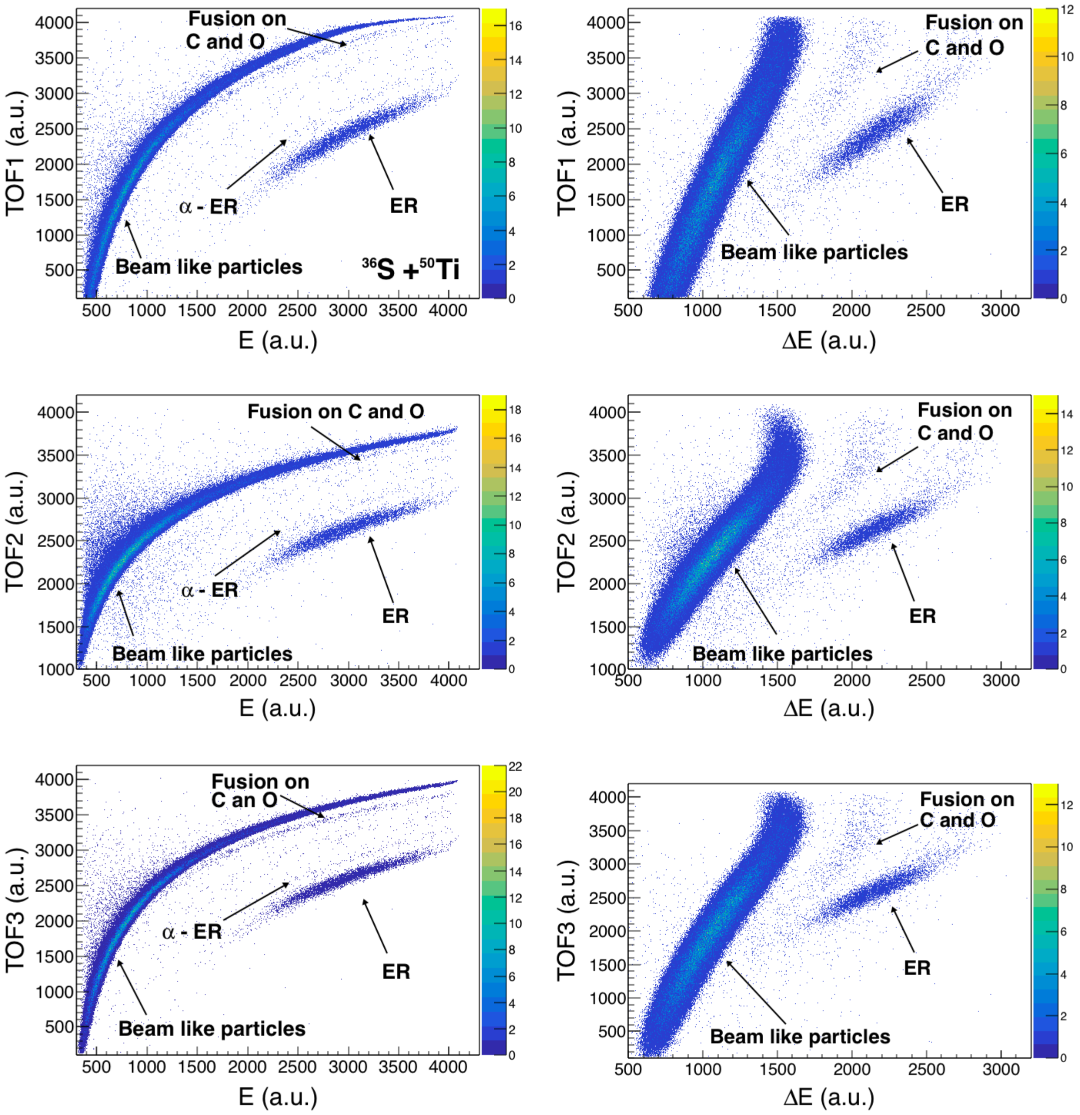

FIGURE 6.2: Time of flights $TOF_1$, $TOF_2$ and $TOF_3$ as a function of the residual energy $E$ (on the left) and of the total energy loss (on the right) for the reaction $^{36}S + ^{50}Ti$ at the beam energy of 100 MeV. The ER produced by evaporation of one alpha-particle are indicated as $\alpha$-ER and are clearly visible in the matrices of the time of flights as a function of the energy. On the contrary, in the matrices $TOF_{1,2,3}$ vs ΔE they are not distinguishable and are included in the cluster of all other ER. The fusions of the $^{36}$S beam with the carbon and oxygen of the target are also visible.

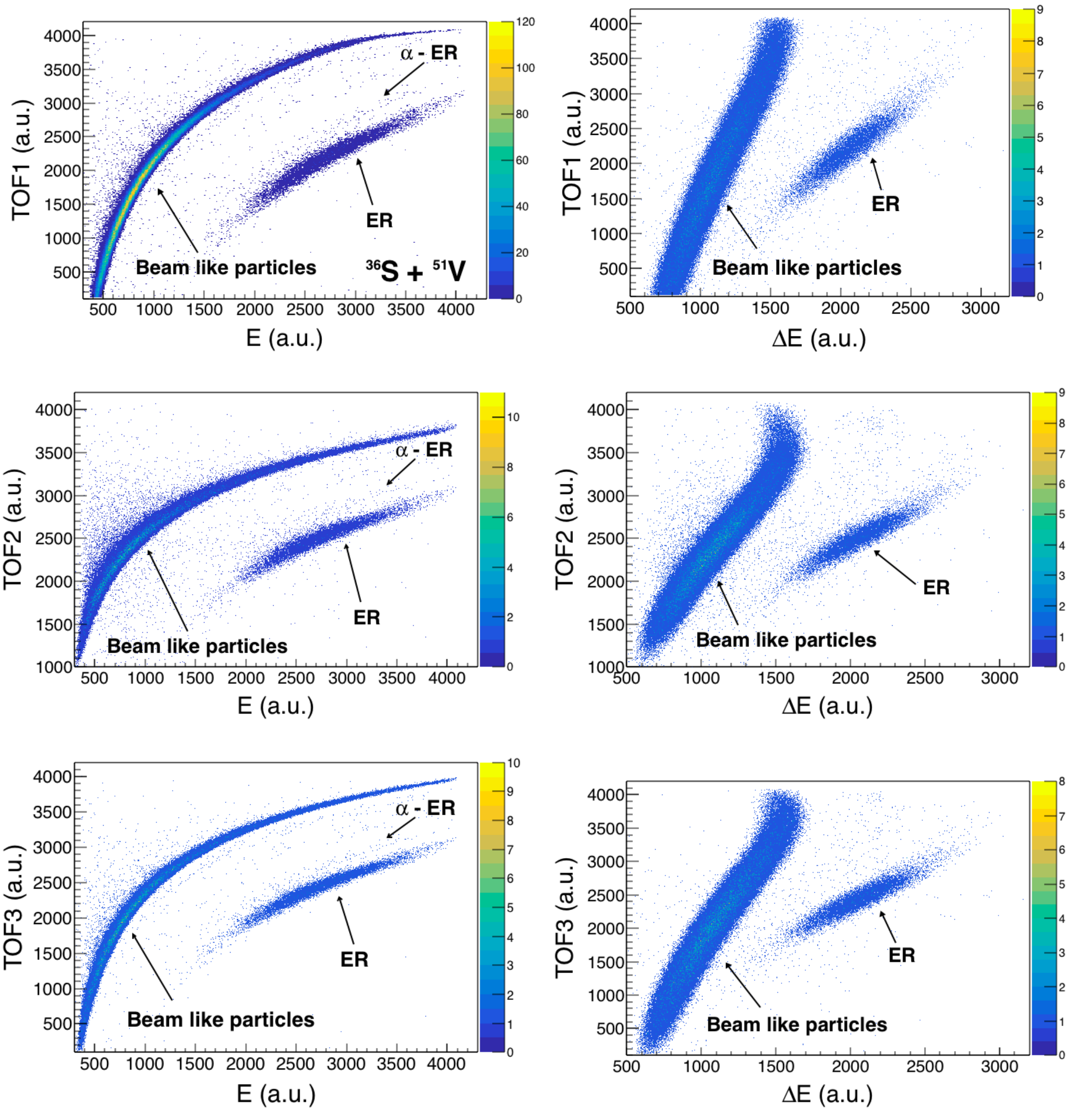

FIGURE 6.3: Time of flights TOF$_1$, TOF$_2$ and TOF$_3$ as a function of the residual energy $E$ (on the left) and of the total energy loss (on the right) for the fusion reaction $^{36}$S + $^{51}$V at the beam energy 100 MeV. The ER produced by evaporation of one alpha-particle are indicated as $\alpha$-ER and are clearly visible in the matrices showing the time of flights as a function of the energy. On the contrary, in the matrices TOF$_{1,2,3}$ vs ΔE they are not distinguishable and are included in the cluster of all other ER.

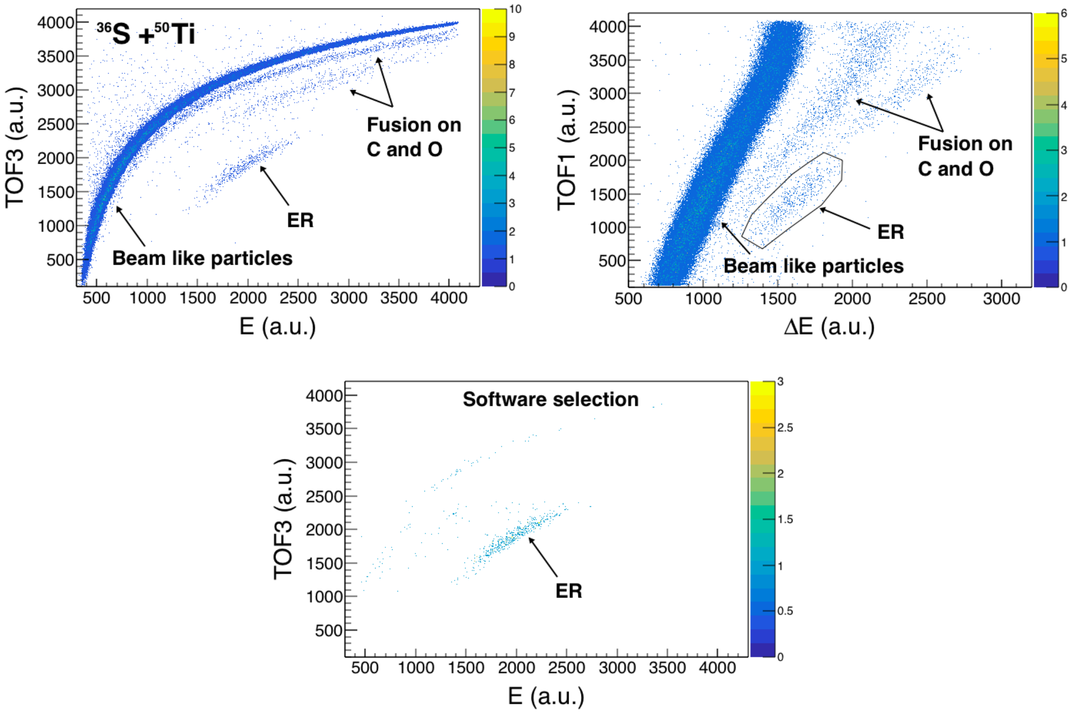

FIGURE 6.4: (Upper left panel) Time of flight $TOF_3$ as a function of the residual energy $E$ for the system $^{36}S + ^{50}Ti$ at the beam energy of 78 MeV, that is, below the barrier. (Bottom panel) The same matrix after a software selection of the ER identified in the $TOF_1$ vs ΔE matrix (upper right panel). Because of the longer acquisition time necessary for sub-barrier fusion measurements, the fusion of the beam on carbon and oxygen is more visible than in the case of the higher energies (see Fig. 6.2))

Figure 6.3 shows the plots $TOF_{1,2,3}$ vs. residual energy (on the left) and $TOF_{1,2,3}$ vs. $\Delta E$ (on the right) for the system $^{36}S + ^{51}V$. At the highest measured energy (100 MeV) the ER are well separated from the degraded beam. Unlike the case of $^{36}S + ^{50}Ti$, the fusion on the carbon and oxygen of the target are hardly visible because: *i*) the target is metallic and *ii*) the acquisition time for those measurements was shorter.

The relative contribution of fusion on the carbon backing of the target and on the oxygen (which was not a component of the target but was originated from its oxydation) increases at sub-barrier energies and is clearly visible (energies below 78 MeV, see Fig. 6.5). As shown in Fig. 6.3 (left panels), a fraction of the ER were produced following alpha particles emission. Also for this system this fraction (overestimated by the *PACE*4 calculations by 81% and 56% at energies above and below the barrier, respectively) decreases with decreasing beam energy and becomes negligible at sub-barrier energies.

When the energy drops below the barrier, the ratio of ER to background events decreases rapidly. The identification of ER becomes therefore more difficult and it is necessary to apply software conditions in order to remove the background. The adopted method is based on identifying the ER by using the various independent parameters (two TOF, ΔE and E) that are measured. Figure 6.4 presents the plot of the time of flight $TOF_3$ as a function of the residual energy $E$ before (upper left panel) and after (bottom panel) the selection of the ER identified in the $TOF_1$ vs ΔE (upper right panel) for the $^{36}S + ^{50}Ti$ system. The same type of matrices obtained for the

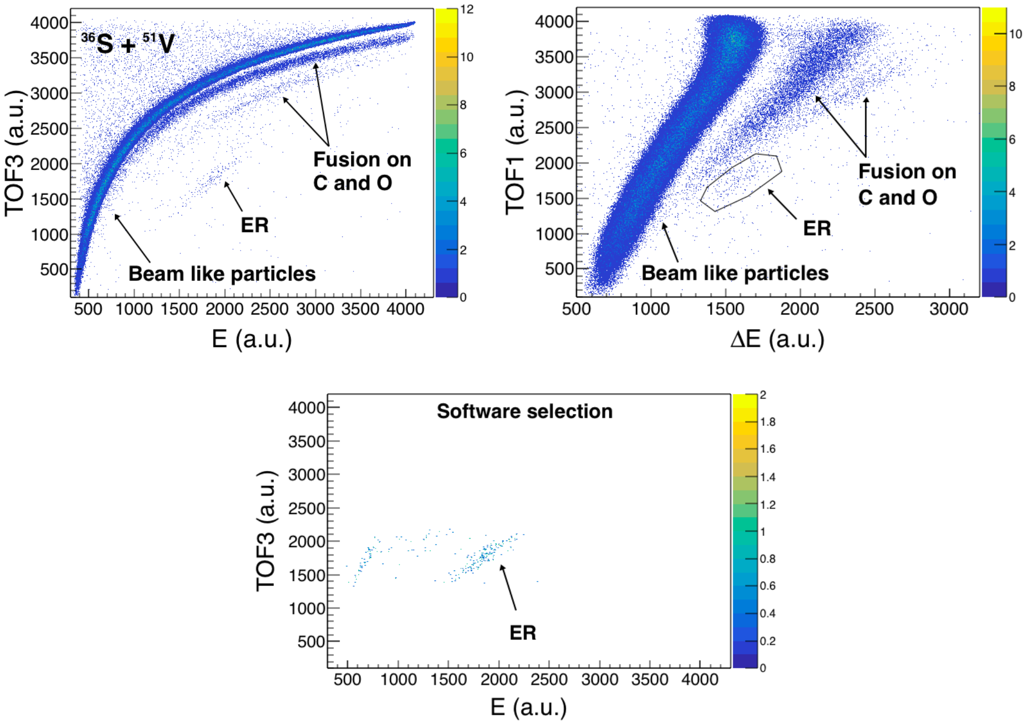

FIGURE 6.5: (Upper left panel) Time of flight $TOF_3$ as a function of the residual energy $E$ for the system $^{36}S + ^{51}V$ at the beam energy of 78 MeV. (Bottom panel) The same matrix after a software selection of the ER identified in the $TOF_1$ vs ΔE matrix (upper right panel). Because of the longer acquisition time necessary for sub-barrier fusion measurements, the fusion on carbon and oxygen of the target are more visible than in the case of the higher energies (see Fig. 6.3)

$^{36}S + ^{51}V$ reaction are shown in Fig. 6.5. The beam energy for these two measurements was 78 MeV, which is in the sub-barrier energy region for both systems. The use of the selection allows to identify the ER more clearly.

At deeper sub-barrier energies, a further software selection was necessary in order to separate the ER from the background. A selection on the matrices $TOF_2$ vs $E$ was therefore performed. However, unlike the case of higher energies, the ER were not clearly identified in the matrices used for the software selection. Therefore, the gates for the selection were wide and their positions were chosen according to the situation observed at higher energies, where the ER were still clearly visible. By applying both these conditions the ER are clearly identified (see Fig.6.6, lower left panel), and the background is considerably reduced.

The matrices resulting from this additional selection for the $^{36}S + ^{50}Ti$ system are shown in Fig. 6.6, where the beam energy was 75 MeV. On the contrary, the ER are not distinguishable from the background for the $^{36}S + ^{51}V$ system, as shown in Fig. 6.7 (upper left panel). The energy was 76 MeV, which is the lowest energy used for this system. However, the use of a selection on the two matrices $TOF_1$ vs ΔE and $TOF_2$ vs E allows to identify the few ER which were produced.

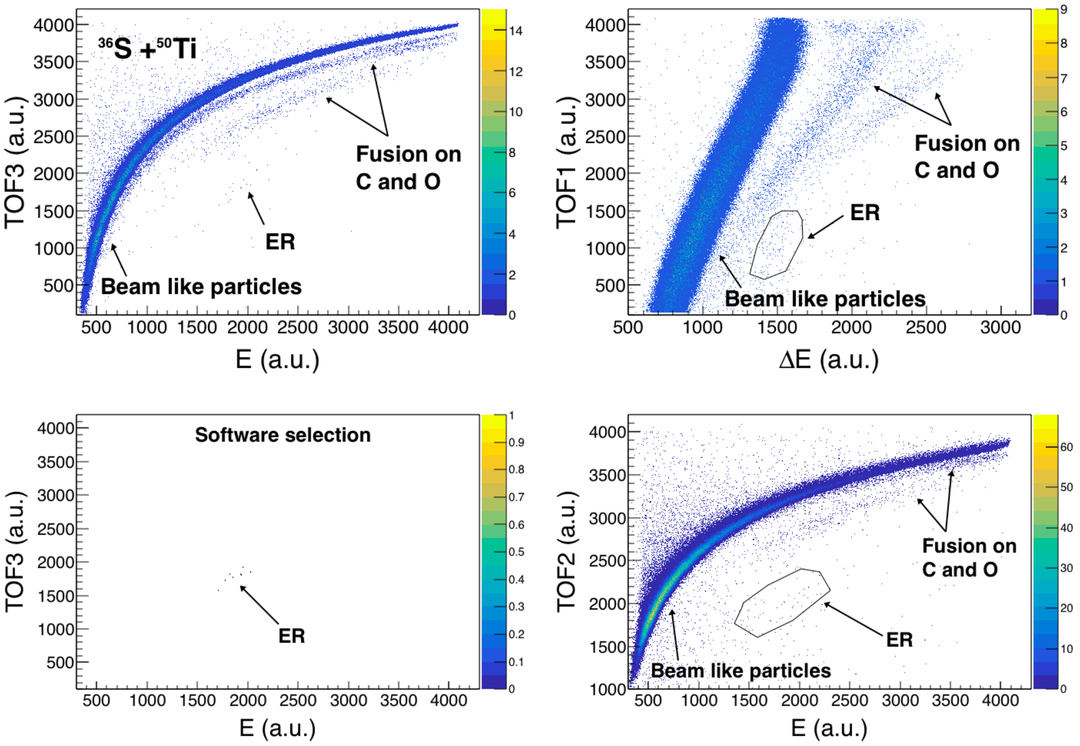

FIGURE 6.6: (Upper left panel) Time of flight $TOF_3$ as a function of the residual energy $E$ for the system $^{36}S + ^{50}Ti$ at the beam energy of 75 MeV. (Bottom left panel) The same matrix after a software selection of the ER identified in the matrices $TOF_2$ vs E (bottom right panel) and $TOF_1$ vs ΔE (upper right panel).

### 6.3.1 Excitation function and barrier distribution

The four silicon detectors placed inside the reaction chamber detected the beam nuclei which scattered on the target, at an angle of 16.05° with respect to the beam direction. Examples of 1D spectra provided by the four monitors at the maximum measured energy of 100 MeV are shown in the Figures 6.8 and 6.9 for the $^{36}S + ^{50}Ti$ and $^{36}S + ^{51}V$ systems, respectively. As shown in the figures, also the beam nuclei that scattered on the carbon backing of the targets and on oxygen (in the case of the titanium target) are visible. The overall statistics of the nuclei of the scattered beam nuclei on the targets in each monitor allows to control the beam centering during the experiment and to estimate the Rutherford scattering cross section, which is used to normalize the fusion cross section.

The normalization is very important since the beam parameters do not remain constant but tend to fluctuate, especially during the sub-barrier energy measurements, when the acquisition time is very long (several hours). This normalization allows to take into account and correct for the variations of beam conditions.
The Rutherford cross section is given by the following formula:

$$\frac{d\sigma_{Ruth}}{d\Omega_{lab}}(E,\theta_{lab}) = \left(\frac{Z_p Z_t e^2}{16\pi\epsilon_0 E_{Lab}}\right)^2 \left(\frac{1}{sin^4(\theta_{lab}/2)} - 2\left(\frac{M_p}{M_t}\right)^2 + ...\right) \tag{6.1}$$

where $Z_p$ and $Z_t$ are the atomic numbers of the projectile and target nuclei, respectively and $\theta_{lab}$ is the angle where the monitors are placed with respect to the

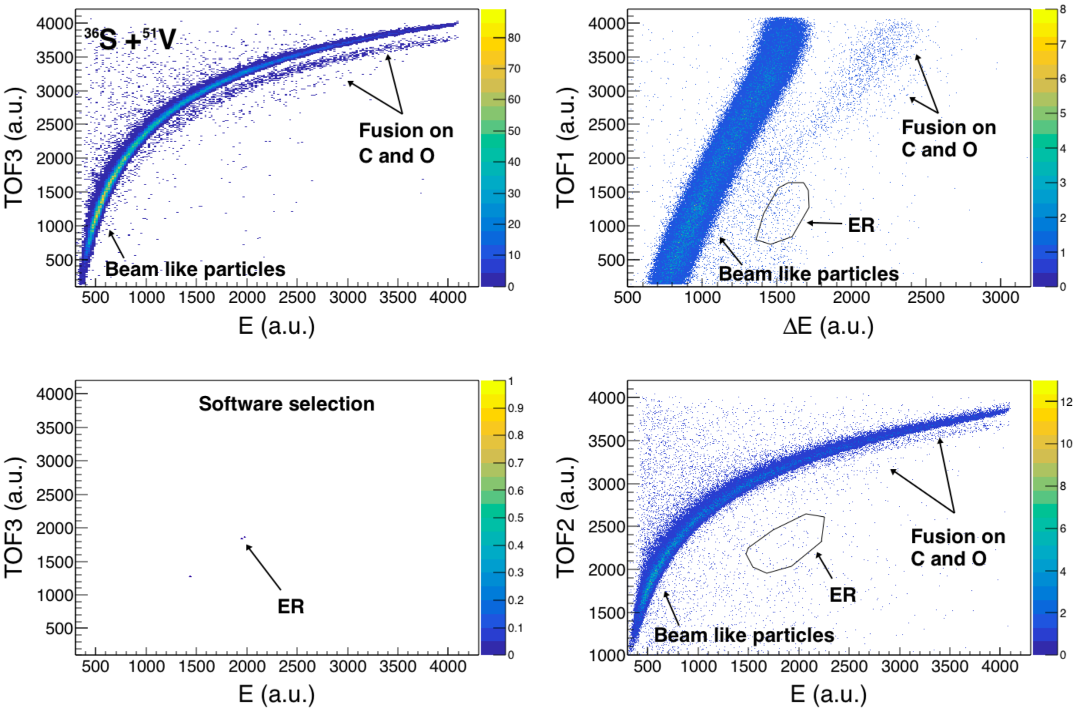

FIGURE 6.7: (Upper left panel) Time of flight TOF$_3$ as a function of the residual energy $E$ for the system $^{36}$S + $^{51}$V at the beam energy of 75 MeV. (Bottom left panel) The same matrix after a software selection of the ER identified in the matrices TOF$_2$ vs E (bottom right panel) and TOF$_1$ vs ΔE (upper right panel).

beam line. $M_p$ and $M_t$ are the projectile and target masses. Terms of higher order ($\propto (M_p/M_t)^4$) are negiglible in direct kinematics reactions.

Once the ER and monitors counts have been measured, it is possible to obtain the differential fusion cross section for each energy using the following formula:

$$\frac{d\sigma^{ER}}{d\Omega}(E,\theta_{ER}) = \frac{d\sigma_{Ruth}}{d\Omega_{lab}}(E,\theta_{lab})\frac{N^{ER}}{N^{Mon}}\frac{\Delta\Omega^{Mon}}{\Delta\Omega^{ER}}\frac{1}{\epsilon} \tag{6.2}$$

Here, $N^{Mon}$ is the number of elastic scattering events detected by the monitors, $\Delta\Omega^{Mon}$ is the total solid angle subtended by them and $\theta_{lab}$ is the monitor angle 16.05°. $N^{ER}$ is the number of ER counted by the silicon detector and $\Delta\Omega^{ER}$ is its solid angle. The quantity $\epsilon$ can be explicitly expressed as the product of:

- the deflector transmission $T$;
- the transparency of the two MCP $t$;
- the transparency of the IC electrodes $(t_e)^{11}$;
- the transparency of the IC entrance window $t_{mesh}$.

These parameters are reported in Table 6.2, together with the values of the solid angles of the four monitors $\Delta\Omega^{Mon}$ and of the silicon detector $\Delta\Omega^{ER}$.

The uncertainty on the measured differential cross section is composed by systematic and statistical contributions. The systematic component affects all measurements in the same way and originates from the uncertainty on the solid angle of the

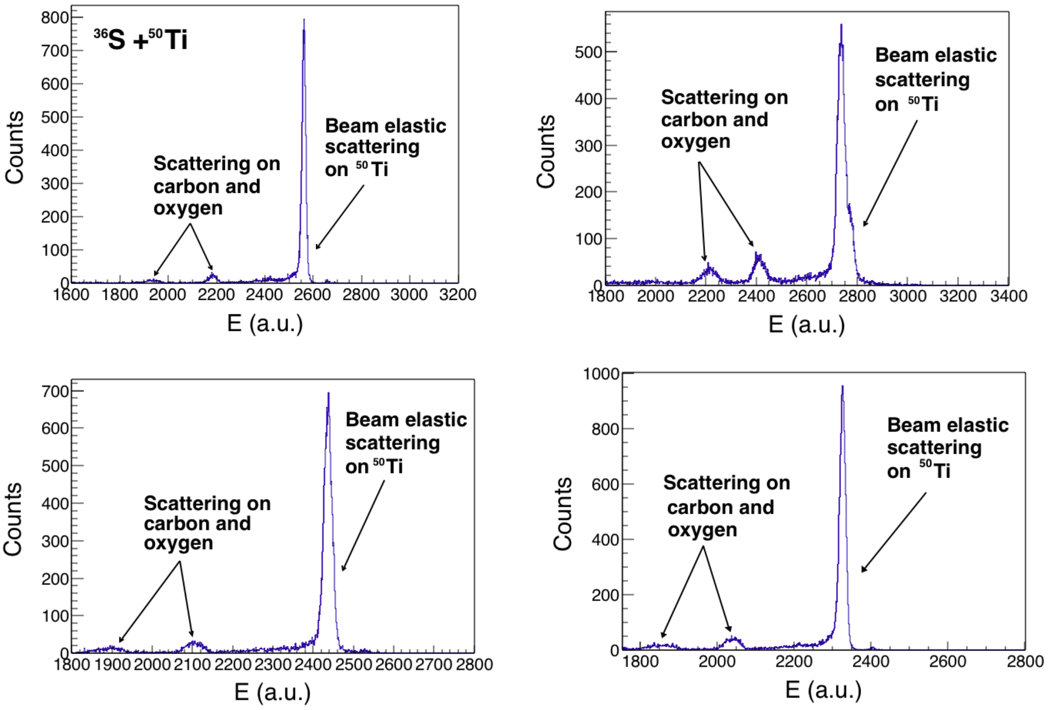

FIGURE 6.8: Energy spectra of the 4 monitors for the $^{36}$S + $^{50}$Ti system at 100 MeV. The peaks of the beam scattering on the titanium, carbon and oxygen of the target are well separated.

detectors, on the transmission of the deflector and on the transparency of the various parts of the telescope. It is given by the following formula:

$$\left(\frac{\epsilon^{syst}_{d\sigma/d\Omega}}{d\sigma/d\Omega}\right)^2 = \left(\frac{\epsilon_{\Delta\Omega_{mon}}}{\Delta\Omega_{mon}}\right)^2 + \left(\frac{\epsilon_{\Delta\Omega_{ER}}}{\Delta\Omega_{ER}}\right)^2 + \left(\frac{\epsilon_T}{T}\right)^2 + \left(\frac{\epsilon_t}{t}\right)^2 + \left(\frac{\epsilon_{t_{mesh}}}{t_{mesh}}\right)^2 + \sum_{i=1}^{N_e}\left(\frac{\epsilon_{t_e}}{t_e}\right)^2_i \tag{6.3}$$

where N$_e$ is the number of electrodes of the IC, which was 11 for this experiment. The expression above gives a value of the order of 5%. The dominant contribution derives from the transmission of the deflector, which was estimated 4% for T = 0.74. Smaller contributions derive from the transparency of the detectors (estimated as the product of the transparencies of the MCP, the window and the electrode grids) and from the solid angles of both the monitors and the silicon detectors (see Table 6.2). The statistical contribution includes the uncertainties on the number of detected events, whose effect on the measurement of the differential cross section can be calculated by the propagation formula:

TABLE 6.2: From left to right: transmission of the deflector, transparencies of the MCP and of the IC window mesh and of one electrode grid, and solid angles of the monitors and of the silicon detector.

| T | t | $t_{mesh}$ | $t_e$ | $\Delta\Omega^{Mon}$ (msr) | $\Delta\Omega^{ER}$ (msr) |
|---|---|---|---|---|---|
| $0.74 \pm 0.03$ | $0.726 \pm 0.004$ | $0.80 \pm 0.01$ | $0.9795 \pm 0.0004$ | $0.167 \pm 0.001$ | $0.0358 \pm 0.0004$ |

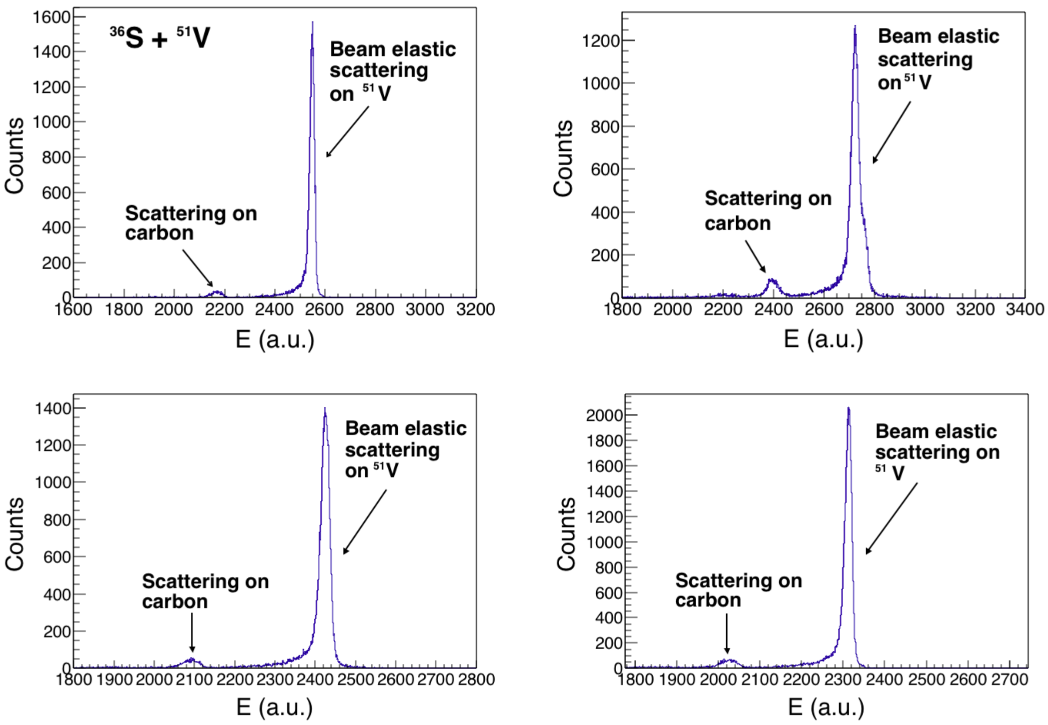

FIGURE 6.9: Energy spectra of the 4 monitors for the $^{36}$S + $^{51}$V system at 100 MeV. The peaks of the beam scattering on vanadium and carbon are well separated.

$$\left(\frac{\epsilon^{stat}_{d\sigma/d\Omega}}{d\sigma/d\Omega}\right)^2 = \left(\frac{\epsilon_{N_{mon}}}{N_{mon}}\right)^2 + \left(\frac{\epsilon_{N_{ER}}}{N_{ER}}\right)^2 \tag{6.4}$$

The statistical component is much lower or comparable to the systematic one, at energies above or near the barrier, but it becomes predominant as energy decreases. This effect is related to drastic reduction of the number N of detected ER at energies below the Coulomb barrier which leads to a rapid increase of the statistical uncertainty (the distribution of the particles' counts is Poissonian so that the associated uncertainty is $\sqrt{N}$).

As mentioned before, for both systems, two ER angular distributions were measured at the beam energies of 80 and 90 MeV by varying the detection angle from -6 ° to +9° at steps of 1°. Figures 6.10 and 6.11 show the angular distributions measured at the two energies and for the two systems.
The distribution of the evaporation residues is forward peaked, no run was performed at 0° because of the large background produced by the residual beam which makes the ER identification difficult.
As shown in Fig. 6.10 and Fig. 6.11, the angular distributions follow a Gaussian trend, whose parameters can be estimated by interpolating the experimental data with the function:

$$\frac{d\sigma_{fus}}{d\Omega}(E,\theta) = Ae^{\frac{-\theta^2}{B^2}} \tag{6.5}$$

the fitting parameters $A$ and $B$ are reported in the appendix A.1.1 (Tables A.2 and A.4) and E is the energy at which the angular distribution was measured.

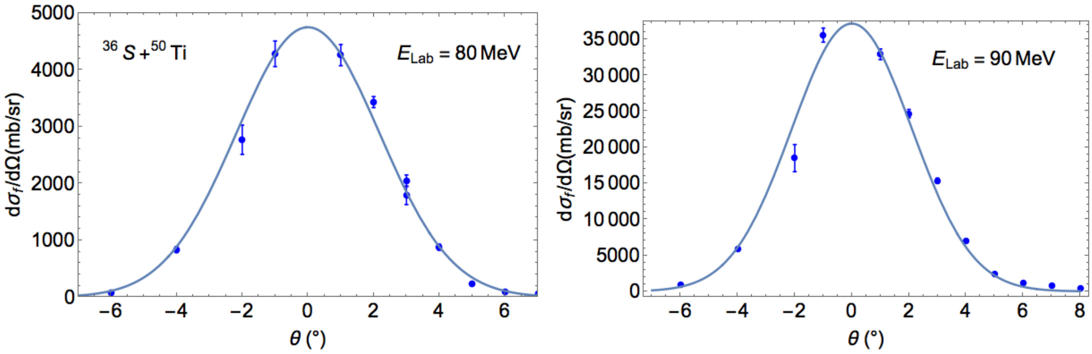

FIGURE 6.10: ER angular distribution for the $^{36}$S + $^{50}$Ti system measured at 80 MeV (left panel) and 90 MeV (right panel). The parameters of the Gaussian fit (blue line) are reported in Table A.2 (Appendix A.1.1).

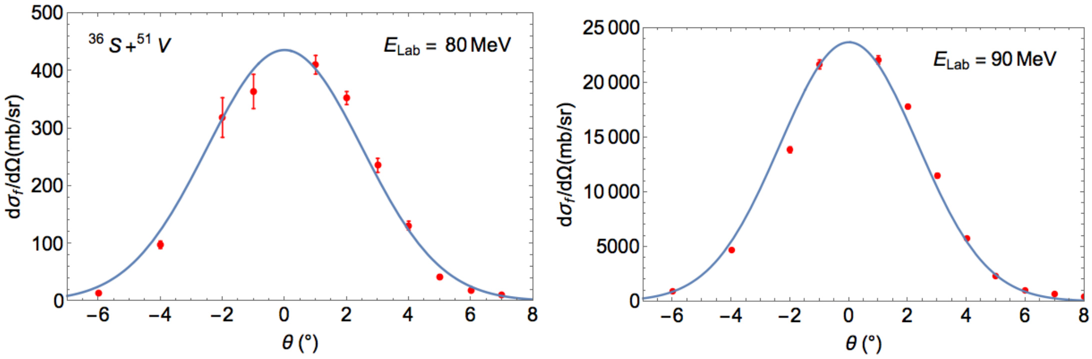

FIGURE 6.11: ER angular distribution for the $^{36}$S + $^{51}$V system at 80 MeV (left panel) and 90 MeV (right panel). The parameters of the Gaussian fit (blue line) are reported in Table A.4 (Appendix A.1.1).

The total fusion cross sections were obtained by integrating those distributions over the entire solid angle.

$$\sigma_{fus}(E) = \int \frac{d\sigma_{fus}}{d\Omega}(E,\theta)d\Omega \tag{6.6}$$

The total fusion cross section at all energies other than 80 or 90 MeV, where only measurements at 2° were performed, were obtained by the use of a simple proportion:

$$\sigma_{fus}(E) = K(E)\frac{d\sigma_{fus}}{d\Omega}(E,\theta) \tag{6.7}$$

where $d\sigma_{fus}/d\Omega(E,\theta)$ is the differential fusion cross section (Eq. 6.5) at the energy $E$ and the detection angle $\theta$ (which is 2° for all the measurements performed at different energies). The parameter K(E) is a quantity weakly dependent on the energy in the measured range. For each system this parameter has been extracted at the two energies where the angular distribution was measured and the obtained values are reported in the appendix A.1.1 (Tables A.2 and A.4).

From the weighted average of these values it was possible to obtain the total fusion cross section at all measured energies, whose values for the two systems are

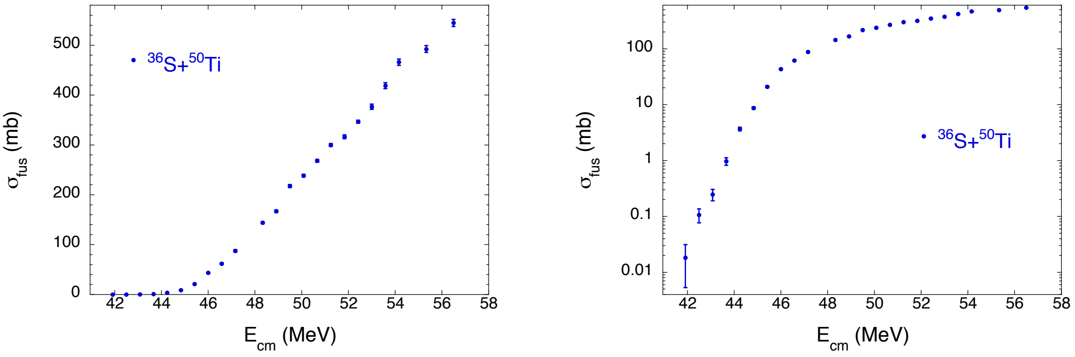

FIGURE 6.12: Excitation function of the system $^{36}$S + $^{50}$Ti in linear (left panel) and logarithmic (right panel) scale.

shown in Table A.5 of the appendix A.1.2.

Figures 6.12 and 6.13 show the excitation functions (fusion cross section as a function of the energy in the center of mass system) in linear (left panels) and logarithmic (right panels) scale for the two systems.

The cross sections vary by five orders of magnitude in the measured energy range. The error bars shown in Figs. 6.12 and 6.13 correspond only to the statistical uncertainty, that is, 1-2% at high energies and 20-30% at sub-barrier energies.

The excitation functions of the two systems are compared in Fig. 6.14, where the cross sections are shown in a reduced energy scale taking into account that the two reactions have Coulomb barriers which differ by few MeV. This comparison highlights a very similar behaviour of the two systems. In order to put in evidence possible small differences, the comparison of the barrier distributions is necessary.

Extracting barrier distribution from the experimental data has proved to be an excellent method to evidence structure effects in the fusion processes, especially at energies around and below the Coulomb barrier.

According to the definition given in Eq. 2.85, the barrier distribution $D_{fus}$ (E) can be expressed as

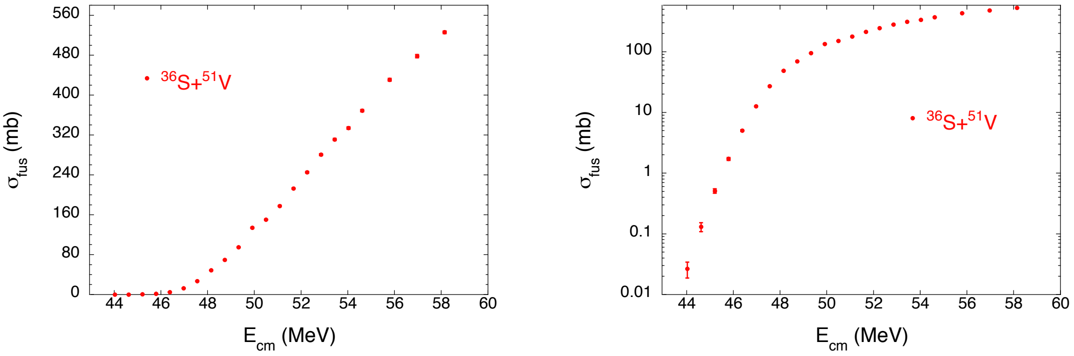

FIGURE 6.13: Excitation function of the system $^{36}$S + $^{51}$V in linear (left panel) and logarithmic (right panel) scale.

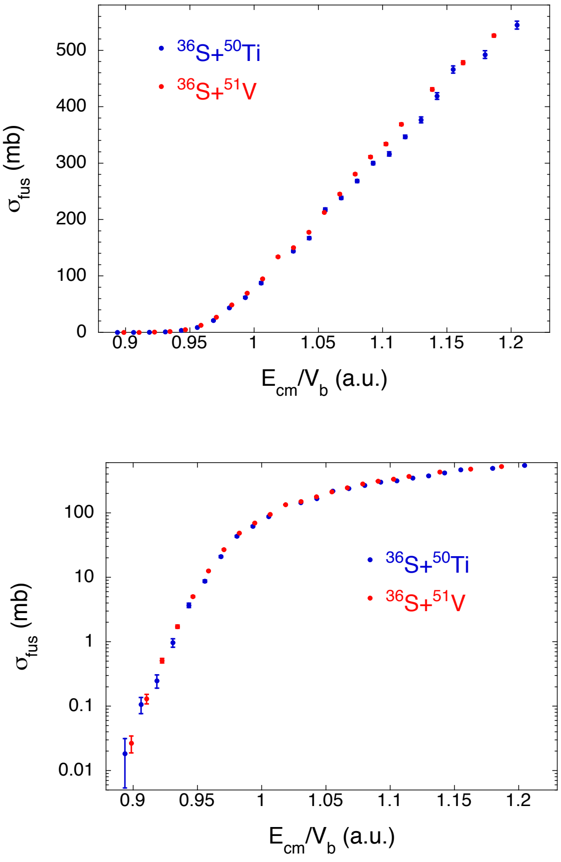

FIGURE 6.14: Comparison of the excitation functions in linear (top panel) and logarithmic (bottom panel) scale for the two fusion reactions. The measurements for the $^{36}S + ^{50}Ti$ and $^{36}S + ^{51}V$ systems are shown with blue and red points, respectively. The energy was normalized with respect to the height $V_b$ of the two Coulomb barriers.

$$D_{fus}(E) = \frac{1}{\pi R^2} \frac{d^2(E\sigma_{fus})}{dE^2} \tag{6.8}$$

As discussed in section 2.3, given the finite nature of the measured fusion cross sections, obtaining the barrier distribution from the experimental data can not be performed analytically. To overcome this problem, the barrier distribution can be obtained using incremental ratios, where the derivative of the energy-weighted cross sections can be calculated using the point-difference formula. It is as well possible to obtain the second derivative considering three values of the cross section $\sigma_{1,2,3}$ measured at consecutive energies $E_{1,2,3}$ (three-points formula), so that the second derivative relative to the average energy ( $E_1$ + 2$E_2$ + $E_3$)/4 is expressed as:

$$\frac{d^2(E\sigma_{fus})}{dE^2} \simeq 2\left(\frac{E_3\sigma_3 - E_2\sigma_2}{E_3 - E_2} - \frac{E_2\sigma_2 - E_1\sigma_1}{E_2 - E_1}\right)\left(\frac{1}{E_3 - E_1}\right) \simeq (\frac{E_3\sigma_3 - 2E_2\sigma_2 + E_1\sigma_1}{\Delta E^2}) \tag{6.9}$$

where the second expresion is obtained assuming equal energy steps for the three

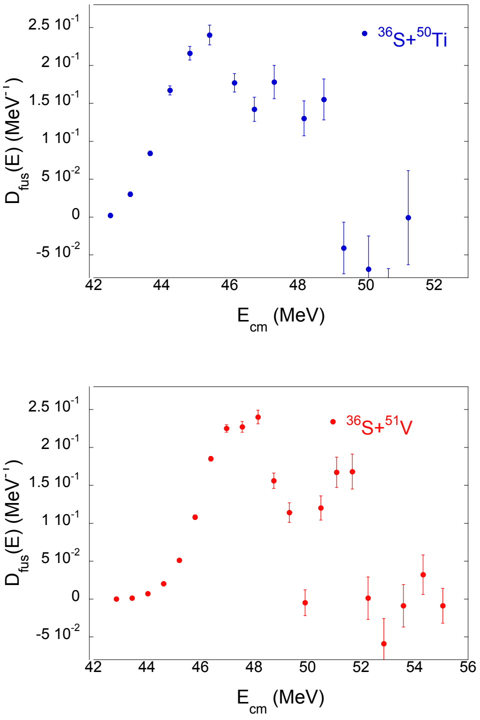

FIGURE 6.15: Fusion barrier distributions of $^{36}\mathrm{S} + {}^{50}\mathrm{Ti}$ (on the top) and $^{36}\mathrm{S} + {}^{51}\mathrm{V}$ (on the bottom).

measurements. The statistical uncertainty associated with the second derivative is estimated as the quadratic propagation of the absolute statistical uncertainties of the cross sections:

$$\delta_c = \left(\frac{E}{\Delta E^2}\right)[(\delta\sigma)_1^2 + 4(\delta\sigma)_2^2 + (\delta\sigma)_3^2]^{\frac{1}{2}} \tag{6.10}$$

The values obtained in this way are shown in Table A.6 of the appendix A.1.3.

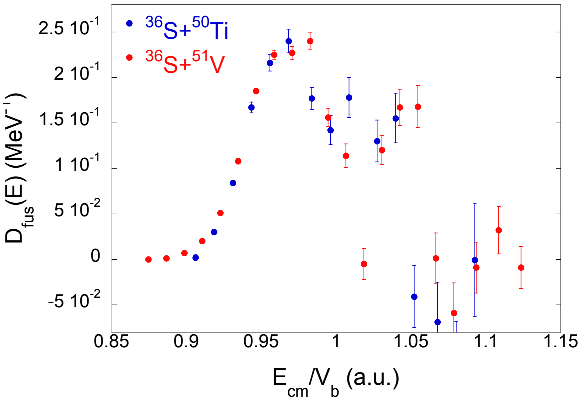

FIGURE 6.16: Comparison of the two barrier distributions, shown separately in Fig. 6.15.

Energy intervals of $\sim 1.5$ MeV have been used to extract the barrier distributions and to make visible the structures at energies above and below the barrier. As discussed in chapter 2.3, this choice of energy intervals allows to reach a good compromise between the sensitivity and the precision of the values obtained for the barrier distributions.

The barrier distributions obtained for the two systems are plotted vs. the energy in the center of mass system in Fig. 6.15. The shapes of the two distributions are extremely similar. This is more evident in figure 6.16 where the two barrier distributions are compared by using a reduced energy scale (energy in the center of mass devided by the height of the Coulomb barrier $V_b$).

It appears that to correctly undestand the experimental results, a theoretical interpretation is necessary. In this perspective a coupled-channels analysis was performed using a modified version of the CCFULL code, able to consider nuclei with non-zero spin in the ground state.

### 6.3.2 Coupled channel analysis

The experimental data of the two fusion reactions have been compared to the theoretical calculations based on the coupled-channels model. The comparison is of great importance not only from a structural point of view, in order to verify the excited states involved in the fusion dynamics, but also to evidence possible small differences between the two reactions not observed in the comparison of experimental data and that would be attributable to the odd nature of $^{51}$V. For both systems the CC calculations were performed by means of the CCFULL code [26], which solves the coupled equations by employing the isocentrifugal approximation and the incoming wave boundary condition, described in Chapter 2.2 in details.

For the $^{36}$S+$^{50}$Ti reaction, the energies of the excited states of both target and projectile nuclei, as well as the associated deformation parameters, are given in Table 6.3 [78, 79]. The deformation parameters for each state were calculated using the Eq. 2.57 ( Chapter 2) starting from the reduced transition probabilities B(E2) and B(E3) which have been obtained from the literature [80, 81].
The CC calculations included the collective vibrational excitations of both target and projectile nuclei. In particular, the one-phonon excitation of both the lowest quadrupole vibration state $2^+$ at 1.554 MeV of $^{50}$Ti and the first $2^+$ state at 3.29 MeV in $^{36}$S, were considered.

By employing in the calculations the Akyüz-Winter (AW) potential, whose parameters are reported in Table 6.1 (a), the resulting fusion cross sections underestimate the experimental data, as shown in Fig. 6.17 (left panel). This effect may be caused, at least partially, by the adiabatic coupling to high-energy states [8]. In order to correct for this effect, the well depth of the AW potential has been modified to

TABLE 6.3: Nuclear structure parameters of CCFULL calculations. The $\beta_\lambda$ is the deformation parameter of the various vibrational modes.

| Nucleus | E(MeV) | $\lambda^\pi$ | $\beta_\lambda$ |
|---|---|---|---|
| $^{50}$T | 1.55 | $2^+$ | 0.166 |
|  | 4.41 | $3^-$ | 0.138 |
|  | 2.68 | $4^+$ | 0.050 |
| $^{36}$S | 3.29 | $2^+$ | 0.167 |

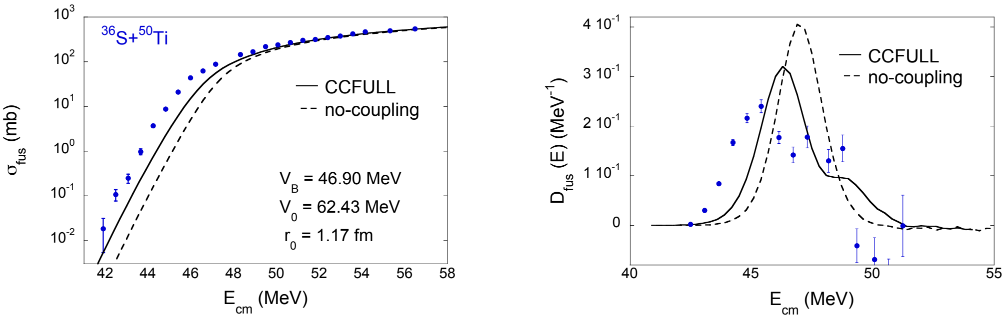

FIGURE 6.17: (Left) Experimental excitation function (blue points) compared to the theoretical prediction based on the coupled channel calculations involving the $2^+$ excited states of the $^{50}$Ti and $^{36}$S nuclei (black line) and no-coupling limit (black dashed line). (Right) The barrier distributions extracted from the experimental data and from the CC calculations (with and without the coupling to excited states). The AW potential was used.

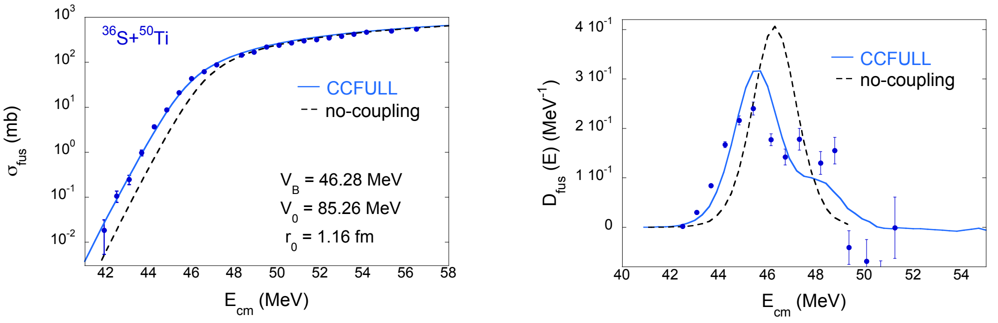

FIGURE 6.18: (Left) Experimental excitation function (blue points) compared to the theoretical prediction based on the CC calculations involving the coupling of the $2^+$ excited states of the $^{50}$Ti and $^{36}$S nuclei (blue line) and without any coupling (black dashed line). (Right) The barrier distributions extracted from the experimental data and from the CC calculations (with and without couplings to the excited states). A modified Woods-Saxon potential was used (see text).

$V_0 = 85.26$ MeV. Following this renormalization, the barrier is $V_B = 46.28$ MeV and the radius parameter $r_0$ is 1.16 fm. The diffuseness $a$ was kept to 0.66 MeV. The resulting CC calculation is shown in Fig. 6.18. The couplings lead to a large enhancement of the fusion below the barrier and well reproduce the experimental data at energies both below and above the Coulomb barrier.

The calculated barrier distribution is reported in Fig. 6.17 (right panel) and shows a trend very similar to the experimental one. In particular a very good fit to the $^{36}S + ^{50}Ti$ data can be obtained by using a nuclear deformation parameter $\beta_N = 0.2$, slightly larger than the Coulomb one $\beta_C = 0.166$ (reported in Table 6.3).

Coupled channels calculations which include additionally the $3^-$ octupole state of the $^{50}$Ti at 4.41 MeV as well as the lower weak $4^+$ overstimate the experimental

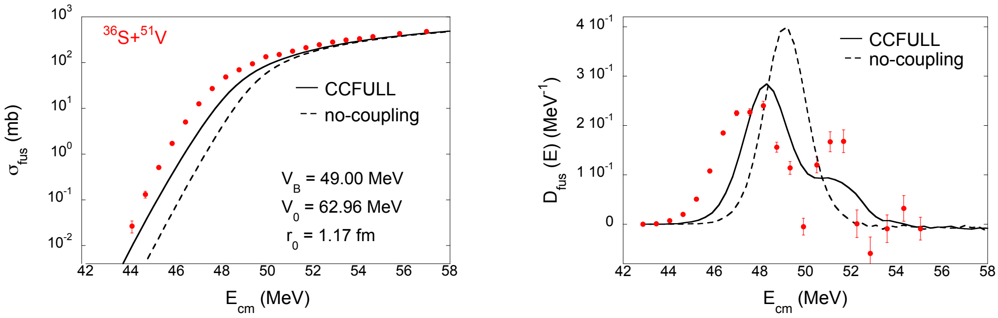

FIGURE 6.19: (Left) Experimental excitation function (red points) compared to the theoretical prediction based on the CC calculations involving couplings of the $2^+$ excited states of the $^{51}$V and $^{36}$S nuclei (black line) and without any couplings (black dashed line). (Right) The barrier distributions extracted from the experimental data and from the CC calculations (with and without the couplings to excited states). The AW potential was used.

data at sub-barrier energies since their couplings are already included in the renormalized potential.

In the case of $^{36}$S+$^{51}$V, the calculations are more complex and tedious because of the non-zero ground-state spin $I = 7/2^-$ of $^{51}$V. The shell-model structure of the nucleus $^{51}$V is relatively simple, consisting of a proton in the $f_{7/2}$ shell added to $^{50}$Ti or of a proton-hole in $^{52}$Cr [82]. For simplicity, this last configuration has been adopted in the following calculations. The five low-lying odd-parity excited states considered in the calculations are reported in Table 6.4.

In the rotating frame approximation, where the $m$ quantum number stays fixed and equal to the value in the initial state, the calculations have to be repeated for each value of $m$. Actually, it was sufficient to perform the calculations for $m = 1/2, 3/2, 5/2$ and $7/2$, for symmetry reasons.

A total of eight couplings have been included in the calculations, according to the transitions among the states in $^{51}$V which are well known experimentally [83] and whose reduced transition probabilities are reported in Table 6.5. The deformation parameters have been calculated for each coupling between the $i$-th and the $j$-th channel and are shown in the same Table 6.5. In order to establish the sign of the deformation parameter, the weak-coupling approximation was used (see Appendix A.2). For the coupled-channels calculation a modified code of CCFULL was employed. This program evaluates the fusion cross section for each m-substate and

TABLE 6.4: Spin and energy of the ground state and excited states of $^{51}$V. The levels are numbered with the notation on the left.

| Level | Spin $I$ | E (MeV) |
|---|---|---|
| 1 | $7/2^-$ (g.s.) | 0 |
| 2 | $5/2^-$ | 0.32 |
| 3 | $3/2^-$ | 0.93 |
| 4 | $11/2^-$ | 1.61 |
| 5 | $9/2^-$ | 1.81 |
| 6 | $3/2^-$ | 2.41 |

TABLE 6.5: The eight couplings of the excited states of $^{51}$V. For each of them, the quadrupole transition probability and the deformation parameters are given.

| Level Coupling | Spin $I$ | B(E2) (W.u.) | $\beta$ |
|---|---|---|---|
| 1 - 2 | $5/2^- \rightarrow 7/2^-$ | 14.5 | |
| | $\pm 1/2$ | | + 0.06 |
| | $\pm 3/2$ | | + 0.165 |
| | $\pm 5/2$ | | + 0.21 |
| 2 - 3 | $3/2^- \rightarrow 5/2^-$ | 10.0 | |
| | $\pm 1/2$ | | - 0.069 |
| | $\pm 3/2$ | | - 0.169 |
| 1 - 3 | $3/2^- \rightarrow 7/2^-$ | 7.6 | |
| | $\pm 1/2$ | | + 0.1.27 |
| | $\pm 3/2$ | | + 0.095 |
| 1 - 4 | $11/2^- \rightarrow 7/2^-$ | 8.5 | |
| | $\pm 1/2$ | | + 0.188 |
| | $\pm 3/2$ | | + 0.172 |
| | $\pm 5/2$ | | + 0.140 |
| | $\pm 7/2$ | | + 0.0919 |
| 1 - 5 | $9/2^- \rightarrow 7/2^-$ | 3.1 | |
| | $\pm 1/2$ | | - 0.0246 |
| | $\pm 3/2$ | | - 0.07 |
| | $\pm 5/2$ | | - 0.103 |
| | $\pm 7/2$ | | - 0.109 |
| 2 - 5 | $9/2^- \rightarrow 5/2^-$ | 2.8 | |
| | $\pm 1/2$ | | + 0.110 |
| | $\pm 3/2$ | | + 0.095 |
| | $\pm 5/2$ | | + 0.0649 |
| 2 - 6 | $3/2^- \rightarrow 5/2^-$ | 7 | |
| | $\pm 1/2$ | | - 0.0577 |
| | $\pm 3/2$ | | - 0.141 |
| 1 - 6 | $3/2^- \rightarrow 7/2^-$ | 8.6 | |
| | $\pm 1/2$ | | + 0.136 |
| | $\pm 3/2$ | | + 0.101 |

provides their average as output. The performed CC calculations included the vibration coupling of all six excited states of $^{51}$V with the $2^+$ state of the projectile nuclei $^{36}$S and all the mutual excitations. As in the case of the $^{36}$S+$^{50}$Ti, using the AW potential parameters (reported in Table 6.1) leads to an underestimation of the fusion cross section at energies below the Coulomb barrier, as shown in Fig. 6.19 (left panel). Also in this reaction the AW potential generates a barrier which is higher than the experimental evidence. Following a renormalization of the AW potential to obtain a barrier $V_B = 48.39$ MeV, the potential well becomes $V_0 = 85.26$ MeV.

Figure 6.20 (left panel) reports the performed CC calculation employing the renormalized potential. The couplings (red line) enhance the fusion cross section below the barrier with respect of the no-coupling predictions (dashed black line) and a good agreement with the experimental excitation function is obtained. The experimental barrier distribution (Fig. 6.20 right panel) is well predicted by the CC calculation at lower energies, where the main peak is well reproduced.

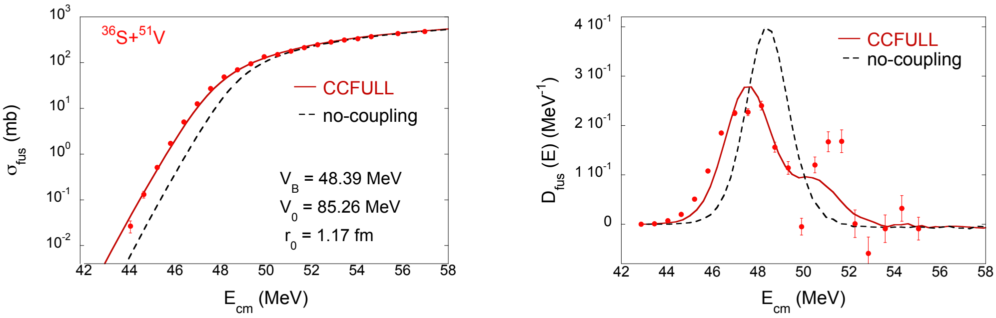

FIGURE 6.20: (Left) Experimental excitation function (red points) compared to the theoretical prediction based on the CC calculations involving couplings of the excited states of the $^{51}$V and $^{36}$S nuclei (red line) and without any couplings (black dashed line). (Right) The barrier distributions extracted from the experimental data and from CC calculations (with and without the couplings to the excited states). A modified WS potential was used (see text).

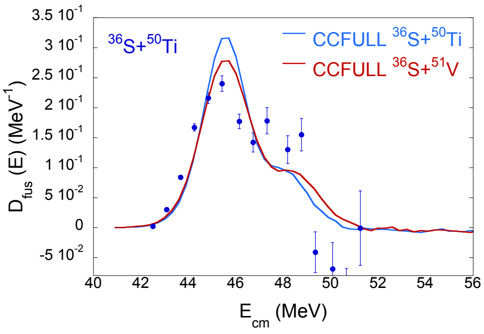

FIGURE 6.21: The experimental barrier distribution of the system $^{36}$S+$^{50}$Ti compared to the calculated barrier distribution for the same system (blue line) and for $^{36}$S+$^{51}$V (red line).

The CC calculations performed for both fusion reactions are in very good agreement with the experimental data and reproduce the fusion cross section at energies much below the Coulomb barrier (see left panel of Fig. 6.18 and 6.20). Despite the different target nuclei involved and the different couplings of the excited states, the calculated barrier distributions show a very similar behavior. This is clearly observed in Fig. 6.21, where the experimental barrier distribution of the $^{36}$S+$^{50}$Ti system (blue points) is compared with the CC calculations obtained for the two systems. Both theoretical predictions well reproduce the peak at low energies, whereas they slightly differ at higher energies where the shoulder is more evident in the $^{36}$S+$^{51}$V system (red line). Unfortunaly, the lack of accurate experimental data in this energy region does not allow to confirm the different trend between the two systems.

## 6.4 Conclusion

Sub-barrier fusion of the two systems $^{36}$S+$^{50}$Ti,$^{51}$V has been measured at the Laboratori Nazionali di Legnaro with the purpose of investigating the possible effect of the non-zero spin of the $^{51}$V ground state on the sub-barrier excitation function, and in particular on the shape of the barrier distribution.

The fusion cross sections of two systems vary by five orders of magnitude in the energy range measured down to values $\sim$20 $\mu$b. The two excitation functions look very similar, as shown in Fig. 6.14.
A coupled channels analysis was therefore performed in order to highlight differences between the two systems attributable to the non-zero spin ground state of $^{51}$V. In the case of the $^{36}$S+$^{50}$Ti system the CCFULL code was used and the calculations included the couplings of the $2^+$ vibrational states of both projectile and target. For the $^{36}$S+$^{51}$V reaction the CCFULL code has been modified in order to include the $^{51}$V excitations. In these calculations the $2^+$ excitation in $^{36}$S was considered as well as the couplings to the $5/2^-$, $3/2^-$, $11/2^-$, $9/2^-$, and $3/2^-$ states in $^{51}$V. In both cases the Akyüz-Winther potential was renormalized in order to shift the barrier to lower energies. The theoretical predictions obtained in this way are in very good agreement with the experimental excitation functions of both systems at energies above and below the Coulomb barrier (see Figs. 6.18 and 6.20).

Also the barrier distribution for $^{36}$S+$^{50}$Ti looks very similar to the barrier distribution for $^{36}$S+$^{51}$V (as shown in Fig. 6.16 and Fig. 6.21). This would indicate that the extra proton in the $1f_{7/2}$ shell does not have any significant influence on sub-barrier fusion behaviour. A small difference between the two barrier distributions is calculated around 51–52 MeV (see Fig. 6.21) but the accuracy of the data in that energy region is not sufficient to confirm this evidence, and it would not be easy to have more precise data for fusion barrier distribution in that region above the barrier. As an alternative, a future measurement of the barrier distribution extracted from backward-angle quasi-elastic scattering may be considered for that energy range [84, 85].

## Chapter 7

# Summary

The availability of the very neutron-rich beams of the SPES facility at relatively low intensities makes very tempting to extend the study of near- and sub-barrier fusion to exotic systems also at the National Laboratories of Legnaro.

A new set-up for fusion cross section measurements, especially designed for the low intensity beams delivered by the SPES facility, has been developed and is being installed at the LNL. The set-up is inspired on a similar one built at Oak Ridge some years ago, with a significant improvement due to the use of a very fast ionization chamber (Fast IC). This new Fast IC is designed to ensure a high counting rate particle identification for fusion studies involving exotic beams up to $10^5$ pps. To reduce the response time of the ionization chamber, a design using 13 tilted electrodes has been adopted. This configuration significantly decreases the drift time of the electrons to anodes with respect to a conventional IC with transverse field, thus enabling ion detection at high counting rates. We expect a maximum counting rate up to 100-200 kHz for the identification of ER.

The set-up already existing at LNL for fusion measurements has been upgraded by using the new Fast IC, and will remain in use for experiments with high-intensity stable (and upcoming exotic) beams. The performance of the Fast IC has been studied in several tests with stable beams. The detector proved to be able to work with a shaping time of 0.25 $\mu$s and a gate width of the DAQ of 1 $\mu$s, which are four times lower than the ones used with the conventional IC. The last modules of the IC can produce a veto signal by adjusting the gas pressure so that only the transmitted beam (and not the ER) reaches the last anode. This veto helps cleaning up the spectra by rejecting the unwanted beam-like events. Under this condition, the detector has been tested up to a rate of $\simeq 140$ kHz. All these tests verified the capability of th IC to provide a fast response. The Z-resolution of the IC has been measured to be 1/38 for $^{64}$Zn ions at about 3 MeV/A. The energy resolution is $\cong 2.1\%$ with $^{64}$Zn ions at the energy of 2.3 MeV/A.

The sub-barrier fusion of the two systems $^{36}$S+$^{50}$Ti,$^{51}$V has been measured with the upgraded set-up. The purpose of the experiment was to investigate the possible effect of the non-zero spin of the $^{51}$V ground state on the sub-barrier excitation function, and in particular on the shape of the barrier distribution.

The fusion cross section has been measured down to $\sim 20\,\mu$b for both systems. The two excitation functions look very similar, as well as the two barrier distributions. A coupled channels analysis was therefore performed in order to highlight differences between the two systems attributable to the $7/2^-$ ground state of $^{51}$V. In the case of the $^{36}$S+$^{50}$Ti the CCFULL code was used and the calculations included the couplings of the $2^+$ vibrational states of both projectile and target. For $^{36}$S+$^{51}$V a modified CCFULL code was used in order to include the $^{51}$V excitations. In these calculations the $2^+$ excitation of $^{36}$S was considered as well as the couplings to the $5/2^-$, $3/2^-$, $11/2^-$, $9/2^-$, and $3/2^-$ excited states in $^{51}$V. The theoretical predictions are in very

good agreement with the experimental excitation functions of both systems at energies above and below the Coulomb barrier.
Also the calculated barrier distributions of $^{36}$S+$^{50}$Ti,$^{51}$V look very similar to each other. A first interpretation of the results is that the extra proton of $^{51}$V ($^{51}$V(I) = $^{50}$Ti $(2^+) \otimes p(1f_{7/2})$) does not have any significant influence on sub-barrier fusion behaviour. In perspective, the small difference between the two barrier distributions calculated above the barrier, might be experimentally checked by measuring the backward-angle quasi-elastic scattering in that energy region.

# Appendix A

# Appendix

## A.1 Fusion cross sections

### A.1.1 Angular distribution

Two ER angular distributions have been measured at 80 MeV and 90 MeV for $^{36}$S+$^{50}$Ti, $^{51}$V. The differential cross sections measured at these two energies for $^{36}$S + $^{50}$Ti are reported in Table A.1. The fitting parameters obtained by reproducing the angular distributions (Fig. 6.10) with a Gaussian function are shown in Table A.2.

TABLE A.1: ER angular distributions obtained for $^{36}$S + $^{50}$Ti at the energies of 80 MeV (a) and 90 MeV (b)

(a) 80 MeV

| $\theta_{lab}$ (deg) | $d\sigma/d\Omega_{lab}$ (mb/sr) |
|---|---|
| - 6 | 76 ± 10 |
| - 4 | 837 ± 52 |
| - 2 | 2770 ± 257 |
| - 1 | 4284 ± 224 |
| 1 | 4260 ± 185 |
| 2 | 3433 ± 96 |
| 3 | 1788 ± 159 |
| 3 | 2053 ± 98 |
| 4 | 877 ± 53 |
| 5 | 240 ± 23 |
| 6 | 97 ± 12 |
| 7 | 61 ± 10 |

(b) 90 MeV

| $\theta_{lab}$ (deg) | $d\sigma/d\Omega_{lab}$ (mb/sr) |
|---|---|
| - 6 | 944 ± 65 |
| - 4 | 5930 ± 190 |
| - 2 | 18482 ± 1880 |
| - 1 | 35532 ± 976 |
| 1 | 32880 ± 735 |
| 2 | 24657 ± 563 |
| 3 | 15342 ± 362 |
| 4 | 6944 ± 177 |
| 5 | 2469 ± 119 |
| 6 | 1129 ± 59 |
| 7 | 780 ± 50 |
| 8 | 463 ± 42 |

TABLE A.2: Fitting parameters of the Gaussian function and the proportional constant K at the energies of the two angular distributions for the system $^{36}$S + $^{50}$Ti.

| E (MeV) | A (mb/sr) | B (sr) | K (sr) |
|---|---|---|---|
| 80 | 4751 ± 135 | 3.1 ± 0.1 | 0.01262 ± 0.00006 |
| 90 | 37129 ± 1642 | 2.9 ± 0.2 | 0.0127 ± 0.0001 |

The differential cross sections measured for $^{36}$S + $^{51}$V are reported in Table A.3. The fitting parameters of these angular distributions are shown in Table A.4.

TABLE A.3: ER angular distributions obtained for $^{36}S + ^{51}V$ at the energies of 80 MeV (a) and 90 MeV (b).

(a) 80 MeV

| $\theta_{lab}$ (deg) | $d\sigma/d\Omega_{lab}$ (mb/sr) |
|---|---|
| -6 | 13 ± 2 |
| -4 | 97 ± 6 |
| -2 | 318 ± 34 |
| -1 | 364 ± 30 |
| 1 | 410 ± 16 |
| 2 | 352 ± 11 |
| 3 | 235 ± 12 |
| 4 | 130 ± 8 |
| 5 | 42 ± 4 |
| 6 | 19 ± 2 |
| 7 | 11 ± 2 |

(b) 90 MeV

| $\theta_{lab}$ (deg) | $d\sigma/d\Omega_{lab}$ (mb/sr) |
|---|---|
| -6 | 917 ± 56 |
| -4 | 4727 ± 83 |
| -2 | 13865 ± 268 |
| -1 | 21679 ± 411 |
| 1 | 22096 ± 380 |
| 2 | 17820 ± 174 |
| 3 | 11491 ± 219 |
| 4 | 5768 ± 63 |
| 5 | 2322 ± 53 |
| 6 | 1039 ± 30 |
| 7 | 651 ± 18 |
| 8 | 433 ± 17 |

TABLE A.4: Fitting parameters of the Gaussian function and the proportional constant K at the energies of the two angular distributions for the system $^{36}S + ^{51}V$.

| E (MeV) | A (mb/sr) | B (sr) | K (sr) |
|---|---|---|---|
| 80 | 435 ± 16 | 3.6 ± 0.1 | 0.0149 ± 0.0001 |
| 90 | 23709 ± 799 | 3.3 ± 0.1 | 0.0139 ± 0.0001 |

### A.1.2 Fusion cross sections

The total fusion cross sections at all measured energies for the two systems are reported in the following Table A.5.

TABLE A.5: Fusion cross sections of the two systems .

(a) $^{36}S + ^{50}Ti$

| $E_{cm}$ (MeV) | $\sigma$ (mb) |
|---|---|
| 41.91 | 0.02 ± 0.01 |
| 42.50 | 0.11 ± 0.03 |
| 43.08 | 0.25 ± 0.06 |
| 43.66 | 0.9 ± 0.1 |
| 44.25 | 3.7 ± 0.3 |
| 44.83 | 8.7 ± 0.4 |
| 45.41 | 20.9 ± 0.7 |
| 46.00 | 43 ± 1 |
| 46.58 | 61 ± 2 |
| 47.16 | 87 ± 2 |
| 48.33 | 143 ± 2 |
| 48.91 | 166 ± 2 |
| 49.50 | 217 ± 3 |
| 50.08 | 238 ± 3 |
| 50.66 | 268 ± 3 |
| 51.25 | 299 ± 3 |
| 51.83 | 316 ± 4 |
| 52.41 | 346 ± 3 |
| 53.00 | 376 ± 5 |
| 53.58 | 418 ± 6 |
| 54.16 | 465 ± 6 |
| 55.33 | 492 ± 7 |
| 56.49 | 544 ± 7 |

(b) $^{36}S + ^{51}V$

| $E_{cm}$ (MeV) | $\sigma$ (mb) |
|---|---|
| 44.03 | 0.027 ± 0.008 |
| 44.62 | 0.13 ± 0.02 |
| 45.21 | 0.51 ± 0.04 |
| 45.79 | 1.7 ± 0.1 |
| 46.38 | 5.0 ± 0.2 |
| 46.97 | 12.6 ± 0.3 |
| 47.56 | 27.0 ± 0.5 |
| 48.15 | 48.6 ± 0.5 |
| 48.73 | 69.4 ± 0.8 |
| 49.32 | 94.8 ± 0.9 |
| 49.91 | 133 ± 1 |
| 50.50 | 150.4 ± 0.9 |
| 51.09 | 177 ± 1 |
| 51.68 | 212 ± 1 |
| 52.26 | 245 ± 2 |
| 52.85 | 280 ± 2 |
| 53.44 | 311 ± 2 |
| 54.03 | 333 ± 2 |
| 54.62 | 368 ± 2 |
| 55.79 | 430 ± 3 |
| 56.97 | 478 ± 3 |
| 58.14 | 525 ± 3 |

### A.1.3 Barrier distributions

The barrier distributions of the two systems are reported in Table A.6

TABLE A.6: Barrier distributions of the two systems.

(a) $^{36}S + ^{50}Ti$

| $E_{cm}$ (MeV) | $D_{fus}$(E) ($MeV^{-1}$) |
|---|---|
| 42.50 | 0.002 ± 0.003 |
| 43.08 | 0.030 ± 0.003 |
| 43.66 | 0.084 ± 0.003 |
| 44.25 | 0.167 ± 0.006 |
| 44.83 | 0.216 ± 0.009 |
| 45.41 | 0.24 ± 0.01 |
| 46.14 | 0.18 ± 0.01 |
| 46.72 | 0.14 ± 0.02 |
| 47.31 | 0.18 ± 0.02 |
| 48.18 | 0.13 ± 0.02 |
| 48.77 | 0.16 ± 0.03 |
| 49.35 | -0.04 ± 0.03 |
| 50.08 | -0.07 ± 0.04 |
| 50.66 | -0.11 ± 0.05 |
| 51.25 | -0.001 ± 0.062 |

(b) $^{36}S + ^{51}V$

| $E_{cm}$ (MeV) | $D_{fus}$(E) ($MeV^{-1}$) |
|---|---|
| 43.44 | 0.0010 ± 0.0001 |
| 44.03 | 0.0070 ± 0.0001 |
| 44.62 | 0.020 ± 0.001 |
| 45.21 | 0.051 ± 0.001 |
| 45.79 | 0.108 ± 0.003 |
| 46.38 | 0.185 ± 0.003 |
| 46.97 | 0.225 ± 0.005 |
| 47.56 | 0.227 ± 0.007 |
| 48.15 | 0.240 ± 0.009 |
| 48.74 | 0.16 ± 0.01 |
| 49.32 | 0.11 ± 0.01 |
| 49.91 | -0.01 ± 0.02 |
| 50.50 | 0.12 ± 0.02 |
| 51.09 | 0.17 ± 0.02 |
| 51.68 | 0.17 ± 0.02 |
| 52.26 | 0.001 ± 0.03 |
| 52.85 | -0.06 ± 0.03 |
| 53.59 | -0.01 ± 0.03 |
| 54.32 | 0.03 ± 0.03 |
| 55.06 | -0.01 ± 0.02 |

## A.2 Weak coupling model applied to $^{51}$V

In order to establish the sign of the deformation parameter of the couplings in the $^{36}\mathrm{S}+{}^{51}\mathrm{V}$ system, the weak-coupling approximation was used. In this section the method used to extract the sign under this approximation is described.

The coupling strenghts between the states $I$ and $I'$ is:

$$\frac{\beta^{(k)}_{I\,I'}}{\sqrt{4\pi}} = \sqrt{\frac{2\lambda+1}{4\pi}} < Ik|\hat{\alpha}_{\lambda 0}|I'k > \tag{A.1}$$

where $\hat{\alpha}_{\lambda 0}$ is the surface coordinate related to the phonon creation and annihilation operators and to the electric quadrupole operator $\hat{Q}^{(E\lambda)}_{\lambda\mu}$. Indeed, for a sharp matter distribution of the target nucleus, the electric multipole operator is given by

$$\hat{Q}^{(E\lambda)}_{\lambda\mu} = \frac{3e}{4\pi} Z_T R_T^{\lambda} \hat{\alpha}_{\lambda\mu} \tag{A.2}$$

where $Z_T$ and $R_T$ are the charge and radius of the target, respectively. The transition probability between the initial $I_i$ and final $I_f$ state is

$$B(E\lambda; I_i \to I_f) = \frac{1}{2I_i+1} | < I_i||\hat{Q}^{(E\lambda)}_{\lambda}||I_f > |^2 \tag{A.3}$$

If the state $I_i$ is the ground-state ($I_i = 0$) the expression A.1 is reduced to Eq. 2.57. Using the Eq. A.2, the transition probability can be expressed as

$$B(E\lambda; I_i \to I_f) = \frac{1}{2I_i+1} \left( \frac{3e}{4\pi} Z_T R_T^{\lambda} \right)^2 | < I_i||\hat{\alpha}_{\lambda\mu}||I_f > |^2 \tag{A.4}$$

The element of matrix $< I_i||\hat{\alpha}_{\lambda\mu}||I_f >$ is therefore

$$< I_i||\hat{\alpha}_{\lambda\mu}||I_f >= \pm \frac{4\pi}{3eZ_T R_T^{\lambda}} \sqrt{(2I_i+1)B(E\lambda; I_i \to I_f)} \tag{A.5}$$

By replacing the above equation in Eq. A.1, the coupling strength is

$$\begin{aligned} \beta^{(k)}_{I\,I'} &= \sqrt{2\lambda+1}\,(-)^{I-k} \begin{pmatrix} I & \lambda & I' \\ -k & 0 & k \end{pmatrix} < I|\hat{\alpha}_{\lambda}|I' > \\ &= \pm\sqrt{2\lambda+1}\,(-)^{I-k} \begin{pmatrix} I & \lambda & I' \\ -k & 0 & k \end{pmatrix} \tfrac{4\pi}{3eZ_T R_T^{\lambda}} \times \sqrt{(2I_i+1)B(E\lambda; I_i \to I_f)} \end{aligned} \tag{A.6}$$

For a weak coupling model the total spin of the state can be decoupled in the spin of the core $I_C$ and of the state occupied by the weakly coupled nucleon/hole. The matrix element $< I_i||\hat{\alpha}_{\lambda}||I_f >$ thus becomes

$$\begin{aligned} &< I||\hat{\alpha}_{\lambda}||I' >=< [I_C \otimes Y_{ij}]^{(I)}||\hat{\alpha}_{\lambda}||[I'_C \otimes Y_{ij}]^{(I')} > \\ &= (-)^{I_C+j+I'+\lambda} \sqrt{(2I+1)(2I'+1)} \begin{Bmatrix} I_C & I & j \\ I' & I'_C & \lambda \end{Bmatrix} \times \\ &\times < I_C||\hat{\alpha}_{\lambda}||I'_C > \end{aligned} \tag{A.7}$$

For $I'_C = 0$ and $I' = j$

$$\left\{ \begin{array}{ccc} I_C & I & j \\ I' & I'_C & \lambda \end{array} \right\} = \left\{ \begin{array}{ccc} I_C & I & j \\ j & 0 & \lambda \end{array} \right\} = \left\{ \begin{array}{ccc} I & I_C & j \\ 0 & j & \lambda \end{array} \right\} = (-)^{I-I_C+j} \frac{1}{\hat{I_C}\hat{j}} \tag{A.8}$$

The sign of $< I||\hat{\alpha}_\lambda||I' >$ as well as of the coupling strength in the weak coupling limit is therefore determined by$-(-)^{I+j+\lambda}$. The $^{51}$V can be interpreted as a hole in the $f_{7/2}$ shell above $^{52}$Cr. According to the weak coupling model, the signs of coupling strenghts of the excited state (see Table 6.4 ) to the ground state are

$$\begin{array}{cccc} I = \frac{5}{2} & j = \frac{7}{2} & \lambda = 2 & \rightarrow \quad -1 \\ I = \frac{3}{2} & j = \frac{7}{2} & \lambda = 2 & \rightarrow \quad +1 \\ I = \frac{11}{2} & j = \frac{7}{2} & \lambda = 2 & \rightarrow \quad +1 \\ I = \frac{9}{2} & j = \frac{7}{2} & \lambda = 2 & \rightarrow \quad -1 \end{array} \tag{A.9}$$

The signs of the coupling strengths calculated for the coupling considered in the CC analysis are reported in Table 6.5.

# Bibliography

[1] C. Y. Wong. “Interaction barrier in charged-particle nuclear reactions”. In: *Physical Review Letters* 31.12 (1973), pp. 766–769. ISSN: 00319007.

[2] R. G. Stokstad et al. “Measurements of fusion cross sections for heavy-ion systems at very low energies”. In: *Physical Review Letters* 37.14 (1976), pp. 888–891. ISSN: 00319007.

[3] C. H. Dasso, S. Landowne, and A. Winther. “A study of Q-value effects on barrier penetration”. In: *Nuclear Physics A* 407.12 (1983), pp. 221–232.

[4] C. H. Dasso, S. Landowne, and A. Winther. “Channel-coupling effects in heavy-ion fusion reactions”. In: *Nuclear Physics A* 405 (1983), pp. 381–396.

[5] C. H. Dasso, S. Landowne, and A. Winther. “Barrier penetration in the presence of coupling to intrinsic degrees of freedom”. In: *Nuclear Physics A* 432 (1985), pp. 495–513.

[6] G. R. Satchler N. Rowley and P. H. Stelson. “On the “distribution of barriers” interpretation of heavy-ion fusion”. In: *Reviews of Modern Physics* 254 (1991), pp. 25–29. ISSN: 15390756.

[7] C. L. Jiang et al. “Unexpected behavior of heavy-ion fusion cross sections at extreme sub-barrier energies.” In: *Physical review letters* 89.5 (2002). ISSN: 0031-9007.

[8] K. Hagino and N. Takigawa. “Subbarrier fusion reactions and many-particle quantum tunneling”. In: 128.6 (2012). ISSN: 0033-068X.

[9] Ö. Akyüz and A. Winther. “Nuclear Structure and Heavy-Ion Collisions”. In: *Proc. Int. School of Physics “Enrico Fermi” Course LXXVII, Varenna* (1979).

[10] R. A. Broglia and A. Winther. *Heavy-Ion Reactions*. Addison-Wesley, New York, 1991.

[11] G. Bertsch et al. “Interactions for inelastic scattering derived from realistic potentials”. In: *Nuclear Physics A* 284 (1977), pp. 399–419.

[12] Ş. Mişicu and H. Esbensen. “Signature of shallow potentials in deep sub-barrier fusion reactions”. In: *Physical Review C* 75.3 (2007), pp. 1–14. ISSN: 05562813.

[13] H. Esbensen, C. L. Jiang, and A. M. Stefanini. “Hindrance in the fusion of $^{48}$Ca+$^{48}$Ca”. In: 054621 (2010), p. 8. ISSN: 0556-2813.

[14] P. Fröbrich and R. Lipperheide. *Theory of Nuclear Reactions*. Clarendon Press, 1996.

[15] R. Bass. *Nuclear Reactions with Heavy Ions*. Springer-Verlag, 1980.

[16] D. L. Hill and J. A. Wheeler. “Nuclear constitution and the interpretation of fission phenomena”. In: *Physical Review* 89.5 (1953), pp. 1102–1145. ISSN: 0031899X.

[17] J. R. Leigh et al. “Nuclear constitution and the interpretation of fission phenomena”. In: *Physical Review C* 52.6 (1995), p. 3151. ISSN: 0556-2813.

[18] M. Beckerman et al. “Dynamic influence of valence neutrons upon the complete fusion of massive nuclei”. In: *Physical Review Letters* 45.18 (1980), pp. 1472–1475. ISSN: 00319007.

[19] A. B. Balantekin, S. E. Koonin, and J. W. Negele. “Inversion formula for the internucleus potential using sub-barrier fusion cross sections”. In: *Physical Review C* 28.4 (1983), p. 1565.

[20] S. Yusa, K. Hagino, and N. Rowley. “Role of noncollective excitations in low-energy heavy-ion reactions”. In: *Physical Review C* 82 (2010), pp. 1–7.

[21] S. Yusa, K. Hagino, and N. Rowley. “Role of noncollective excitations in heavy-ion fusion reactions and quasi-elastic scattering around the Coulomb barrier”. In: *Physical Review C* 85 (2012), pp. 1–8.

[22] M. N. Harakeh and A. Van Der Woude. *Giant Resonances*. Oxford University Press, 2001.

[23] O. Tanimura, J. Makowka, and U. Mosel. “Adiabatic approach to subbarrier fusion cross section”. In: *Physics Letters B* 163 (1985), pp. 317–322.

[24] N. Takigawa et al. “Role of mass renormalization in adiabatic quantum tunneling”. In: *Physics Review C* 49.5 (1994), p. 2630.

[25] M. Dasgupta et al. “Measuring Barriers to Fusion”. In: *Annu. Rev. Nucl. Part. Sci.* 48 (1998), pp. 401–461.

[26] K. Hagino, N. Rowley, and A. T. Kruppa. “A program for coupled-channels calculations with all order couplings for heavy-ion fusion reactions”. In: *Computer Physics Communications* 123 (1999).

[27] M. A. Nagarajan, A. B. Balantekin, and N. Takigawa. “Geometric interpretation of the adiabatic model for heavy-ion fusion”. In: *Physical Review C* 34.3 (1986), pp. 894–898.

[28] A. M. Stefanini et al. “Influence of Complex Surface Vibrations on the Fusion of $^{58}$Ni + $^{60}$Ni”. In: *Physical Review Letters* 74.6 (1995), pp. 864–867. ISSN: 0031-9007.

[29] H. Esbensen and S. Landowne. “Higher-order coupling effects in low energy heavy-ion fusion reactions”. In: *Physical Review C* 35.6 (1987), pp. 2090–2096. ISSN: 05562813.

[30] C. L. Jiang et al. “Influence of nuclear structure on sub-barrier hindrance in Ni + Ni fusion”. In: *Physical Review Letters* 93.1 (2004). ISSN: 00319007.

[31] B. B. Back et al. “Recent developments in heavy-ion fusion reactions”. In: *Reviews of Modern Physics* 86 (2014), pp. 317–360. ISSN: 15390756.

[32] A. Mişicu and H. Esbensen. “Hindrance of heavy-ion fusion due to nuclear incompressibility”. In: *Physical Review Letters* 96.11 (2006), pp. 1–4. ISSN: 00319007.

[33] T. Ichikawa, K. Hagino, and A. Iwamoto. “Signature of smooth transition from sudden to adiabatic states in Heavy-Ion fusion reactions at deep Sub-Barrier energies”. In: *Physical Review Letters* 103.20 (2009), pp. 1–4. ISSN: 00319007.

[34] T. Ichikawa. “Systematic investigations of deep sub-barrier fusion reactions using an adiabatic approach”. In: *Physical Review C* 92.6 (2015), pp. 1–19. ISSN: 1089490X.

[35] E. M. Burbidge et al. “Synthesis of the elements in stars”. In: *Reviews of Modern Physics* 29.4 (1957), pp. 547–650. ISSN: 00346861.

[36] G. Montagnoli and A. M. Stefanini. “Recent experimental results in sub- and near-barrier heavy-ion fusion reactions”. In: *European Physical Journal A* 53.8 (2017). ISSN: 1434601X.

[37] V. Yu. Denisov. “Subbarrier heavy ion fusion enhanced by nucleon transfer”. In: *European Physical Journal A* 7.1 (2000), pp. 87–99. ISSN: 14346001.

[38] V. I. Zagrebaev. “Sub-barrier fusion enhancement due to neutron transfer”. In: *Physical Review C* 67.6 (2003), p. 5. ISSN: 1089490X.

[39] A. M. Stefanini et al. “Fusion of $^{48}Ca+^{90,96}$Zr above and below the Coulomb barrier”. In: *Physical Review C* 73.3 (2006), pp. 1–8. ISSN: 1089490X.

[40] A. M. Stefanini et al. “Sub-barrier fusion of $^{40}$Ca+$^{94}$Zr: Interplay of phonon and transfer couplings”. In: *Physical Review C* 76.1 (2007), pp. 4–8.

[41] H. Timmers et al. “A case study of collectivity, transfer and fusion enhancement”. In: *Nuclear Physics A* 633.3 (1998), pp. 421–445. ISSN: 03759474.

[42] J. F. Liang et al. “Fusion of radioactive $^{132}$Sn with $^{64}$Ni”. In: *Physical Review C* 75.5 (2007), p. 054607. ISSN: 0556-2813.

[43] Z. Kohley et al. “Near-barrier fusion of Sn+Ni and Te+Ni systems: Examining the correlation between nucleon transfer and fusion enhancement”. In: *Physical Review Letters* 107.20 (2011), pp. 1–5. ISSN: 00319007.

[44] V. Yu. Denisov and S. Hofmann. “Formation of superheavy elements in cold fusion reactions”. In: *Physical Review C* 61 (2000), pp. 1–15. ISSN: 034606.

[45] N. Takigawa, H. Sagawa, and T. Shinozuka. “Fusion of a halo nucleus and synthesis of superheavy elements”. In: *Nuclear Physics A* 538 (1992), pp. 221–228.

[46] Z. Kohley et al. “Sub-barrier fusion enhancement with radioactive $^{134}$Te”. In: *Physical Review C* 87.6 (2013), pp. 1–6. ISSN: 1089490X.

[47] J. J. Kolata et al. “Fusion of $^{124,132}$Sn with $^{40,48}$Ca”. In: *Physical Review C* 85.5 (2012), pp. 1–7. ISSN: 1089490X.

[48] H . L. Ravn. “Experiments with intense secondary beams of radioactive ions”. In: *Physics Reports* 54 (1979), pp. 201–259.

[49] M. Cogneau et al. “Production of a high purity $^{18}$F radioactive beam”. In: *Nuclear Instruments and Methods in Physics* 420 (1999), pp. 489–493.

[50] J . F. Liang and C Signorini. “Fusion Induced by Radioactive Ion Beams”. In: *International Journal of Modern Physics E* 14.8 (2005), p. 1121. ISSN: 0218-3013.

[51] T. J. M. Symons et al. “Observation of New Neutron-Rich Isotopes by Fragmentation of 205-MeV/Nucleon $^{40}$Ar Ions”. In: *Physical Review Letters* 42.1 (1979).

[52] G. De Angelis et al. “The SPES radioactive ion beam project of INFN”. In: *Journal of Physics: Conference Series* 527.1 (2014). ISSN: 17426596.

[53] G. Prete et al. “The SPES project: An ISOL facility for exotic beams”. In: *AIP Conference Proceedings - 12th Conference on ‘Theoretical Nuclear Physics in Italy’* 1120 (2009), pp. 247–252. ISSN: 0094243X.

[54] *SPES Beam Tables*. URL: `https://web.infn.it/spes/index.php/nuclear-physics/spes-beams-2014`.

[55] G. Prete et al. “The SPES project: An ISOL facility for exotic beams”. In: *AIP Conference Proceedings - HIAT09, Venice, Italy* 1120 (2009), pp. 247–252. ISSN: 0094243X.

[56] D. Shapira et al. “A high-efficiency compact setup to study evaporation residues formed in reactions induced by low-intensity radioactive ion beams”. In: *Nuclear Instruments and Methods in Physics Research A* 551.2-3 (2005), pp. 330–338. ISSN: 01689002.

[57] G. Montagnoli et al. “The large-area micro-channel plate entrance detector of the heavy-ion magnetic spectrometer PRISMA”. In: *Nuclear Instruments and Methods in Physics Research* 547.2-3 (2005), pp. 455–463. ISSN: 01689002.

[58] G. F. Knoll. *Radiation Detection and Measurement*. John Wiley Sons Inc, IV edition, 2010.

[59] H. W. Fulbright. “Ionization Chambers”. In: *Nuclear Instruments and Methods* 162 (1979), pp. 21–28.

[60] H. Stelzer. *Detectors in Heavy-Ion Reactions*. Springer - Verlag, 1982.

[61] G. Montagnoli et al. “Fusion hindrance for the positive Q -value system $^{12}$C + $^{30}$Si”. In: *Physical Review C* 97.2 (2018), pp. 1–6. ISSN: 24699993.

[62] G. Montagnoli et al. “Fusion of $^{28}$Si + $^{28,30}$Si: Different trends at sub-barrier energies”. In: *Physical Review C* 90.4 (2014). ISSN: 0556-2813.

[63] G. Colucci et al. “Isotopic effects in sub-barrier fusion of Si + Si systems”. In: *Physical Review C* 97.4 (2018), pp. 1–8. ISSN: 24699993.

[64] J. F. Liang et al. “Enhanced fusion-evaporation cross sections in neutron-rich $^{132}$Sn on $^{64}$Ni”. In: *Physical Review Letters* 91.15 (2003), pp. 1–4. ISSN: 10797114.

[65] K. Kimura et al. “High-rate particle identification of high-energy heavy ions using a tilted electrode gas ionization chamber”. In: *Nuclear Instruments and Methods in Physics Research* 538.1-3 (2005), pp. 608–614. ISSN: 01689002.

[66] K. Y. Chae et al. “Construction of a fast ionization chamber for high-rate particle identification”. In: *Nuclear Instruments and Methods in Physics Research A* 751 (2014), pp. 6–10. ISSN: 01689002.

[67] L. Corradi. “The Tandem-ALPI-PIAVE Accelerator Facility Usage Operation , Maintenance and Developments of LNL Heavy Ion Accelerator Complex”. In: *LNL Annual Report* (2009), pp. 177–179.

[68] M. Mazzocco. “TANDEM-ALPI-PIAVE Accelerator Complex : Facility Usage”. In: *LNL Annual Report* (2016), p. 152.

[69] J. F. Ziegler. *SRIM - The Stopping and Range of Ions in Matter*. URL: `http://www.srim.org/`.

[70] *PACE 4 : evaporation code operating under MS Windows*. URL: `http://lise.nscl.msu.edu/pace4.html`.

[71] H. Esbensen. “Complete fusion of $^{9}$Be with spherical targets”. In: *Physical Review C - Nuclear Physics* 81.3 (2010), pp. 1–8. ISSN: 1089490X.

[72] P. R. S. Gomes et al. “Comprehensive study of reaction mechanisms for the $^{9}$Be + $^{144}$Sm system at near- and sub-barrier energies”. In: *Physical Review C - Nuclear Physics* 73.6 (2006), pp. 1–11.

[73] J. Randrup and J. S. Vaagen. “On the proximity treatment of the interaction between deformed nuclei”. In: *Physics Letters B* 77.6 (1978), pp. 170–173.

[74] E. F. Aguilera et al. “Sub-barrier fusion of $^{27}$Al + $^{70,72,73,74,76}$Ge: Evidence for shape transition and structure effects”. In: *Physical Review C* 41.3 (1990), pp. 910–919. ISSN: 05562813.

[75] H. Esbensen. “Fusion reactions with germanium isotopes”. In: *Physical Review C - Nuclear Physics* 68.3 (2003), p. 12. ISSN: 1089490X.

[76] C. L. Jiang et al. “Fusion hindrance for $^{27}$Al + $^{45}$Sc and other systems with a positive Q value”. In: *Physical Review C - Nuclear Physics* 81.2 (2010), pp. 1–7. ISSN: 1089490X.

[77] N. J. Stone. “Table of nuclear magnetic dipole and electric quadrupole moments”. In: *Atomic Data and Nuclear Data Tables* 90 (2005), pp. 75–176.

[78] *National Nuclear Data Center - $^{36}$S*. URL: `http://www.nndc.bnl.gov/chart/getdataset.jsp?nucleus=36S&unc=nds`.

[79] *National Nuclear Data Center - $^{50}$Ti*. URL: `http://www.nndc.bnl.gov/chart/getdataset.jsp?nucleus=50TI&unc=nds`.

[80] S. Raman et al. “Transition probability, B(E2)↑, from the ground to the first-excited $2^+$ state of even-even nuclides”. In: *Atomic Data and Nuclear Data Tables* 36 (1987), pp. 1–96.

[81] T. Kibédi and R. H. Spear. “Reduced electric-octupole transition probabilities, B(E3;$0_1^+ \rightarrow 3_1^-$) - An update”. In: *Atomic Data and Nuclear Data Tables* 80.1 (2002), pp. 35–82. ISSN: 0092640X.

[82] J. Childs. “Hyperfine Structure of Nine Levels in Two Configurations of $^{51}$V”. In: *Physical Review* 156 (1967), pp. 71–82.

[83] *National Nuclear Data Center - $^{51}$V*. URL: `http://www.nndc.bnl.gov/chart/getdataset.jsp?nucleus=51V&unc=nds`.

[84] E. Piasecki et al. “Barrier distributions in $^{16}$0+$^{116,119}$Sn quasielastic scattering”. In: *Physical Review C* 65.5 (2002), p. 054611. ISSN: 0556-2813.

[85] E. Piasecki et al. “Structure of barrier distributions; probing the role of neutron-transfer channels”. In: *International Journal of Modern Physics E* 16.2 (2007), pp. 502–510. ISSN: 02183013.

# *Acknowledgements*

Voglio ringraziare tutti coloro che mi hanno aiutato e sostenuto durante questo percorso.
Per primi ringrazio i miei supervisors Giovanna e Alberto che mi hanno introdotto nel mondo della fisica nucleare sperimentale. A loro va la mia gratitudine per gli insegnamenti e il sostegno che mi hanno fornito in questi 3 anni, per tutto il tempo che hanno speso per aiutarmi nella realizzazione di questo lavoro, per la completa disponibilità che hanno sempre mostrato ed ancora per le tante opportunità che mi hanno offerto e per tutti i loro preziosi consigli.
Un sentito grazie a Lorenzo, Enrico, Fernando, Suzana, Petra, Franco e Alain per il loro indispensabile aiuto e per gli ottimi suggerimenti che mi hanno fornito durante i vari esperimenti. I thank Dr. Hagino to have provided the modified CCFULL program and for his clear explanations and the useful helps.
Un ringraziamento speciale a tutta la mia famiglia su cui ho sempre potuto fare affidamento. A mia madre che con la sua forza riesce sempre a farmi vedere il lato positivo delle cose e a mio padre che con la sua dolcezza mi supporta in tutte le scelte. Grazie ai miei nonni Liliana e Ilo, per la loro grande fiducia, il loro affetto ed il loro incredibile e incondizionato sostegno. Un grazie a mio fratello Davide, per avermi sempre ascoltato e ai miei zii e cugini che nonostante la lontananza mi sono sempre stati vicini con le loro attenzioni, i "pacchi" e le chiamate domenicali.
Ringrazio i miei amici, i miei coinquilini Mattia, Eugenia e Cora, per la seconda famiglia che hanno creato a Padova, e gli amici di sempre: Floriana, Giada, Davide, Andrea, Fabiana, Ornella, Silvia, Elisa, Giorgio, Sara, Simona e Silvia.
Dziękuję Asi, Teresie i Romanowi za polskie wsparcie.
Last but not least, a special thought goes to Grześ. Podziękowania dla Grzesia, który wypełnił barwami ten ostatni rok i który swoją nieskończoną słodyczą sprawił, że każdy dzień był szczęśliwy.